Analytica Chimica Acta xxx (2015) xxx–xxx

Contents lists available at ScienceDirect

Analytica Chimica Acta

journal homepage: www.elsevier.com/locate/aca

Review

Two decades of chemical imaging of solutes in sediments and soils – a review

Jakob Santner[a,1,*], Morten Larsen[b,1], Andreas Kreuzeder[a], Ronnie N. Glud[b,c,d,e]

[a] *Rhizosphere Ecology and Biogeochemistry Group, Department of Forest and Soil Sciences, Institute of Soil Research, University of Natural Resources and Life Sciences Vienna, Konrad Lorenz-Strasse 24, 3430 Tulln, Austria*
[b] *Nordic Center for Earth Evolution (NordCEE), University of Southern Denmark, Campusvej 55, 5230 Odense, Denmark*
[c] *Scottish Marine Institute, Scottish Association for Marine Science, Oban, Scotland, PA37 1QA, UK*
[d] *Greenland Climate Research Centre (CO Greenland Institute of Natural Resources), Kivioq 2, Box 570, 3900 Nuuk, Greenland*
[e] *Arctic Research Centre, Aarhus University, 8000 Aarhus, Denmark*

HIGHLIGHTS

- We review the state-of-the-art of solute imaging in soils, sediments and wetlands.
- Solute imaging techniques are described in detail.
- Method characterisics, capabilities and limitations are discussed.
- An overview on applications of solute imaging is given.
- Potential directions of further development and application are outlined.

GRAPHICAL ABSTRACT

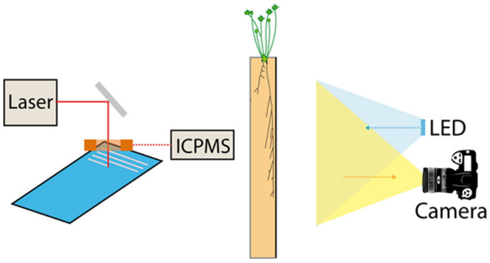

ARTICLE INFO

Article history:
Received 10 September 2014
Received in revised form 3 February 2015
Accepted 5 February 2015
Available online xxx

Keywords:
Chemical imaging
Solute
Diffusive equilibration in thin films (DET)
Diffusive gradients in thin films (DGT)
Planar optodes
Luminescent sensors

ABSTRACT

The increasing appreciation of the small-scale (sub-mm) heterogeneity of biogeochemical processes in sediments, wetlands and soils has led to the development of several methods for high-resolution two-dimensional imaging of solute distribution in porewaters. Over the past decades, localised sampling of solutes (diffusive equilibration in thin films, diffusive gradients in thin films) followed by planar luminescent sensors (planar optodes) have been used as analytical tools for studies on solute distribution and dynamics. These approaches have provided new conceptual and quantitative understanding of biogeochemical processes regulating the distribution of key elements and solutes including O_2, CO_2, pH, redox conditions as well as nutrient and contaminant ion species in structurally complex soils and sediments. Recently these methods have been applied in parallel or integrated as so-called sandwich sensors for multianalyte measurements. Here we review the capabilities and limitations of the chemical imaging methods that are currently at hand, using a number of case studies, and provide an outlook on potential future developments for two-dimensional solute imaging in soils and sediments.

---

[*] Corresponding author. Tel.: +43 1 47654 3129.
E-mail address: jakob.santner@boku.ac.at (J. Santner).
[1] These authors contributed equally and share the first-authorship of this review paper.

http://dx.doi.org/10.1016/j.aca.2015.02.006
0003-2670/© 2015 The Authors. Published by Elsevier B.V. This is an open access article under the CC BY license (http://creativecommons.org/licenses/by/4.0/).

Please cite this article in press as: J. Santner, et al., Two decades of chemical imaging of solutes in sediments and soils – a review, Anal. Chim. Acta (2015), http://dx.doi.org/10.1016/j.aca.2015.02.006

Contents

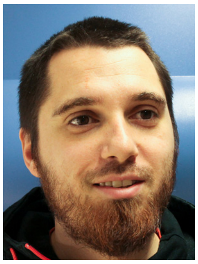

Jakob Santner is a postdoctoral research associate at the Institute of Soil Research of the University of Natural Resources and Life Sciences, Vienna (Austria). He did his PhD on plant–soil interactions in plant root P acquisition, including the development and application of chemical imaging methods for solute mapping in plant rhizospheres. His current research is focused on the development and application of passive solute sampling techniques for bulk soil analysis as well as chemical imaging applications for investigating biological hotspot in soils.

Morten Larsen is a postdoctoral researcher at the Institute of Biology at the University of Southern Denmark, Odense (Denmark). He did his PhD on microscale carbon mineralization in marine sediments, including the development and application of planar optodes. His current research is primarily focused on the application and development of ultra-sensitive oxygen sensors to study low oxygen environments and associated biogeochemical rates and pathways.

Please cite this article in press as: J. Santner, et al., Two decades of chemical imaging of solutes in sediments and soils – a review, Anal. Chim. Acta (2015), http://dx.doi.org/10.1016/j.aca.2015.02.006

Andreas Kreuzeder is a PhD student at the Institute of Soil Research of the University of Natural Resources and Life Sciences, Vienna (Austria). Currently he is working on the development and application of high-resolution methods for simultaneous chemical imaging of solutes in the rhizosphere. He is particularly interested in the combination of different imaging methods for the investigation of rhizosphere processes.

Ronnie N. Glud is Professor at the University of Southern Denmark. His research focuses on "biogeochemistry and climate change". He has developed, applied and optimized a range of optical and electrochemical sensors for *in situ* investigations in many different environments from sea-ice to hadal trenches. He is in particular interested in understanding the interrelation between carbon turnover and environmental controls from the micro-scale to regional and global scales.

1. Introduction

Soil and sediment related processes are central for large-scale element cycling and ultimately regulate the chemical composition of the atmosphere and the aquatic environment. Soils and sediments store enormous amounts of organic material, nutrients and redox sensitive minerals, but at the same time the upper soil and sediment horizons represent sites of intense remineralisation and biogeochemical activity. Microbial communities regenerate organic material and nutrients and the associated redox and pH dynamics regulate the mobility of many important trace elements.

The intense biogeochemical activity in sediment, wetland and submerged soils typically induces steep concentrations gradients of the involved redox species [1–3]. Generally, particulate material and oxidizing agents are supplied from above and in undisturbed, water-logged conditions this induces a characteristic stratification of the respective degradation processes and a gradual increase in redox values with depth [1]. Processes like advective porewater transport, ebullition and faunal as well as root activity can disturb this simple vertical zonation and induce complex three-dimensional structures. Additionally, mechanical reworking of the surface layer can dramatically redistribute both, solids and solutes. Despite the overall, large-scale vertical zonation, these environments can in many cases best be characterized as dynamic, mosaic-like distributions of diagenetic processes and redox species [2,4]. In the aquatic sciences, the requirement for high-resolution measurement techniques for resolving these intense biogeochemical dynamics led to the development of a wide range of different microsensors [5,6]. Traditional applications of these sensors resolve one-dimensional, high-resolution vertical concentration profiles and indeed such data have provided detailed and invaluable insight on the ecology and biogeochemical activity of sediments [5,6].

It was soon realized that numerous profiles were required to overcome, or to fully characterize, the complex microscale variability of natural systems [7–10]. Furthermore, alignment of profiles obtained at different microsites could provide a false impression on the actual zonation or overlaps of biogeochemical processes especially in temporally dynamic systems [4]. This recognition initiated the development of different approaches for better resolving the actual two-dimensional (2D) distribution of solutes and gasses in benthic communities. In early, gel-based methods (diffusive equilibration in thin films (DET), and diffusive gradients in thin films (DGT)), gel slices were inserted into sediments, and subsequently, 2D analysis was performed on the recovered gels [11–14]. Later, dyeing procedures of entrapped solutes were used for imaging the distribution of specific solutes or processes after gel recovery [15,16]. Parallel to the first DGT methods, real-time imaging of immobilized, luminescent dyes that were sensitive to different solutes, so-called planar optodes, were developed [17–21]. Since then, many different configurations and interrogation approaches have been used for optimized performance in different settings or to address specific questions.

Redox cycles play a less dominant role in terrestrial soils than in wetlands and sediments. The vertical zonation of terrestrial soils is governed by the decomposition of plant residues, their mixing into the surface layers and the weathering of the parent rock material [22]. However, as for sediments, solute uptake and release by plant roots, bioturbation, faunal activity as well as localised microbial processes enhance the spatial heterogeneity of soils [23–25]. Moreover, variable groundwater tables and water retention by finely textured layers or impermeable soil horizons can induce highly variable redox conditions in terrestrial soils [22]. Therefore, point microsensors [26], planar pH measurements [27], film autoradiography [28] as well as thin-layer sampling [29] were applied early on for resolving the distribution of solutes in soil, with most effort being directed towards investigations of solute distributions around plant roots.

Even though some early investigations applied micro- and planar sensors to soil, the development and application of micro- and especially planar sensors for biogeochemical process studies has mainly been driven by aquatic scientists. Given the extreme microscale variability in soils it is surprising that these technical developments have only recently been more broadly applied to soil research [12,19,30–32].

The present review provides an overview of available techniques for chemical imaging that have been successfully applied in sediments and more recently in soil studies. Advantages and challenges of different designs are evaluated and discussed together with the potential for further advances in 2D chemical sensing and how this can facilitate novel scientific developments, especially in soil science.

2. Principles

2.1. DET

Diffusive equilibration in thin films was initially developed for measuring the Fe(II) and Mn(II) concentration at the water–sediment interface at spatial resolutions of up to 100 μm [33,34]. DET uses polyacrylamide hydrogels with a water content of ~95% for the localised sampling of solutes. In the original configuration the hydrogels are contained in polytetrafluoroethylene (PTFE) or ceramic gel holders with an exposure window of ~15 × 2 cm. These samplers are pushed into the sediment and are retrieved after the solute concentration in the gel has equilibrated with the porewater.

The solute distribution at spatial resolutions of ~3 mm can be determined by slicing the gel, back-equilibrating the solutes in a small volume of water or acid and subsequent determination of the solute concentration in the solvent [14]. Resolutions down to ~100 μm can be obtained by converting the solutes into an

Please cite this article in press as: J. Santner, et al., Two decades of chemical imaging of solutes in sediments and soils – a review, Anal. Chim. Acta (2015), http://dx.doi.org/10.1016/j.aca.2015.02.006

immobile phase, *e.g.* by precipitating dissolved Fe and Mn by exposing the DET gel to NaOH [33,34]. The gel is then dried and analysed by beam techniques like particle induced X-ray emission (PIXE) or laser ablation inductively coupled plasma mass spectrometry (LA-ICPMS).

A few, early studies used DET for measuring 2D concentration images [14,34], while most of the DET applications so far only resolved averaged 1D vertical concentration profiles across the sediment-water interface and into the sediment by slicing the DET gel. The most recent developments in 2D imaging include simple colorimetric DET techniques for measuring Fe(II) and phosphate [15,16,35–38] as well as a 2D DET technique for the measurement of NO_3^- and N_2 isotopic composition [39]. These approaches are discussed in more detail below.

2.2. DGT

Diffusive gradients in thin films was introduced as a dynamic speciation tool for measuring element concentrations in waters [40,41]. The DGT technique has since been adopted as an analytical tool for the determination of the availability of nutrients and contaminants to terrestrial [42,43] and aquatic organisms [44], complex dissociation kinetics [45] and also for 2D chemical imaging of the distribution of labile chemical species in both, soils and sediments [11–13,15,36,46–59].

The typical DGT setup consists of two layers; a polyacrylamide hydrogel layer that contains a binding agent, overlain by a diffusive layer consisting of a diffusive gel (polyacrylamide hydrogel without resin material) and a protective membrane [41]. This gel assembly is housed in a plastic sampling unit that only exposes the membrane to the outer medium (Fig. 1a). During DGT application, the analytes diffuse through the diffusive layer towards the resin gel where they get immediately bound. Thereby the analyte concentration at the resin gel–diffusive gel interface remains effectively zero, providing a constant zero-sink for the analytes which causes a continuous diffusive flux of analyte into the sampler. At the end of the experiment the resin gel is retrieved, eluted and analysed for the amount of analyte taken up. The accumulated amount of analyte can be interpreted as time-averaged flux into the sampler (f_{DGT}) using

$$f_{DGT} = \frac{M}{At} \tag{1}$$

or as time-averaged concentration (c_{DGT}) at the interface of the DGT sampler and the sampled medium.

$$c_{DGT} = \frac{M\Delta g}{DAt} \tag{2}$$

In Eqs. (1) and (2) M is the mass of analyte bound to the resin gel, Δg is the diffusive layer thickness, D is the diffusion coefficient in the hydrogel, A is the sampling area, and t is the sampling time [41,60].

DGT chemical imaging has so far been used to investigate sediment biogeochemistry as affected by plant roots and animal burrows [15,36–38,53,61], solute dynamics in microbial micro-niches in sediments [13,16,36,47–49,56,62–65] as well as for investigating nutrient and contaminant uptake and solubilisation in the vicinity of terrestrial plant roots [12,50,59].

2.3. Planar optodes

Optodes are optical sensors that measure the change in photoluminescence as a function of the analyte concentration. Optodes exist as 1D single-point devices that can be used to measure the bulk analyte concentration in a solution or a gas [66,67], and in a 2D variant (termed 'planar optode') that is capable of acquiring high spatial resolution (μm range) images of the analyte distribution in real time [17]. The planar optode setup consists of a luminophore immobilized in an analyte-permeable matrix that is coated onto a support material (*e.g.* a plastic foil) and a camera-based imaging system (Fig. 1). The sensors are typically mounted on the inside wall of transparent containers (rhizotrons or aquaria).

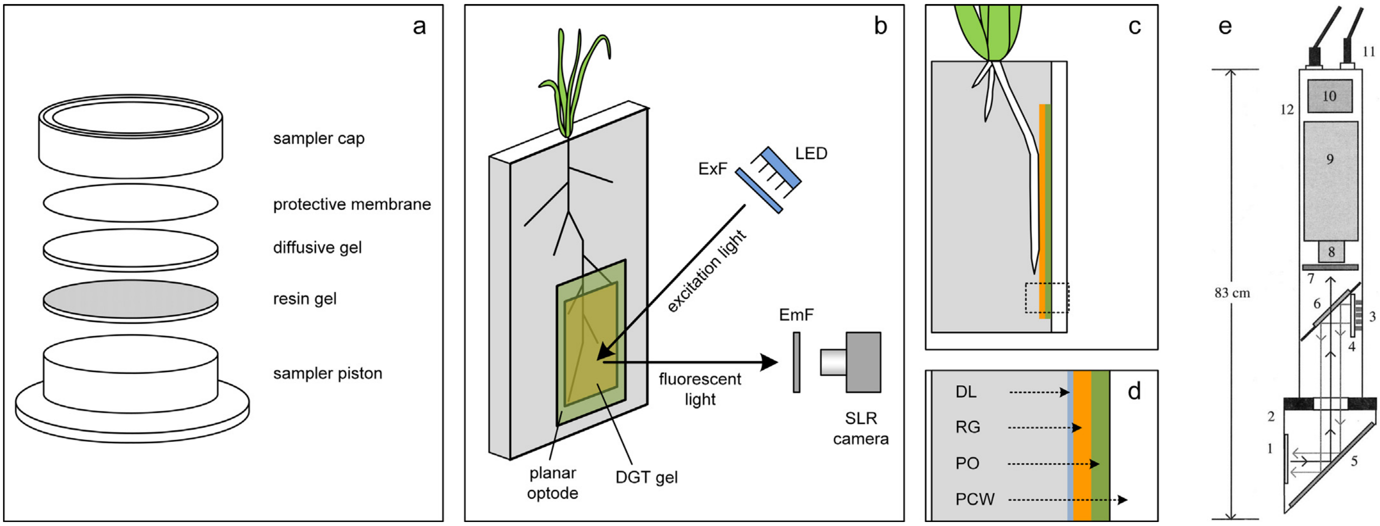

Fig. 1. DGT and planar optode sampling setups. (a) Exploded view of a standard (non-2D) DGT sampler showing the gel layer setup contained in the plastic sampler housing. (b) Application of a DGT gel and a planar optode sensor foil onto a root system of a plant grown in a rhizotron. ExF and EmF denote the excitation and emission light filters. (c) Side view of the sampling setup. (d) Close-up of (c) showing the DGT diffusion layer (DL), which is usually a ca. 10 μm thick membrane, the resin gel (RG) and the planar optode (PO). These sampling/sensor layers are fixed by tape to the plastic container wall (PCW). (e) Schematic drawing of an in situ planar optode module. The camera and electronics (8,9,10) are housed in a pressure cylinder (12). The optode (1) is mounted on the head of the periscope (2) together with a mirror (5). LED excitation light (3) and optical filters (4,6,7) are placed in the pressure cylinder. Communication and power is provided externally (11). The instrument can be used at water depths of up to 6000 m. Reproduced with permission from [201]. Copyright 2014 by the Association for the Sciences of Limnology and Oceanography, Inc. (For better readability of the colours in this figure the reader is referred to the web version of this article.)

Please cite this article in press as: J. Santner, et al., Two decades of chemical imaging of solutes in sediments and soils – a review, Anal. Chim. Acta (2015), http://dx.doi.org/10.1016/j.aca.2015.02.006

2.3.1. Photoluminescence

Planar optodes rely on a photoluminescent indicator entrapped in an analyte-permeable matrix. Upon absorption of a photon, the luminescent indicator is excited from its ground state to a higher vibrational level [68], followed by a nonradiative transmission to the lowest vibrational level. Subsequently, the indicator returns to its ground state through a radiative de-excitation transmission, during which a part of the absorbed energy is emitted in the form of a photon. This process is termed luminescence.

Two major de-excitations processes are possible, (1) fluorescence emission and (2) phosphorescence emission [68]. Fluorescence is shorter-lived with lifetimes near 10^{-8} s. The majority of luminescence sensors relevant for soil and sediment studies are fluorescent, including pH and pCO_2 sensors. Phosphorescent emission is longer lived and has lifetimes of 10^{-6} s to several hours. The only two phosphorescence sensors used in soil and sediment studies have so far been based on O_2 and temperature-sensitive luminophores. For both types of luminescence the emission light has a longer wavelength than the absorbed excitation light – this phenomenon is referred to as 'Stokes shift'.

For O_2 indicators de-excitation can also occur through a non-luminescent process. The excited luminophore may return to its ground state by transferring the absorbed energy to a quencher molecule (*e.g.* O_2) in its immediate vicinity, a process that is termed 'dynamic (collisional) quenching'. Since this mode of deactivation is non-luminescent the presence of a quencher will reduce the indicator's luminescence intensity and its phosphorescence lifetime. Temperature indicators also show a luminescent lifetime dependency, this is however due to thermal quenching [69].

In cases without quenchers, *e.g.* pH/pCO_2 indicators, only a change in luminescence intensity is observed as function of analyte concentration. This intensity change is due to changes in the absorption or emission spectra of the indicators, caused by their dynamic interaction with the analyte. For O_2 and pCO_2 sensors the luminescence intensity decreases with increasing analyte concentrations [17,20,70–72] whereas the luminescence intensity for *e.g.* pH and NH_4^+ sensors often increase with analyte concentration, depending on sensor design [18,73–75].

Luminescent sensors may be reversible or irreversible. Throughout this article we use the term 'sensors' with reference to both, reversible and irreversible luminescent sensors. Reversible sensors dynamically react to the analyte concentration of the external medium as their interaction with the analyte is based on free diffusion and equilibrium between sensors and medium. Irreversible sensors, however, bind the analyte permanently and therefore only provide a signal integrated over the application time similar to DGT. Reversible sensors include luminophores for O_2, pH, pCO_2, NH_3, NH_4^+ [17,18,72,74,76], examples of irreversible sensors include Fe^{2+}, Cu^{2+} and enzyme activity [77–79]. While irreversible sensors can provide important information about biogeochemical processes, fully reversible sensors are much more powerful in resolving analyte dynamics in response to environmental changes. In this review we will focus on fully reversible planar optodes as these have been most widely applied and have generated most novel scientific insights on biogeochemical functioning in soil, wetland and sediment systems.

3. Methodology

3.1. Imaging experiment setup

Several setups have been used for applying DET/DGT gels and optodes onto soils and sediments. For the investigation of sediment chemistry, typical DET and DGT imaging (and 1D profile) applications were done using flat (~0.5 cm) gel housings that have a sampling window of 2–5 × 15 cm [11,14,34,49,62]. Recently, a larger and thicker (1.4 cm) gel holder with an 8 × 17 cm window was used for dual-layer DET–DGT studies [16,36,37]. For sampling, these gel setups are pushed into the sediment, and left for a given period for equilibration or analyte uptake, respectively. The insertion might smear the sediment profile by carrying adhering sediment particles downwards, but surprisingly, thorough and systematic testing of potential smearing artefacts on DGT, DET and planar optode results is still lacking. In a recent experiment we found considerable smearing of fluorescent particles (Fig. 2) after inserting a flattened sediment corer into sediment, demonstrating that a large number of particles can be transported down the sampled profile, whereby the analyte distribution in the sampled region is considerably altered. Detailed investigation of smearing upon sampler insertion is therefore highly desirable.

For gel deployment on plant roots or along animal burrows that would be damaged by the insertion of such samplers, a different deployment procedure is needed. For root studies plants are grown in flat, transparent growth containers (rhizotrons) at an inclination of 30–45° to induce root growth along the wall [12,50,59]. The wall of the rhizotron can be removed for applying DGT (or DET) gels onto the roots and the surrounding soil (Fig. 1). Typically a thin membrane layer (10 μm) covers the soil to avoid injury to the root when opening the growth container. After opening the rhizotron, the gel setup is taped onto the inner side of the removed wall. Subsequently, the wall with the DGT gel is re-installed for the sampling period. The use of transparent walls allows to direct link physical features (*e.g.* roots architecture) to gel measurements. Solute dynamics around (artificial) animal burrows have been investigated with a similar experimental setup, *i.e.* DGT-planar optode double layer sensors taped to the wall of an aquarium across the sediment-water interface [55].

Laboratory planar optode studies are typically conducted in aquaria, flumes or chambers similar to rhizotrons, made of plastic [80] or glass [81] with at least one wall being made of a transparent material. The planar optode sensor is mounted on this transparent wall/window [82]. Often the window is detachable from the rest of the assembly [83] – thus allowing different walls with *e.g.* different types of optodes (*e.g.* O_2, pH or pCO_2) to be used successively. The optode sensors are either taped [84], glued [17] or directly coated onto the wall [85]. Inverted periscopes equipped with planar optodes have also been applied to study solute dynamics in marine sediments *in situ* (Fig. 1e) [86,87].

3.2. DGT and DET

3.2.1. Hydrogel preparation

Hydrogels used in DET and DGT are usually polyacrylamide gels either cross-linked by an agarose-derived crosslinking agent supplied by DGT Research Ltd. (Lancaster, UK) [41,60], by *N*, *N*′-methylene-bis-acrylamide [60], or by methacrylamide [46,47]. While resin gels contain embedded or precipitated ion binding resin materials, diffusive gels are plain hydrogels. Thin gel films are produced by adding appropriate amounts of ammonium persulphate as polymerisation initiator and *N*,*N*,*N*′,*N*′-tetramethylethylenediamine (TEMED) as catalyst to the acrylamide-cross linker solutions and quickly pipetting these solutions between two glass plates [60]. The glass plates are separated by thin plastic spacers and held together by clips. By varying the spacer thickness gels of different thickness, typically 0.2–1.2 mm, can be produced. After polymerisation, the gels are hydrated and remaining chemicals are washed off in successive baths of deionised water. Diffusive gels need to be conditioned in 0.01–0.001 mol L^{-1} NaCl or $NaNO_3$ for avoiding artefacts caused by local electrical charges in the

Please cite this article in press as: J. Santner, et al., Two decades of chemical imaging of solutes in sediments and soils – a review, Anal. Chim. Acta (2015), http://dx.doi.org/10.1016/j.aca.2015.02.006

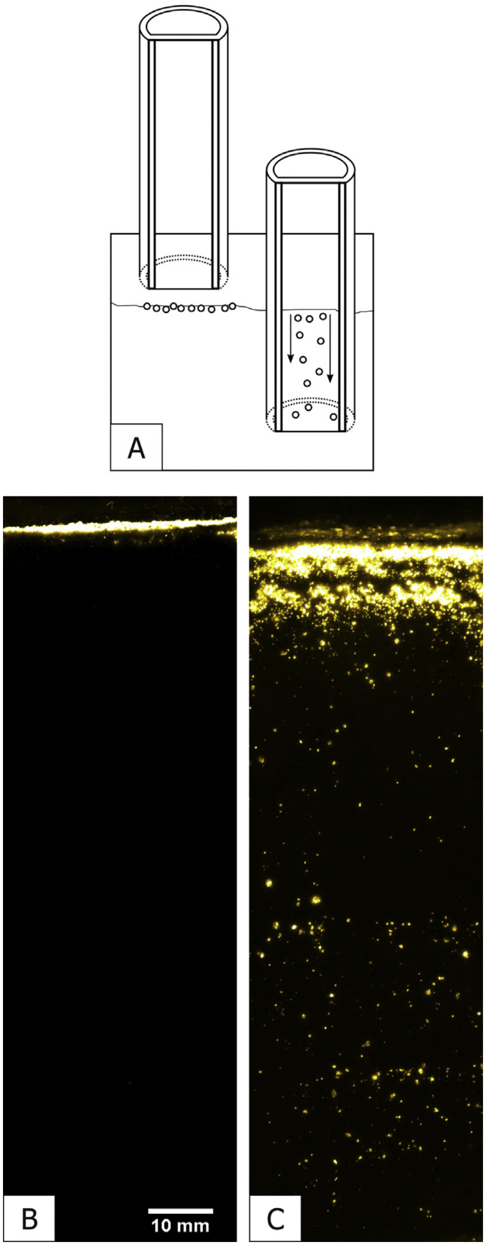

Fig. 2. Particle smearing caused by sampler insertion. (a) Schematic of the smearing experiment, which demonstrates the insertion of a transparent core liner with a flat front window (45 mm wide) into a sandy marine sediment. The bottom of the core liner had a 45° beveled edge to reduce the mechanical resistance during insertion. The surface sediment was covered with a ~1 mm thick layer of fluorescent sand particles with a size distribution comparable to the sediment. The sampler with sediment was subsequently removed and the distribution of the fluorescent sand particles was imaged under UV light excitation. (b) Image of the sediment before insertion of the sampler, the thin layer of fluorescent sand is visible on the surface. (c) Image of the sediment after sampler insertion. It is evident that the insertion caused significant particle smearing. Most of the visible particles (>80%) were observed in the top 15 mm of the sediment, however >350 particles with a diameter larger than 0.2 mm were observed deeper than 15 mm. The particles appeared down to the maximum sampler insertion depth (~120 mm). The experiment was conducted several times with similar results. It should be noted, that in the presented experiment only the displacement of the fluorescent particles can be observed and thus the true smearing of particles and porewater might be underrepresented. Unpublished results of Morten Larsen and Ronnie N. Glud.

polyacrylamide matrix on analyte diffusion and binding in the diffusive gel [60]. These effects are described in detail in Section 4.1.3.

3.2.2. Resin gels

High-resolution DGT measurements typically resolve the solute distribution in the resin gel in the range of 50–500 μm [12,57]. However, conventional DGT resin gels, incorporating relatively coarse binding agents like Chelex 100 (bead size ~100 μm; Bio-Rad Hercules, CA, US) or ferrihydrite slurry [41,88] do not provide a sufficiently homogeneous distribution of the binding phase in the gel matrix for measurements at these small spatial scales. Consequently, resin gels with highly homogeneous distributions of very fine sorbents were developed to overcome this problem [46,48,51,54,89]. An overview on resin gels suitable for 2D analysis is given in Table 1.

Davison et al. [11] pioneered this development by using the suspended particulate reagent – iminodiacetic acid (SPR-IDA; CETAC, Omaha, NE, US) resin. It has a bead size of ~0.2 μm and, like Chelex 100, mainly binds transition metals by its iminodiacetic acid groups. The SPR-IDA gel formulation described by Warnken et al. [89] has a Cd capacity of 570 nmol cm^{-2} gel. This is usually considered an estimate for the general transition metal capacity of this gel as Chelex has a relatively low affinity for Cd compared to metals like Cu, Co, Ni, Zn and Pb [90]. For some analytes, *e.g.* Fe(II) and Mn(II), Chelex 100 has however considerably lower affinities. In environments with high dissolved Fe(II) and Mn(II) concentrations like reduced sediments, competition for binding sites and displacement effects on the resin could therefore cause artefacts in the DGT measurement. Generally, performance testing of resin gels should be done carefully to avoid problems with saturating the resin gel layer beyond its capacity, where it ceases to function as zero sink, and with the competition and potential displacement of analytes from binding sites on the resin.

To image the distribution of total dissolved sulphide (S^{2-} + HS^- + H_2S), different procedures of embedding AgI in resin gels have been developed. The technique takes advantage of the colour change from yellow to black when AgI and sulphide form Ag_2S [13]. A gel with a sulphide capacity of ~3 μmol cm^{-2} was made by mixing AgI powder into the gel solution before initiating the polymerisation. Upon exposure to a sulphide-containing sediment, dark Ag_2S patches developed on the gel, which can subsequently be quantified by computer imaging densitometry (CID, see Section 4.1.1) using standard gels of known sulphide concentrations [13]. In addition to determining the accumulated amount of sulphide after gel retrieval using CID, it might also be possible to monitor the rate of darkening of AgI gels by frequently taking photographs, potentially allowing to study the dynamics of sulphide production in sediments. A method for direct precipitation of AgI inside a polyacrylamide gel was presented by Devries and Wang [62]. Here $AgNO_3$ was added to the gel solution at a concentration of about 0.1 mol L^{-1}. Gels polymerised from this solution were subsequently immersed in 0.2 mol L^{-1} KI, leading to the precipitation of a AgI phase in the gel. The advantage of their procedure was a more homogeneous AgI distribution in the gel along with less photoreduction of AgI to black Ag(0), which otherwise could interfere with the quantification of Ag_2S.

By adding a ferrihydrite phase in a second precipitation step, Stockdale et al. [56] made it possible to simultaneously determine S^{2-}, PO_4^{3-}, VO_4^{3-} and AsO_4^{3-} in the vicinity of microbial hotspots of a freshwater sediment. The ferrihydrite was precipitated by immersing the AgI gel in a 0.1 mol L^{-1} $Fe(NO_3)_3$ solution for 2 h and subsequently soaking the gel in a carbonate buffer adjusted to pH 6–7. Although the resulting gel showed good performance in the LA-ICPMS analysis of P, V and As, the red ferrihydrite phase

Please cite this article in press as: J. Santner, et al., Two decades of chemical imaging of solutes in sediments and soils – a review, Anal. Chim. Acta (2015), http://dx.doi.org/10.1016/j.aca.2015.02.006

Table 1
DGT and DET methods for high-resolution, two-dimensional imaging of solutes in soils and sediments.

Resin	Analytical technique	Analytes	LOD	Precision	Upper dynamic range	Reference
Diffusive equilibration in thin films (DET)						
			μmol L^{-1}	%		
	PIXE [a]	Fe^{2+}, Mn^{2+}				[34]
	Slicing & ZF-AAS [b]	Fe^{2+}, Mn^{2+}				[14]
	Segmented gel probe & GC-IRMS [c] and colorimetry	NO_3^-, $^{29}N_2$, $^{30}N_2$	0.4 ($^{29}N_2$) 0.3 ($^{30}N_2$)			[39]
	CID [d]	Fe^{2+}, PO_4^{3-}	~1 (Fe^{2+}) ~2 (PO_4^{3-})	7.3 (Fe^{2+}) 12.2 (PO_4^{3-})		[38]
Diffusive gradients in thin films (DGT)						
			pmol cm^{-2}	%	μmol cm^{-2}	
SPR-IDA [e]	PIXE, LA-ICPMS [f]	Mn^{2+}, Fe^{2+}, Co^{2+}, Ni^{2+}, Cu^{2+}, Zn^{2+}, As, Cd^{2+}, Pb^{2+}	1-110	7-16		[11,58,89,178]
AgI	CID	S^{2-}	4230	5.3	1	[13]
AgI and Ferrihydrite	LA-ICPMS, CID	S^{2-}, PO_4^{3-}, AsO_4^{3-}, VO_4^{3-}	2-125	< 10		[56]
Ferrihydrite	LA-ICPMS	PO_4^{3-}, AsO_4^{3-}, MoO_4^{3-}, SbO_4^{3-}, WO_4^{3-}, U	30 (P only)	< 10 (P only)		[54,57]
Zr-oxide	Slicing & Colorimetry, CID	PO_4^{3-}	6770 (CID)	5–40 (Slicing, depending on gel loading) <7 (CID)	1.3 (CID)	[46,48]
Zr-oxide and AgI	Slicing & Colorimetry, CID	PO_4^{3-}, S^{2-}	2500 (S^{2-})		0.94 (S^{2-})	[47]
SPR-IDA and Zr-hydroxide	LA-ICPMS	PO_4^{3-}, AsO_4^{3-}, Cu^{2+}, Cd^{2+}	11 (As), 24 (Cu), 348 (Cd), 1097 (P)	13-40		[51]
AgI	LA-MC-SF-ICPMS [g]	$\delta^{34}S$ in S^{2-}, S^{2-}		0.03 ($\delta^{34}S$)		[182]
Multilayer DGT and DET techniques						
			μmol L^{-1}	%	μmol L^{-1}	
AgI	CID	S^{2-} (DGT) Fe^{2+} (DET)				[15]
AgI	CID	S^{2-} (DGT) Fe^{2+} (DET)	0.6 (Fe)	< 10 (Fe)	500 (Fe)	[16]
AgI	CID	S^{2-} (DGT) PO_4^{3-}, Fe^{2+} (DET)	0.22 (P)	< 5 (P)	1000 (P)	[36]
SPR-IDA and AgI	LA-ICPMS, CID	Mn^{2+}, Fe^{2+}, Co^{2+}, Ni^{2+}, Cu^{2+}, Zn^{2+}, S^{2-} cations and sulphide on separate DGT gels				[63]

[a] Particle induced X-ray emission.
[b] Zeeman furnace – atomic absorption spectroscopy.
[c] Gas chromatography – isotope ratio mass spectrometry.
[d] Computer imaging densitometry.
[e] Suspended particulate reagent – iminodiacetic acid.
[f] Laser ablation inductively coupled plasma mass spectrometry.
[g] Laser ablation multi collector sector field inductively coupled plasma mass spectrometry.

interfered with the sulphide CID measurement, which was therefore only interpreted semi-quantitatively.

A directly precipitated, ferrihydrite-only gel has been tested for its suitability for the analysis of PO_4^{3-} at high spatial resolution using LA-ICPMS [54] and for the bulk analysis of VO_4^{3-}, AsO_4^{3-}, SeO_4^{3-} and SbO_4^{3-} [91]. The gel showed a five-fold increased phosphate capacity (224 nmol cm^{-2}) compared to a ferrihydrite gel made by adding ferrihydrite slurry prior to polymerisation [88]. The capacities for VO_4^{3-}, AsO_4^{3-}, SeO_4^{3-} and SbO_4^{3-} were 260, 257, 104 and 149 nmol cm^{-2}, respectively. With this gel, DGT measurements up to (pore-) water concentrations of 29–84 mmol L^{-1} (24 h deployment at 20 °C, depending on species) are possible. However, such high concentrations will only be encountered in highly fertilised or contaminated environments.

Ding et al. [92] developed a high-capacity Zr-oxide containing polyacrylamide gel for chemical imaging applications [46–48]. This gel has a phosphate capacity of ~3.2 μmol cm^{-2} [92] and arsenic capacities of 0.43 μmol cm^{-2} (As(III)) and 1.18 μmol cm^{-2} (As(V)) in low ionic strength conditions (I = 0.01 mol L^{-1}) and of 0.26 μmol cm^{-2} (As(III)) and 0.41 μmol cm^{-2} (As(V)) at the ionic strength of sea water [93].

Although this gel has been applied repeatedly, it is not easy to reproduce. When trying to make this gel, the Zr-oxide material seemed to interfere with the acrylamide polymerisation process, which could be due to the known capability of group III–VIII transition metals to catalyse polymerisation reactions [94]. The analyte range of the original Zr-oxide gel was extended to include S^{2-} by adding granular AgI prior to gel polymerisation [47], which was used to show the simultaneous release of dissolved reactive phosphate and sulphide from sulphidic microniches in a freshwater sediment.

A novel, high-resolution resin gel capable of measuring both, anionic and cationic solutes using SPR-IDA and Zr-hydroxide as ion resins has recently been developed [51]. The use of a polyurethane gel matrix (Hydromed D4, AdvanSource Biomaterials, Wilmington, MA, USA) makes this gel highly geometrically stable and tear-proof even down to thicknesses of 100 μm. These features ease the combination of DGT with other planar solute imaging techniques (see Section 3.4), which requires very thin gel layers to avoid image blurring (see Sections 4.1.4, 4.1.5, 4.2.1). We currently use this gel for the investigation of anion and cation distributions around plant roots.

3.3. Planar optodes

3.3.1. Planar optode sensor design

Planar optode sensors consist of the luminescent indicator immobilized in an analyte-permeable matrix fixed to a sensor support. The luminescent indicator is the analyte-specific component of the sensor and is chosen based on its luminescent properties and its sensitivity to the analyte of interest. Table 2 provides a list of the indicators that have been applied to planar optode imaging, Table S1 presents indicators that have so far not been applied for planar optode imaging, but which are of potential interest for future planar optode work in soil and sediment.

The indicator is immobilized in a matrix that serves three main functions, (1) the entrapment of the indicator, either physically or by chemical bonding to the matrix polymer, (2) preventing indicator aggregation as well as its diffusion into the external medium and (3) as permeable membrane that allows for the diffusion of the analyte towards the indicator and facilitates analyte equilibration between the matrix and the external medium. For O_2 sensors the dynamic range of the sensor can be tuned by changing the analyte permeability of the matrix [95,96].

The sensor support functions as a physical support upon which the sensor is cast and is required for convenient handling of the sensor. The support is generally a transparent polyester sheet

Table 2
Overview on indicators used for planar optode imaging. For O_2 and pH sensors the dynamic range is dependent on the matrix.

Luminescent indicator	Matrix	Imaging approach	Dynamic range	Comments	References
O_2indicators					
Ru-dpp	PVC, polystyrene, ORMOSIL	Intensity, lifetime	$0 > 100\%$ air saturation	Good resolution at higher O_2 concentration	[17,108,110,176]
PtTFPP	Polystyrene, hydrogel	Intensity, lifetime, ratiometric	0–100% air saturation	Highest resolution at low O_2 concentration	[85,106,114,118,164]
PtOEP	Polystyrene	Intensity, lifetime, ratiometric	0–100% air saturation	Highest resolution at low O_2 concentration	[82,115]
$Ir(Cs)_2(acac)$	Polystyrene	Lifetime	$0 > 100\%$ air saturation	Highest resolution at higher O_2 concentration	[70,97,119]
pH indicators					
HPTS (8-hydroxy-1,3,6-pyrenetrisulfonic acid trisodium salt)	Hydrogel, ethyl cellulose, cellulose acetate, poly(vinyl alcohol)	Ratiometric	~5.5–9.5	Good photostability, high brightness	[18,75,82,83,120,123]
DHFA (2′,7′-dihexyl-5(6)-*N*-octadecylcarboxamido-fluorescein)	Hydrogel	DLR	~7.2–9.3	Low interference from ionic strength	[125,126,219]
DHFAE (2′,7′-dihexyl-5(6)-*N*-octadecyl-carboxamidofluorescein ethyl ester)	Hydrogel	DLR	~7.2–9.3	Negligible interference from ionic strength	[124,126]
5-Hexadecanoylamino-fluorescein	Hydrogel	Intensity	~5.0–8.0	Low interference from ionic strength	[127]
DHPDS (6,8-dihydroxypyrene-1,3-disulfonic acid)	Cellulose acetate	Ratiometric	~6.0–9.0	Low interference from ionic strength	[73]
pCO_2indicators					
HPTS (8-hydroxy-1,3,6-pyrenetrisulfonic acid trisodium salt)	Ethyl cellulose	Ratiometric, DLR	0–~40 hPa.	Good photostability, high brightness	[20,72,122]
NH_4^+					
Merocyanine 540	Hydrogel	Ratiometric	$10–100 \times 10^3\ \mu mol\ L^{-1}$	Interference only from K^+	[133,134,227]
H_2S					
Pyronin Y	Ethyl cellulose	Intensity	$4–\sim3000\ \mu mol\ L^{-1}$	Semi reversible at high H_2S concentrations	[21]
Enzyme activity					
L-leucine 7-amido-4-methylcoumarin hydrochloride	Hydrogel	Intensity	n.a.[a]	Irreversible sensor, sensing approach can be applied to other enzymes	[77,152]
Fe^{2+}					
Ferrozine (3-(2-pyridyl)-5,6-diphenyl-1,2,4-triazine-*p*,*p*′-disulfonic acid monosodium salt hydrate)	poly(vinyl alcohol)	Intensity	$0–200\ \mu mol\ L^{-1}$	Irreversible sensor, absorbance based imaging approach	[78]

[a] Not available.

Please cite this article in press as: J. Santner, et al., Two decades of chemical imaging of solutes in sediments and soils – a review, Anal. Chim. Acta (2015), http://dx.doi.org/10.1016/j.aca.2015.02.006

(often referred to as the support foil); however other transparent materials may be used, as long as they are resistant to the matrix solvent and are inert towards the indicator. In addition to plastic support foils the sensing layer can be directly coated onto a glass plate of the imaging setup [85,97]. In some cases it is necessary to silanize the glass surface to ensure proper adhesion of the optode matrix, this can effectively be achieved by silanization with *e.g.* 3-(aminopropyl)-triethoxysilane (APTES) or dimethyldichlorosilane [98].

For manufacturing planar optodes with highly uniform indicator distribution, the indicator and the matrix are usually dissolved in a solvent and applied onto the sensor support by either knife coating [82], a film applicator [85] or by simply pipetting the solution onto the support foil. The mix of indicator and matrix in the solvent is referred to as the sensing cocktail. The sensing layer can also be applied by an air brush [99,100]. This procedure is particularly useful for small glass windows. After the application of the sensing cocktail, the solvent is often left to evaporate under a hood [72] to prevent fast evaporation that can cause imperfections in the sensing layer.

Generally it is advantageous to maintain a low indicator concentration in the sensing layer, as high concentrations of the indicator can lead to aggregation and consequently, self-quenching [101–103]. However, low dye concentrations will result in weak signals; therefore it is useful to increase the brightness of the sensor by other means than increasing the indicator concentration. Brightness increases can be achieved by adding light-scattering particles such as TiO_2 [17,85,99,103–106], diamond or gold [107], which increase the brightness by back-scattering of the luminescence light and increase the optical length of the excitation light, consequently enhancing the absorption by the indicator [103,105]. However, TiO_2 also acts as a photocatalyst, which can reduce sensor photostability [102]. A more elegant way to increase the brightness is to use an antenna dye, which efficiently absorbs the excitation light and transfers the energy to the indicator [102]. This light harvesting approach has so far been applied to O_2, pH and NH_3 sensors [82,101,102]. It is a very versatile principle that can applied to enhance the brightness of all luminescent sensors [102].

3.3.2. Planar optode indicators

3.3.2.1. O_2 indicators. The first planar optode sensors applied were based on intensity measurements of the O_2 indicator ruthenium (II)-tris-4,7-diphenyl-l,10-phenathroline perchlorate (Ru-dpp) [17] which is still one of the most widely used O_2 indicators [68]. It has a relative long phosphorescent lifetime, moderate brightness, excellent photostability and a long Stokes-shift, making it a good candidate for luminescent imaging. Ru-dpp is usually immobilized in polystyrene [30,108] or plasticized PVC [17,86,109] to achieve a dynamic range relevant for many biological systems (~0–100% air saturation). In one case Ru-dpp was incorporated in an organically modified sol–gel (ORMOSIL) [110]. The fabrication of ORMOSIL sensors is, however, cumbersome and has no explicit advantages for optode imaging. The Ru-dpp complex shows an almost linear decrease in luminescence lifetime as a function of increasing O_2 concentration when incorporated in polystyrene (Fig. 3c). One of its major disadvantages is the large temperature dependence of the luminescence which needs to be accounted for in many applications [70,111]. The temperature sensitivity can however be utilized to fabricate temperature sensors if the indicator is incorporated into an O_2 impermeable matrix [67]. The relatively broad emission peak (~150 nm) makes Ru-dpp non-ideal for ratiometric sensing; however, both, pure intensity and lifetime based imaging can be realized [31,112,113].

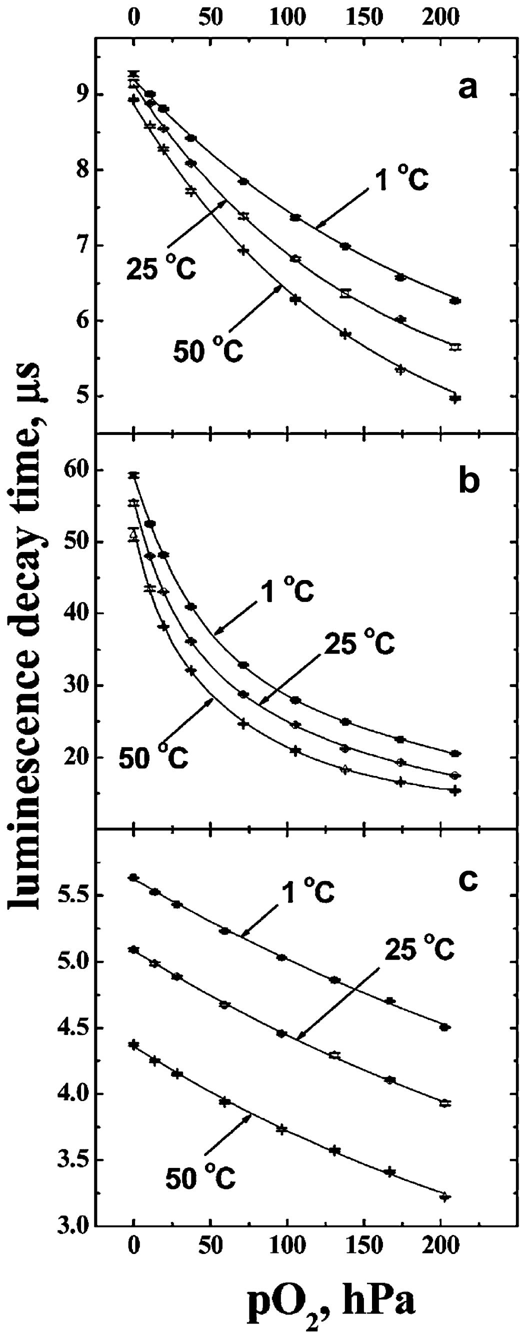

Fig. 3. Effect of temperature on calibration curves of luminescent O_2 sensors. (a) Ir $(C_S)_2$(acac), (b) PtTFPP and (c) Ru-dpp immobilized in a polystyrene matrix. Both Ir $(C_S)_2$(acac) and PtTFPP show a moderate interference from temperature compared to Ru-dpp which shows a strong interference. For all indicators the interference is predictable and allows for compensation when the temperature is monitored in parallel. Adapted with permission from Borisov and Klimant [70]. Copyright 2007 American Chemical Society.

In recent years platinum(II)-metalloporphyrin-based indicators have become widespread for O_2 imaging, especially the commercially available compounds platinum(II)-5,10,15,20-tetrakis-(2,3,4,5,6-pentafluorphenyl)-porphyrin (PtTFPP) and platinum (II)-2,3,7,8,12,13,17,18-octaethylporphyrin (PtOEP). Compared to Ru-dpp they offer longer phosphorescent lifetimes (Fig. 3) and narrower emission peaks (~30 nm), making them ideal for ratiometric imaging if a reference dye is added to the sensor cocktail [82,114]. PtOEP is brighter than Ru-dpp and PtTFPP [82,115].

Please cite this article in press as: J. Santner, et al., Two decades of chemical imaging of solutes in sediments and soils – a review, Anal. Chim. Acta (2015), http://dx.doi.org/10.1016/j.aca.2015.02.006

When polystyrene is used as sensor matrix, the Pt(II) based sensors exhibit a significantly higher sensitivity than Ru-dpp, at least at lower O_2 saturation levels (*i.e.* <75% air sat). This makes them especially useful for investigations at oxic–anoxic interfaces and in O_2 depleted environments [115]. Of the two common Pt(II) based indicators, PtTFPP is most frequently applied for planar optode imaging, mainly due to the better photostability [116].

An elegant approach to increase the sensor brightness of Pt(II) indicators is to use an antenna dye [102] as described in Section 3.3.1. Apart from increasing the sensor brightness, the antenna dye can also be used as internal reference, as part of the excitation energy collected by the antenna is emitted from the antenna dye itself [82,102]. The dual emission from both, the antenna dye and the indicator makes the sensors ideally suited for colour ratiometric measurements [82,84,114,117,118].

Lastly, a few studies have used cyclometalated iridium(III)-coumarin complexes such as $Ir(C_S)_2(acac)$ [70,97,119]. When immobilized in polystyrene, this indicator has a slightly shorter luminescence lifetime than Ru-dpp, with an almost linear response to O_2 concentration (0 to ~150% air saturation), but with a significantly increased brightness. Sensors based on this $Ir(C_S)_2(acac)$ complex embedded in a polystyrene matrix are an excellent choice for studies in O_2 super-saturated settings such as photosynthetic microbial communities [97,119]. As for Ru-dpp, the relatively broad emission peak makes $Ir(C_S)_2(acac)$ less suited for ratiometric imaging.

3.3.2.2. pH indicators. A few studies have applied pH, pCO_2 and NH_4^+ planar optodes for studies in soil, wetlands and sediment. The primary indicator used for pH measurements and the only one used to date for pCO_2, is 8-hydroxy-1,3,6-pyrenetrisulfonic acid trisodium salt (HPTS). HPTS is an excellent choice for ratiometric pH measurements, due to a simultaneous change in the absorption spectra of the protonated and the deprotonated form of the indicator, but with largely unaffected emission spectra. HPTS based sensors can be interrogated with dual excitation/single emission [18,75], single excitation/dual emission and dual excitation/dual emission (Section 3.3.4), [120]. For the single excitation/dual emission approach an additional dye can be added to increase the sensor brightness and to serve as the ratiometric reference [82,121]. Furthermore, HPTS shows excellent photostability [122]. Designs of pH sensors using HPTS have relied on the indicator immobilized in either poly(vinyl alcohol) [18,75,123], cellulose acetate [18], ethyl cellulose [120] or a polyurethane hydrogel (Hydromed D4) [82]. Like the majority of pH sensors, HPTS shows interference from ionic strength (Fig. 4a) [18,75].

Alternative indicators for pH sensors include the fluorescein derivates 2′,7-dihexyl-5(6)-*N*-octadecylcarboxamidofluorescein (DHFAE) and 2′,7′-dihexyl-5(6)-*N*-octadecylcarboxamidofluorescein (DHFA) which both operate well when immobilized in Hydromed D4 [110,124,125]. These indicators only display weak changes in the absorption and emission spectra of their protonated and de-protonated forms, therefore internal referencing has been obtained by adding phosphorescent reference particles based on Ru-dpp [124–126]. These sensors are typically interrogated by the t-DLR technique (Section 3.3.5). Both, DHFA and DHFAE show only little/negligible interference from changes in the ionic strength, making them better suited for the marine environment (Fig. 4b). These indicators, however, suffer from a rather poor long term stability [124], limiting the sensors lifetime to ~2–5 days [126].

In addition, the fluorescein derivate 5-hexadecanoylamino-fluorescein has been used for intensity based pH measurements also using Hydromed D4 as matrix [127]. This indicator has only negligible response to changes in the ionic strength.

Recently the indicator 6,8-dihydroxypyrene-1,3-disulfonic acid (DHPDS) has also been applied for pH sensing [128]. DHPDS shares most of the advantageous properties of HPTS, such as high quantum yield, excellent water solubility, ratiometric properties and lack of toxicity [73] but with negligible interference from changes in the ionic strength [73,128].

3.3.2.3. pCO_2, NH_4^+ and sulphide indicators. In principle, pCO_2 sensors are pH sensors covered by a gas-permeable membrane (*e.g.* silicone), which excludes interference from H^+ or other ionic species. The CO_2 in the medium will establish equilibrium with the sensing layer and induces a measurable pH change. Luminescent pCO_2 optodes are typically composed of a pH indicator dye and a lipophilic organic base incorporated in a hydrophobic polymer forming an ion pair. The lipophilic base is usually a quaternary ammonium hydroxide *e.g.* tetraoctylammonium hydroxide (TOA-OH) [129,130]. The addition of the base serves to neutralize acidic residues in the polymer and to create a buffer, thus stabilizing the deprotonated form of the pH indicator ion pair in the matrix [129,130]. The sensitivity of pCO_2 sensors generally depends on the apparent pK_a value of the indicator in the sensor matrix, on the CO_2 permeability of the polymer and on the amount and nature of the

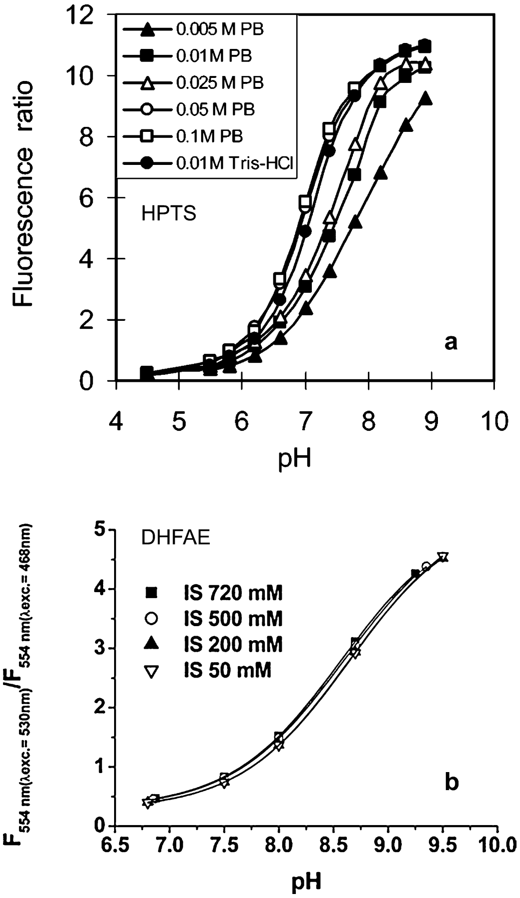

Fig. 4. Effect of ionic strength on calibration curves of pH planar optodes. (a) Calibration curves of a HPTS-based planar optode, which expresses considerabe changes as a function of the ionic strength in the external medium. The given concentrations refer to the ionic strength of the phosphate buffer (PB). 0.01 mol L^{-1} Tris–HCL represents the ionic strength of natural seawater. Increasing the ionic strength from 0.005 to 0.025 mol L^{-1} results in a considerable shift in the indicator's apparent pK_a, whereas increasing the buffer concentration from 0.05 to 0.1 mol L^{-1} has relatively little effect. Reprinted with permission from Zhu et al. [75]. Copyright 2005 American Chemical Society. (b) Calibration curves of a DHFAE-based sensor which is relatively insensitive to ionic strength changes in the range from 50 to 720 mmol L^{-1}. The calibration curves were measured in solutions containing 15 mmol L^{-1} TRIS buffer and natural seawater. The ionic strength of natural seawater is approximately 720 mmol L^{-1}. Reproduced in part from Schröder et al. [126] with permission of the Royal Society of Chemistry.

Please cite this article in press as: J. Santner, et al., Two decades of chemical imaging of solutes in sediments and soils – a review, Anal. Chim. Acta (2015), http://dx.doi.org/10.1016/j.aca.2015.02.006

lipophilic buffer substance added [129,131]. The HPTS(TOA) ion pair, immobilized in ethyl cellulose, is to date the only indicator reported to be used for planar optode imaging of pCO_2 [20,72].

The polarity-sensitive fluorescent indicator merocyanine 540 (MC540) has been developed and applied for NH_4^+ imaging [74,132–134]. The sensing system relies on a co-extraction technique [135], where the sensor matrix is based on a two phase system, containing a hydrogel (NH 80/92) and non-polar ether emulsion droplets. As the sensor is exposed to NH_4^+, the fluorescent dye MC540 changes solvent from the hydrogel to the ether emulsion droplets, a consequence of NH_4^+ binding to the solute-sensitive ionophore nonactin. The shift of solvent causes a change in the excitation–emission spectra of MC540. Quantification of the NH_4^+ concentration is made through a dual-excitation dual-emission ratiometric imaging approach [132]. Using time-correlated pixel-by-pixel calibration [74,127] this sensor was stable for up to 10 days at concentrations from 0 to 500 μmol L^{-1} [74,134]. The co-extraction technique has recently been modified by incorporating lyophilized gold nanoparticles into the ether phase of the NH_4^+ sensor, which reduced the noise level, increased the ratiometric signal, and improved the detection limit, as compared to the original sensor design [136,137]. It should furthermore be noted that the co-extraction based sensing scheme is universal and can be used for designing numerous sensors for a range of ions [137].

For many marine systems H_2S sensors are of particular interest. A few suitable indicators have been reported, but most lack reversibility and show interferences from pH and other solute species [138–140]. Recently, a semi-reversible H_2S sensor was realised by immobilizing pyronin Y (PY) into ethyl cellulose [21]. PY is a xanthene derivative that shows a bright fluorescence in aqueous solution. Depending on the amounts of PY immobilized in the sensor matrix, the dynamic range of the sensors is 4 to 3150 μmol L^{-1}. To avoid unwanted quenching from sulphide and bisulfide ions, the sensing layer was covered by a gas-permeable silicone membrane that was impermeable to hydrated ions. The reaction mechanism between PY and HS^- has not been specifically studied; however, it is hypothesized that the fluorescence quenching of PY is caused by the formation of PY^+HS^- ion pairs [21]. The sensor is not sensitive to pH or other dissolved gasses (O_2, N_2, CO_2, and NH_3). Another promising reversible indicator for future H_2S planar optodes is based on the indicator tetraoctylammonium fluorescein mercury(II) acetate immobilized in a poly(vinyl chloride) matrix together with tri-*n*-butyl phosphate [141].

3.3.2.4. Other reversible luminescent indicators. Other reversible luminescent indicators for measuring temperature, Cl^-, H_2O, NH_3 and NO_3^- have been developed [142–149]. Although no 2D applications using these sensors have been realised in soil or sediments, they can potentially be applied for planar optode sensing and most of the sensors can be interrogated with ratiometric imaging approaches. An overview on potential planar optodes for future biogeochemical studies indicators is given in Table S1.

Several combinations of indicators for designing single-layer, multi-analyte sensors have been presented. Such sensors include dual (O_2/pCO_2, O_2/temperature and O_2/pH), triple (O_2/pH/temperature) and quadruple ($O_2/pH/pCO_2$/temperature) sensors [76,122,150,151]. Some of these combinations could potentially be developed for planar sensing, but in most cases this would involve a complex combination of different imaging approaches and the use of multiple emission-excitation settings.

3.3.2.5. Additional 2D sensors. In addition to the fully reversible sensors described so far, irreversible fluorescent sensors have been presented in the literature. An interesting sensor that has recently been applied to sediments quantifies the extracellular activity of leucine-aminopeptidase (Leu-AP) [77]. It relies on L-leucine-7-amido-4-methylcoumarin hydrochloride (Leu-MCA) as 'indicator', and on MCA as fluorophore. The principle of the sensing system is the controlled diffusion of the non-fluorescent substrate (Leu-MCA) from the optode hydrogel layer into the sediment. The cleavage of Leu-MCA by Leu-AP releases MCA from the complex and generates a fluorescent signal which corresponds to the Leu-AP activity [77,152].

A very similar technique for imaging enzyme activities is soil zymography, which has been used for measuring protease and amylase activities [153], acid and alkaline phosphatase activities [154,155] as well as cellulose and chitinase activities [155]. Soil zymography was developed independently of the optode community. In this technique, enzyme substrate is immobilised in a 1 mm thick sheet of agarose gel. Substrate-loaded gels are then exposed to the soil matrix for 40 min – 18 h, allowing for the natural enzyme reaction to locally decrease the substrate concentration in the gel. Subsequently, the gels are retrieved and the remaining substrate is stained and imaged using a flatbed scanner [153]. Alternatively, the fluorescence of the reaction product, *e.g.* the fluorescence of methylumberrliferyl (MUF) that is released from non-fluorescent MUF-phosphate by phosphatases, can be measured by excitation with UV light and taking photographs of the emission light [154,155]. This approach is very new and has not been thoroughly evaluated for potential artefacts such as diffusive relaxation (see Section 4.1.4).

Zhu and Aller [78] presented an Fe^{2+} optode that relies on the widely used Fe^{2+} indicator ferrozine (3-(2-pyridyl)-5,6-diphenyl-1,2,4-triazine-*p*,*p*′-disulfonic acid monosodium salt hydrate), which was immobilized onto a PVA membrane. Ferrozine is a highly selective indicator for dissolved Fe^{2+}. Upon reaction with Fe^{2+} it forms a magenta coloured $Fe(ligand)_3^{2+}$ complex in aqueous solution. Ferrozine also reacts with Fe^{3+}, but the resulting complex is colourless and therefore does not interfere with the Fe^{2+} signal [78]. In the work presented by Zhu and Aller [78] the Fe^{2+} concentrations were quantified by absorbance after sensor recovery using a flatbed scanner. This approach is similar to DET Fe^{2+} imaging techniques [15,16,36], but the sensor presented by Zhu and Aller [78] is transparent and thus allows for Fe^{2+} distribution patterns to be directly related to visible features in the sediment. The absorbance could also be quantified using camera based intensity imaging with appropriate LED illumination. Thereby it could also be possible to follow the temporal development of the Fe^{2+} distribution.

Several candidates for irreversible planar optodes for imaging various metal species could be developed based on indicators for *e.g.* Fe^{3+}, Cu^{2+}, Zn^{2+} and Hg^{2+} [156–159] (Table S1).

3.3.3. Imaging systems

There are two main measurement principles for planar optode imaging, (1) the measurement of fluorescence intensity and (2) the measurement of phosphorescence lifetime. An overview on specific imaging approaches, as discussed in the following sections, is given in Table 3. Both imaging approaches rely on excitation light which is either delivered by high-power LEDs (light emitting diodes) [82,118,124] or by halogen/xenon lamps [17,72,83,160]. Due to their high power-to-size ratio, their low cost, and their narrow emission spectra, LEDs are usually preferred nowadays.

In planar optode imaging, luminescence lifetime or intensity is recorded by an optical read-out device with high spatial resolution, either using CCD (charged coupled device) or CMOS cameras (complementary metal oxide semiconductors). Acquisition of luminescent lifetime decay in the 10^{-6} s range requires

Table 3
Overview on imaging approaches and applicable analytes.

Imaging approach		Applicable analytes	Imaging hardware	Comments	References
Lifetime		O_2 Temperature	Fast gateable, high sensitive monochrome CCD[b] camera	Relatively complex imaging setup. The systems relies on non-commercial available hard- and software.	[80,85,115,170,173,228]
DLR[a]		pH pCO_2 NO_3^- NH_3 Cl^-	Fast gateable, high sensitive monochrome CCD camera	Relatively complex imaging setup. The systems relies on non-commercial available hard- and software.	[122,124,125,149,245]
Intensity		O_2 Enzyme activity Fe^{2+} pH H_2S	Monochrome CCD, colour CMOS[c] camera	Very simple imaging approach, but reduced images quality compared to ratiometric and lifetime based systems	[17,77,106,112,127,163]
Ratiometric	Dual excitation	pH pCO_2	Monochrome CCD, colour CMOS camera	Relatively simple imaging approach. Requires excitation at two wavelengths.	[18,20,75]
	Dual emission	O_2 pH pCO_2	Colour CMOS camera	Simple imaging approach utilizing inbuilt colour filter of the camera.	[71,82,104,114,118,161]
	Dual emission/ dual excitation	NH_4^+ pH	Monochrome CCD camera	Relatively simple imaging approach, but requires both, different emission filters and different excitation light sources.	[74,83]

[a] Dual lifetime referencing.
[b] Charged coupled device.
[c] Complementary metal-oxide-semiconductor.

high-sensitivity, low noise cameras with a fast electronic shutter. Such cameras are commercially available, but the requirement of custom-made software and auxiliary hardware makes lifetime based systems expensive (50,000–100,000 €). To our knowledge, no lifetime systems are currently commercially available. Intensity-based imaging setups can be acquired for less than 1000 € with all components being readily available from commercial sources [71,82,114]. Using less expensive digital cameras, the cost can be reduced even further [117,161].

Read-out systems based on single, movable optical fibres have also been realized [19,32,162]. As this approach does not allow for real time imaging and is fundamentally different from camera-based high-resolution systems it will not be discussed further in this review.

3.3.4. Intensity imaging

Intensity-based systems are the most widely applied for planar optode imaging in soil, wetlands and sediment, primarily due to the uncomplicated imaging approach that only requires relatively simple software and electronics. However, pure intensity measurements have some inherent disadvantages as they are sensitive to variations in background reflection, inhomogeneous distribution of the luminophore and variations in the homogeneity of the excitation light. These challenges can, to some extent, be minimized by careful pixel-to-pixel calibration of the optode before and/or after use [17,74] presuming that the signal remains stable during measurements. However, such approaches are often cumbersome. Furthermore, in most cases the approach requires that the sensors are covered by an optical insulation layer to reduce light scattering artefacts from soil, sediment or from roots behind the optode [17,109]. However, the optical insulation layer makes the sensor non-transparent and decreases the sensor response time (see Section 4.2.3). Due to these inconveniences, only a few studies have used the pure intensity based approach to date [127,163,164].

Ratiometric imaging, which utilizes the intensity ratio between two emissions images to determine the analyte concentration, partly overcomes the challenges of intensity based imaging. The two images are either recorded at two different excitation wavelengths [18,20,72], at two different emission wavelengths [165] or as dual-excitation, dual-emission images [134]. The two latter methods require the exchange of optical filters or more elegantly, the use of a colour camera that allows for simultaneously recording of the RGB colour space [82,114,166].

Compared to pure intensity measurements the ratiometric approach is relatively insensitive to inhomogeneities in the luminophore distribution and of the excitation light field. Furthermore, some radiometric designs largely eliminate interferences from indicator photobleaching [114] or temperature [75]. As for the pure intensity measurements, the ratiometric approach can be sensitive to colour-dependent light scattering from the soil/sediment behind the optode. This limitation can be overcome by applying a semi-transparent layer of silicone to the optode. The semi-transparent layer significantly reduces light scattering artefacts but still allows for visual inspection of structures behind to optode [82]. Some ratiometric approaches, using dual excitation/single emission imaging [72,106], appear insensitive to light scattering, presumably as any wavelength-dependent scattering is cancelled out or attenuated.

Intensity and ratiometric measurements can be realized using simple, commercially available digital single-lens reflex (DSLR) and other inexpensive colour cameras. Zhu et al. [75] were the first to apply this approach and used a DSLR camera to interrogate two-dimensional pH and pCO_2 sensors [72]. Later on, the full colour sensing potential of digital colour cameras was utilized by analysing both the red, green and blue (RGB) colours recorded in one image [71,82,114]. This is referred to as 'colour ratiometry' and has been used to interrogate O_2 and pH optodes. Colour ratiometry can in principle be used to interrogate almost any luminescent sensor [82]. Recently it was furthermore

Please cite this article in press as: J. Santner, et al., Two decades of chemical imaging of solutes in sediments and soils – a review, Anal. Chim. Acta (2015), http://dx.doi.org/10.1016/j.aca.2015.02.006

demonstrated that the hue parameter of the HSV colour space (hue, saturation, value) is a promising quantitative tool for fluorescence imaging [167]. Using this parameter the sensor precision was increased by a factor of ~3 compared to ratiometric measurements.

To date only one planar optode system, which is based on a USB microscope camera with 0.3 million effective pixels ("VisiSens", PreSens GmbH, Regensburg, Germany), is commercially available. This system is applicable to O_2, pH and pCO_2, but has a limited field of view (4.1 × 3.3 cm) compared to most other optode systems presented in the literature [104,168,169].

3.3.5. Lifetime imaging

As previously mentioned, lifetime-based imaging is superior to intensity-based sensing, but requires luminophores with relatively long lifetimes ($>10^{-6}$ s) and is therefore limited to O_2 and temperature. Holst et al. [170] introduced a modular luminescence lifetime-based imaging system for planar optode O_2 measurements based on the principle of rapid lifetime determination (RLD) [171,172]. In this approach the phosphorescent lifetime is calculated by dividing the mono-exponential lifetime decay curve (intensity plotted *vs.* time) into at least two areas of equal width. The intensity decrease between the areas is then used to calculate the luminescence lifetime.

The system of Holst et al. [170] relies on a fast, gateable high-sensitivity CCD camera to capture the relatively long-lived phosphorescent lifetime immediately after the excitation light is turned off. A similar system based on the same principle was developed by Oguri et al. [115], which recorded three images during the phosphorescence decay period.

To be applicable in planar optode imaging the phosphorophore lifetime should range between ~2 and 200 μs [70,173], therefore relatively complex hard- and software are required for triggering and synchronizing image acquisition and sensor excitation.

A combination of ratiometric and lifetime sensing for pH measurements has been presented and is referred to as time domain dual-lifetime referencing (t-DLR) [174]. In the t-DLR approach, the intensity of the indicator is referenced to the luminescent lifetime of a reference dye, resulting in a ratiometric approach. t-DLR has so far only been applied for imaging pH in marine systems [124,126].

Ratiometric imaging approaches for O_2, utilizing the luminescent lifetime have also been reported and are referred to as the shark fin approach [175]. This method applies the ratio of the luminescence images recorded during and after excitation [175–177]. The first image records the increase of the luminophore emission, while the second image records the integrated intensity signal during the luminophore decay time. The shark fin approach is the precursor of the RLD approach and requires only a relatively simple and low-cost imaging setup, however it has been applied in few studies only (*e.g.* [176]).

3.4. Simultaneous application of planar optodes and DGT

Recently, dual-layer 'sandwich' sensors that combine planar optodes and DGT gels were applied for the simultaneous imaging of trace metals and pH/O_2 [55,59]. In this assembly, the DGT gel serves as diffusive layer for the overlying optode sensor (Fig. 1), therefore very thin DGT gels are required to minimize blurring of the optode image [55]. Ultrathin DGT gels (≤100 μm) have been developed using polyacrylamide [52] and polyurethane [51] hydrogels. Stahl et al. [55] applied sandwich sensors for the simultaneous mapping of trace metals and O_2 in sediments, demonstrating localised Ni, Cu and Pb mobilisation from sediment as a result of bioirrigation. Using a similar setup, Williams et al. [59] showed differences in the mobilisation of Fe(II), As and Pb as compared to Co, Ni and Zn from iron plaque on submerged rice roots. Both studies clearly demonstrated that the investigation of complex biogeochemical processes requires the simultaneous analysis of multiple solute species along with their spatial distribution. Therefore we expect sandwich sensors to become an important tool in solute imaging.

4. Performance characteristics and limitations

4.1. DGT and DET

4.1.1. Gel analysis and analytical performance

Three approaches have been used to visualize the spatial information that is contained in recovered DGT and DET gels. (1) The least complicated, but also the least often applied is slicing the gel into small gel pieces, eluting the analytes and measuring their concentrations in the eluates [14,46]. Although this is a very simple approach, large amounts of samples for the subsequent time consuming liquid analysis are produced. (2) Computer imaging densitometry (CID) is the fastest approach but lacks multi-analyte capabilities. While most DGT/DET CID methods measure only one analyte species [13,16,36,37,47,48,62], a recent paper reported a procedure to measure phosphate and Fe(II) simultaneously [38]. (3) Laser ablation inductively coupled plasma mass spectrometry (LA-ICPMS) requires expensive equipment, but offers the highest spatial resolution along with the capability for multi-element analysis [12,50,54,58,59].

The analysis of DET and DGT gels for acquiring images is described in the following sections. A methodological overview including the range of analytes, limits of detection (LOD), precision, and dynamic range of the respective approaches can be found in Table 1.

4.1.1.1. Slicing and elution. Shuttleworth et al. [14] introduced gel slicing for obtaining images in a study measuring the 2D distribution of Fe and Mn in a freshwater sediment. After precipitating Fe and Mn in the gel by immersion in 10 mmol L^{-1} NaOH the gels were sliced to 3 × 3 mm pieces and eluted in 1 mol L^{-1} HNO_3. Subsequently the concentrations in the eluates were determined using Zeeman furnace – atomic absorption spectroscopy (ZF–AAS). In another set of studies Zr-oxide containing DGT gels were sliced into 0.45 × 0.45 mm pieces with a custom-made cutter consisting of many parallel aligned razor blades [46,47]. Elution with 1 mol L^{-1} NaOH was followed by neutralisation of the alkaline eluates with H_2SO_4 and colorimetric analysis using molybdate blue on a microplate spectrophotometer. A recent study used a quadratic DET probe with one hundred ~1 cm^2 large wells to sample NO_3^- and dissolved, ^{15}N labelled N_2 ($^{29}N_2$, $^{30}N_2$) in marine sand ripples for assessing nitrogen processing in permeable sand [39]. The isotopic composition of N_2 was analysed using a coupled gas chromatography – isotope ratio mass spectrometer (GC–IRMS), NO_3^- was determined colorimetrically after back-equilibration. In this study no actual slicing step was involved as the single gel pieces were separated by a thin plastic grid inside the DET sampler.

4.1.1.1.1. Resolution and analysis time. Manually slicing gels into pieces smaller than about 3 × 3 mm is hardly possible. Special cutters can help increasing the spatial resolution, but in any way large quantities of liquid samples accumulate. Analysis using microwell plate technology [46] can in some cases overcome this challenge. However, if no fast analytical approach exists and *e.g.* liquid ICPMS has to be performed, analysis time can be very long especially during high-resolution investigations.

Please cite this article in press as: J. Santner, et al., Two decades of chemical imaging of solutes in sediments and soils – a review, Anal. Chim. Acta (2015), http://dx.doi.org/10.1016/j.aca.2015.02.006

4.1.1.1.2. Analytical performance. The detection of analytes in the gel eluates of sliced gels is limited by the small aliquots generated. Highly sensitive detection techniques are thus required for detecting trace amounts of analytes. For example, Ding et al. [46] eluted their 0.45 × 0.45 mm gel squares in 40 μL of 1 mol L^{-1} NaOH and minimized sample dilution by only adding 15 μL of staining reagent to the eluate prior to analysis on a micro-well spectrophotometer. However, these samples are ~85-fold more dilute than a standard gel disk (~3.14 cm^2 analyte-loaded gel area) eluted in 1 mL eluent [41]. Consequently, the detection limits in terms of porewater concentration for eluates of small gel slices will be substantially higher than those of bulk DGT measurements or LA-ICPMS. Gel slicing is therefore only recommendable when the target solutes are present in high concentrations. Analysis of trace analytes will hardly be possible by this procedure.

4.1.1.2. Computer imaging densitometry. Teasdale et al. [13] were the first to apply CID for quantifying the dark Ag_2S patches that develop on AgI gels upon contact with S^{2-} using standard office flatbed scanners [13,62]. After being dried in a vacuum gel drier, a scanned greyscale image acquired along with images of standard gels containing known amounts of sulphide are used to quantify the amount of sulphide bound to the DGT gel. Recently, a CID-based technique capable of measuring the phosphate distribution on Zr-oxide DGT gels was presented [48]. In this approach, the phosphate sorbed to the Zr-oxide phase is first stabilized by a heating treatment and afterwards stained by immersing the gel in a molybdenum-blue reagent, resulting in the formation of blue colour on the DGT gel.

Computer imaging densitometry has also been applied to measure Fe(II) and phosphate in DET gels [15,16,35,36,38]. Here, the sediment-exposed gel is overlaid by a second diffusive gel that was equilibrated with a staining reagent; *i.e.* ferrozine and acetic acid for the analysis of Fe(II) [15,16,35] or sulphuric acid, ammonium molybdate, potassium antimonyl tatrate and ascorbic acid for the determination of phosphate [36]. A chemical image of the target solute is formed by diffusive mixing and reaction of the analyte and the staining agent. Before the analysis the gel assembly is covered with transparent plastic sheets or glass plates to limit evaporation. After colour development for about 10–20 min a flatbed scanner is used to acquire an image of the analyte distribution. Recently, Cesbron et al. [38] presented a method for the simultaneous staining and analysis of Fe(II) and phosphate in a single DET gel. Here, the DET gel was placed between gels containing either a ferrozine or a molybdate blue reagent and subsequently a hyperspectral camera with a spectral resolution of 4.5 nm was used to concomitantly acquire images of the magenta and blue colour pattern that developed. As in sulphide determination, gels of known analyte concentration were used for calibration.

4.1.1.2.1. Resolution and scan time. Computer imaging densitometry is the fastest and least laborious approach for acquiring chemical images from DGT and DET. For scanned images, spatial resolution is limited by the scanner hardware. A modern scanner with an optical resolution of 6400 × 6400 dpi (dots per inch) has a resolution limit of ~4 μm. Cesbron et al. [38] reported a spatial resolution of ~60 × 60 μm for their hyperspectral images. However, the actual spatial resolution limit for the analyte distribution depends on lateral diffusion of the analytes either inside the DET gel or during passage of the diffusive layer in DGT applications. A spatial resolution limit of ~1 mm, taking diffusive relaxation in 1.3 mm thick DET/DGT multilayer gel sensors into account, was estimated in a recent paper on a DET CID technique [16]. The relative contributions of diffusive relaxation before the formation of the colour complex, and after complex formation remained however unclear. Recent results indicate that the diffusion of Fe-ferrozine and phospho-molybdate complexes might be strongly restricted in polyacrylamide gels and that diffusive relaxation before staining might be most important in determining the extent of relaxation [38]. The issue of spatial resolution and diffusive relaxation is further discussed in the Sections 4.1.4 and 4.1.5.

4.1.1.2.2. Analytical performance. Sulphide detections limits (LOD) of 2.5 and 4.2 nmol cm^{-2} have been reported [13,47], corresponding to environmental sulphide concentrations of about 0.16 and 0.27 μmol L^{-1} for DGT deployments at 20 °C for 24 h with 0.93 mm diffusion layer thickness (Table 1). The precision (RSD) on the blank signals was reported to be ~3% [13,47]. The CID-based phosphate DGT approach using Zr-oxide DGT gels had a phosphate detection limit of 6.7 nmol cm^{-2} (1.1 μmol L^{-1} for the mentioned DGT application conditions) and a precision of 0.2–7% [48].

A detection limit of 0.6 μmol L^{-1} and a precision <10% were reported for the colorimetric, two-dimensional determination of Fe(II) using DET [16], with a slightly higher LOD (4.1 μmol L^{-1}) including the inter-pixel standard deviation [35]. The analytical performance for colorimetric DET analysis of phosphate was similar with a LOD of 0.22 μmol L^{-1} and a precision of <5% [36]. Using a DET-hyperspectral camera setup, LODs of ~1 and ~2 μmol L^{-1} Fe(II) and phosphate were reported [38].

The reported upper concentration limits for the CID techniques are ~0.6 μmol cm^{-2} (sulphide) [13,47], 2000 μmol L^{-1} (Fe(II)) [35] and ~700 μmol L^{-1} (phosphate) [36].

4.1.1.3. Laser ablation inductively coupled plasma mass spectrometry. Multi-analyte images of DET/DGT gels for more than two analytes can only be obtained using microbeam techniques such as particle induced X-ray emission (PIXE) [11,34] or laser ablation inductively coupled plasma mass spectrometry (LA-ICPMS) [12,58]. PIXE is not discussed extensively in this review as only two very early studies applied this technique for the analysis of DGT gels. The limited use of this approach might be related to limited access to such instruments.

DGT gels have to be water-free for analysis with ICPMS, therefore they are usually dried in gel dryers under vacuum to minimize gel shrinking in the *x* and *y* dimensions [54,58]. Most LA-ICPMS applications measured elemental concentrations on DGT gels using quadrupole instruments, which are considered in the following [12,49–51,54–59,178].

4.1.1.3.1. Resolution and scan time. The applied spatial resolution is typically about 300 × 300 μm, which is considered sufficient for investigating solute dynamics in biogeochemical hotspots, although finer resolutions are possible. Very high resolution combined with a large field of view (several cm^2) result in analysis time of several hours to days, which can be problematic regarding the difficulty to maintain long-term signal-stability in ICPMS instruments. Both, line scans [12,51,54,178] and the more time-consuming spot ablation [56,58] have been applied for analysing DGT gels.

4.1.1.3.2. LOD. Detection limits ranging from 1 to 130 pmol cm^{-2} were reported for the LA-ICPMS analysis of Co, Ni, Cu, Zn, Cd and Pb on SPR-IDA gels [58,178], P, V and As on ferrihydrite gels [54,56] and As and Cu on a Zr-hydroxide-SPR-IDA gel [51]. Elevated LODs for Zn (330–1400 pmol cm^{-2}) on SPR-IDA gels were probably caused by sample contamination [178] and the high LOD for P (1097 pmol cm^{-2}) and Cd (348 pmol cm^{-2}) on Zr-hydroxide-SPR-IDA gel were presumably caused by the P and Cd background of the urethane-based hydrogel matrix [51]. LODs in line-scan mode [54,178] agree well with those of spot ablation [56,58], therefore

Please cite this article in press as: J. Santner, et al., Two decades of chemical imaging of solutes in sediments and soils – a review, Anal. Chim. Acta (2015), http://dx.doi.org/10.1016/j.aca.2015.02.006

the advantage of faster analysis in line ablation does not come at the expense of increased LODs. Porewater concentrations corresponding to these detection limits (for non-elevated LODs) are in the range of 0.14–3.51 nmol L^{-1} calculated based on a diffusive layer thickness of 0.014 cm, 24 h deployment time, and a diffusion coefficient of $6 \times 10^{-6}\ cm^2\ s^{-1}$.

4.1.1.3.3. Internal normalisation and analytical precision. In the first detailed study investigating the performance of LA-ICPMS analysis of DGT gels, samples containing internal standards were prepared by loading a second gel layer with Sc, In, Ba, La, Ce and Tb, placing this second gel underneath the actual sample gel and drying the two gels simultaneously [58]. This procedure resulted in inseparable, dry gel samples with a homogeneous distribution of internal standards. The laser settings were adjusted to ensure that the laser penetrated through both gel layers. Analytical precision (RSD) for the internal standards was ~10%, with Ba showing the best values. Indium, having a slightly higher RSD, was however chosen for further use as the natural background level of Ba was too high for its use as normalisation standard. The authors did not report a significant improvement to the analytical precision by using internal normalisation compared to analysis without internal standards, *i.e.* precision changed from 7 to 16% RSD before normalisation to 8–14% after normalisation.

^{13}C was shown to be a suitable isotope for internal normalisation in the LA-ICPMS analysis of SPR-IDA [178] and SPR-IDA-Zr-hydroxide [51] gels, and it was concluded that the preparation of In-doped, double-layer DGT gels is unnecessarily complicated. A direct comparison of the two approaches, however, was not performed. Stockdale et al. [56] used ^{57}Fe as internal standard for analysing oxyanions on a ferrihydrite gel as its mass was closer to most of the investigated analytes than that of ^{13}C. They reported increased precision (RSD decreased by up to 7.6%) after internal normalisation in eleven samples and decreased precision (RSD lower by up to 2.1%) in two investigated samples.

Relative combined standard uncertainties, calculated based on the individual uncertainties of calibration, the signal intensities of the sample and of blank correction, for similar ferrihydrite gels were reported to be <20% [54], with precision being <10%. However, in a more extensive consideration of the uncertainty budget of DGT-LA-ICPMS analysis we showed that relative combined standard uncertainties of up to 45% have to be expected for the analysis of SPR-IDA-Zr-hydroxide gels, with the major uncertainty contributors being the normalised signal and the intercept of the calibration [179].

4.1.1.3.4. Interferences. Oxide based spectral interferences in LA-ICPMS are generally reduced compared to liquid ICPMS due the absence of the liquid carrier matrix and the resulting reduced formation rates of interfering polyatomic species [180,181]. Oxide ratios, determined as CeO^+/Ce^+, of dried SPR-IDA gels were not detectable, indicating a very low oxygen and therefore water content of the dried DGT gels [58]. The formation of doubly charged species (Ba^{2+}/Ba^+) was found to be <2%. A very low contribution of N-based spectral interferences ($^{14}N^{16}O^{1}H$ and $^{15}N^{16}O$) to the signal of ^{31}P was found for LA-ICPMS analysis of dried ferrihydrite gels [54]. This contribution was small and constant in blank and standard gels and was thus accounted for by blank correction. To date no reports of severe spectral interferences in LA-ICPMS of DGT gels exist, however novel gels and analytes should be thoroughly tested for interferences.

4.1.1.4. LA multi collector sector field ICPMS. Bellis et al. [182] reported the analysis of $\delta^{34}S$ isotope ratios of sulphide sampled using AgI gels by multi-collector sector field ICPMS. Variations in the S isotopic composition in standard gels of 0.2 to 0.6‰ could be resolved. The precision of the laser ablation analysis was ~0.3‰, similar to that of liquid samples analysed on the same instrument. However, the accuracy obtained for gels containing ground reference material (NIST 8554 and NIST 8555) compared to the certified values was poor ($\delta^{34}S$ in DGT gels containing ground NIST materials deviated by 4–8.5‰ from accepted NIST values). This was possibly caused by the high ^{32}S content of blank gels or by variations in the instrument mass bias. While this approach is clearly fit for measuring relative changes in the isotopic composition of sulphide at high spatial resolution, the absolute determination of isotopic composition of sulphide using DGT requires improved accuracy.

4.1.2. Image generation

Although many image processing tools can be used for creating images of gel slice eluates or LA-ICPMS datasets, the free application ImageJ (National Institute of Health, Bethesda, MD, USA; http://imagej.nih.gov/ij/) is a practical, powerful software that can convert comma-separated value files (.csv) to images. Care should be taken to avoid pixel interpolation in all image resizing operations, which is by standard performed by many common image editing packages. Pixel interpolation might result in the smoothing of gradients and thereby creates artefacts during image data processing. The rawdata images measured using gel slicing, LA-ICPMS or PIXE are usually pixelated as their spatial resolution (~3 mm to ~50 μm) is, in contrast to CID and planar optode techniques, too coarse to allow for smooth images without visible pixels. Good example for pixelated, non-interpolated DGT and DET images measured using PIXE are provided in Davison et al. [11,34], a pixelated LA-ICPMS image is also given in Fig. 9b in this review.

4.1.3. Analyte binding by the diffusive gel

Both, the DET and DGT techniques assume that the hydrogel matrix does not bind the analyte ions. Several studies have, however, shown that this assumption is not always true. A very detailed analysis of gel-analyte interactions can be found in Davison and Zhang [183], therefore we only give a brief overview here.

Early tests showed that the DET measured concentration is in good agreement with the actual solution concentration for various ions (Fe^{2+}, Mn^{2+}, NO_3^-, Cl^-, SO_4^{2-}) at analyte concentrations >2–6 μmol L^{-1} [34,184], supporting the assumption of negligible analyte-gel interaction. However, Cd^{2+} concentrations in deployment solutions and in equilibrated gels only matched at ionic strengths (I) of >1 mmol L^{-1} for gels that were immediately used after production, whereas pre-hydrated and pre-conditioned gels (soaked in ~10 mmol L^{-1} $NaNO_3$) gave consistent results also at lower ionic strength [60]. This behaviour was attributed to the presence of (local) electrical charges in the gel matrix that affect the diffusion of ions through the gel. Other studies have confirmed these unexpected results for Cd^{2+} [185,186].

Detailed investigation of metal binding to the agarose-cross-linked polyacrylamide (APA) gel showed unexpectedly high DET measured concentrations at $I < 1$ mmol L^{-1} using unwashed gels which were attributed to a negative electrical charge caused by remaining polymerisation reactants [187]. In contrast, thorough washing and conditioning of the gel resulted in very low DET recoveries at $I < 1$ mmol L^{-1}, which was attributed to a slightly positive charge remaining on the gel after extensive washing. Preconditioning the APA gel after washing and deployment at $I > 1$ mmol L^{-1} resulted in reproducible and accurate analyte recoveries, however. In addition to such charge effects, specific binding of Co^{2+}, Ni^{2+}, Cu^{2+}, Cd^{2+} and Pb^{2+} to the APA matrix, to bis-acrylamide gels and to polyethersulfone filter membranes (Pall, Port Washington, NY, US) at low analyte concentrations

Please cite this article in press as: J. Santner, et al., Two decades of chemical imaging of solutes in sediments and soils – a review, Anal. Chim. Acta (2015), http://dx.doi.org/10.1016/j.aca.2015.02.006

irrespective of ionic strength has been observed [187,188], with Cu^{2+} and Pb^{2+} having the highest affinities for the gels. The capacity for binding trace metal ions was however low.

4.1.4. Characteristics and limitations specific to DET

4.1.4.1. Analyte binding to the hydrogel matrix. Diffusive equilibration in thin films (typically 0.4–0.8 mm thick) is a well understood, simple technique that accurately measures the porewater solute concentration. Equilibrium between the medium and the gel is reached in less than one hour after insertion into the sediment even for very thick (1 mm) gels [33]. Deviations from equilibrium can, however, occur [185–188]. Binding of analytes to the hydrogel matrix can result in considerable overestimation of porewater concentrations. Therefore DET applications at low analyte concentrations ($\leq$10 μmol L^{-1}) have to be made with care, especially at low ionic strength, as may be the case in freshwater sediments or specific soil types. At higher ionic strength, *i.e.* in marine sediments, no erroneous measurements for weakly binding analytes should occur.

4.1.4.2. Spatial resolution limits. The spatial resolution of DET is limited by two effects, both are associated with continual, omnidirectional diffusion (often termed 'diffusive relaxation') within the DET gel [16,34,38].

The first effect depends on the thickness of the DET gel that is used. A concentration gradient in a sediment that is in contact with a DET sampler is very accurately reflected in the surface layers of the gel. However, relaxation blurs the 'imprint' of the solute distribution in the DET gel depending on the distance from the sediment, hence the solute distribution 'imprint' on the far side of the gel is larger than in the sediment. Davison et al. [34] showed a widening of a sharp concentration gradient by about 2 mm throughout a 2 mm thick DET gel. As the extent of widening depends on the thickness of the gel, thinner gels are recommended if the geometry of the solute distribution should be accurately determined.

Secondly, diffusional relaxation also takes place after retrieving the DET sampler from the sediment, as the solute concentration in the gel begins to 'smear' as the contact with the sediment is lost. For retaining a 250 μm resolution, Fe and Mn need to be precipitated within 1–2 s, whereas 20 s suffice for a 1 mm resolution [34]. Mathematical modelling showed that a 1 mm wide concentration peak in a DET gel will only be at 60% of its original concentration and will have considerably widened already 160 s after the retrieval of the gel (Fig. 5). The spatial resolution limit of ~1 mm given for colorimetric DET methods [16] therefore seems optimistic given the 10–20 min colour development periods that are applied, even if the colour complex has negligible diffusivity in the DET gel [38]. This aspect should be investigated in detail if colorimetric DET data are used for interpreting small-scale features.

4.1.5. Characteristics and limitations specific to DGT

4.1.5.1. Analyte binding to the hydrogel matrix. Analyte binding to the diffusive gel is less problematic for DGT than for DET measurements. Ions binding to the gel matrix will prolong the establishment of a steady concentration gradient (and thus flux) through the diffusive layer as the analyte is removed from the liquid phase until the capacity of the diffusive layer is reached [189]. At this point, the flux through the diffusive layer will have the same magnitude as if no analyte was binding to the diffusive gel. The measured analyte concentration (c_{DGT} in Eq. (2)) will be underestimated by this retardation if short deployment times are used. This effect was found to have the largest impact for ions that

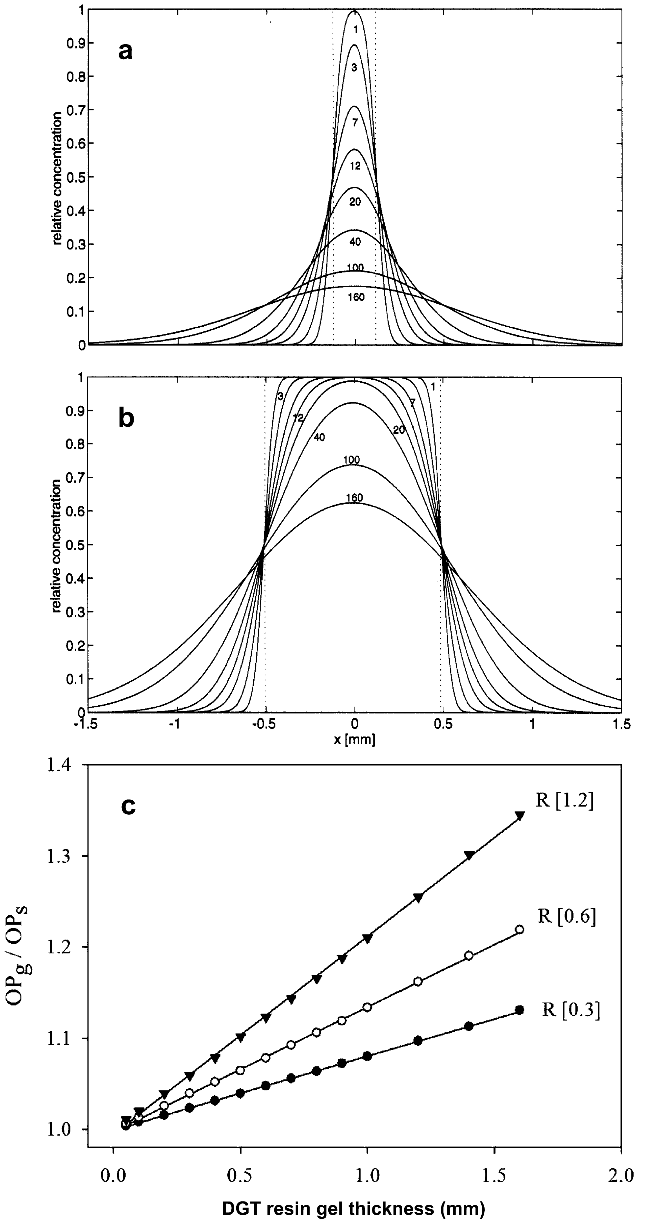

Fig. 5. Simulation of diffusive relaxation in DET and optode setups. Simulated concentration profiles for a hypothetical, initially (a) 250 μm and (b) 1000 μm wide concentration peak after recovery at various times (given in seconds) of relaxation (lateral diffusion) in a DET gel. The dotted lines represent the initial shape of the concentration peaks. These data indicate that reproducing the shape, *i.e.* the width and steepness of the concentration gradient, of a concentration feature requires chemical fixation, *e.g.* by precipitation of Fe(II) using NaOH in the order of 1–20 s after retrieving the DET gel from the sampled medium. Reprinted with permission from Davison et al. [34]. Copyright 1994 American Chemical Society. (c) Numerical simulation of the diffusive broadening of the O_2 penetration depth into sediment for different DGT resin gel thicknesses in a dual-layer DGT-optode setup (corresponding to Fig. 1d). OP_g/Op_s is the broadening ratio, where OP_g is the O_2 penetration depth measured by the DGT-covered optode and OP_s is the actual O_2 penetration depth in the sediment (OP_s). The simulation was performed for three sediment volume specific respiration rates R (given in μmol cm^{-3} s^{-1}). With increasing resin gel thickness the bias becomes larger, as the O_2 image blurs by lateral diffusion of O_2 in the DGT resin gel. The data underpin the importance of using thin gels for combined sensor setups. Reproduced with permission from Stahl et al. [55]. Copyright 2014 by the Association for the Sciences of Limnology and Oceanography, Inc.

Please cite this article in press as: J. Santner, et al., Two decades of chemical imaging of solutes in sediments and soils – a review, Anal. Chim. Acta (2015), http://dx.doi.org/10.1016/j.aca.2015.02.006

strongly bind to the gel matrix (Cu^{2+}, Pb^{2+}) at low concentrations and for DGT deployments with relatively thick diffusive layers [189]. For DGT imaging applications, where the diffusive gels are usually thin (200 μm), or even omitted and replaced by ultra-thin membranes (~10 μm), analyte binding to the diffusive gel matrix is expected to have only a negligible influence on the resolved solute distribution.

4.1.5.2. Spatial resolution and shape fidelity. As discussed, the spatial resolution of 2D DGT measurements is limited by the applied analytical approach. The resolution is generally in the range of 3 mm (slicing) to 4 μm (CID), (Section 4.1.1) [13,14].

Another limiting factor is diffusive relaxation, which, in contrast to DET, only takes effect during passage of the diffusion layer, before the analytes are fixed on the resin layer. Harper et al. [190] investigated how well the width of a concentration peak is reproduced by DGT with diffusion layer thicknesses >0.2 mm using numerical simulations. The minimum width of a concentration peak for being accurately reflected in a DGT measurement (defined as porewater peak width divided by DGT peak width >0.8) was shown to be 1.2 mm with a 0.3 mm diffusion layer. In another modelling study the width of DGT measured peaks produced by simulated microniches were very similar to porewater peaks with a diffusive layer thickness of 0.5 mm [191]. This obvious difference is likely associated with the different modelling approaches that were used in the two studies, one creating a concentration gradient only in the vertical direction in the sediment [190], whereas the other studied small, point sources [191]. However, the use of diffusive layers of ~100 [55] or even 10 μm [52] thickness should reduce relaxation to a point where it becomes negligibly small.

4.1.5.3. Interpretation of DGT results. DGT measurements can be interpreted as time-averaged solute flux into the sampler, f_{DGT} (Eq. (1)) or as time-averaged concentration at the sampler-medium interface, c_{DGT} (Eq. (2)). The value of c_{DGT} matches the bulk solution concentration, c_{soln}, if the solution is well-mixed, *i.e.* if no analyte depletion in the vicinity of the DGT sampler occurs, and if DGT-labile solute species dominate the solution composition [41,88].

In most soils and sediments the porewater solute concentration of analytes measured using DGT (*e.g.* transition element cations, oxyanions like phosphate) is controlled by sorption to solid surfaces or by precipitation–dissolution reactions [192,193]. However, sorption and precipitation may strongly reduce both, convective and diffusive solute transport. As a result, solute desorption is often governing the replenishment of the porewater concentration in response to solute removal by DGT. c_{DGT} therefore only matches the equilibrium bulk solution concentration (c_{soln}) if the desorption rate and the buffer power of the solid phase are high enough to maintain c_{soln} constant throughout the DGT deployment period. The ratio R,

$$R = \frac{c_{DGT}}{c_{soln}} \tag{3}$$

was used to define three possible scenarios for solute resupply for typical 24 h deployments [192,194]; (1) a sustained case where desorption is largely maintaining the solution concentrations ($R > 0.95$), (2) an intermediate case where desorption is not fast enough to maintain the bulk concentration ($0.95 > R > 0.1$) and (3) an unsustained case where resupply is by diffusion only ($R < 0.1$).

An additional effect specific to DGT chemical imaging is connected to the use of very thin diffusive layers (down to 10 μm). In theory (Eq. (2)), c_{DGT} is a linear function of the diffusion layer thickness. This is true if the solute uptake by the DGT resin gel is solely controlled by the diffusive gradient through the diffusive layer which is the case if the external solute concentration is constant. As discussed, this is likely not the case in porous media. If the analyte availability is controlled by desorption/dissolution, a reduction of the diffusion layer thickness and thus an increase in the potential DGT flux will not increase the actual DGT solute uptake linearly. In Fig. 6, bulk soil DGT measurements of labile P for different application periods using diffusive layer thicknesses of 0.095 and 0.001 cm are shown. In theory, the accumulated masses of P in the 0.001 cm devices should be 95 times higher than those in the 0.095 cm devices (Fig. 6a). However, this ratio ranges only from 2.1 (4 h deployment) to 1.3 (192 h) for the given data. As a consequence, c_{DGT} is 45–70 times lower in the 0.001 cm devices than expected according to Eq. (2). Another example for this effect is given in Lehto et al. [52].

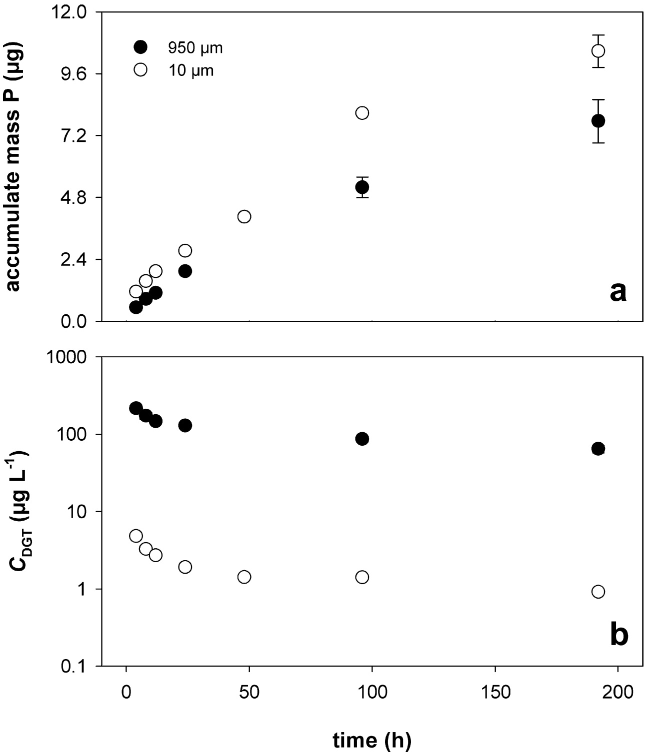

Fig. 6. Effect of diffusion layer thickness on the accumulated solute mass and on c_{DGT} in bulk soil DGT analysis. While the accumulated mass of P is 1.3–2.1 times higher when using a thin (10 μm) compared to a standard (950 μm) diffusion layer, the c_{DGT} concentrations are 45–70 times smaller for the thin diffusion layer because the accumulated mass is normalised to the diffusion layer thickness when calculating c_{DGT}. For further discussion see the text. Unpublished results of Andreas Kreuzeder and Jakob Santner.

Generally, DGT records solute mobilisation from the solid phase to the resin gel by introducing a solute sink into the sediment or soils, but not the actual porewater concentration. The true concentration cannot be inferred from c_{DGT}, with the exception of areas of locally increased solute release like microbial microniches, where modelling showed that the DGT measured concentration will always be between 62 and 87% of the true porewater maximum if the localised source continuously provides solute [191]. Localised differences in solute supply to the resin gel allow for the investigation of the effect of *e.g.* differences in the redox potential, solute uptake by plant roots, or solute release from hotspots of biological activity.

As c_{DGT} values measured in porous, sorbing media are no measurement of the true porewater concentration, and as the very small c_{DGT} concentrations obtained for thin diffusive layers in soils and sediment are not comparable to values measured with bulk samplers, it has been suggested to present DGT chemical images as fluxes [51], or as surface concentration on the resin gel [52] to avoid improper interpretations as porewater concentrations. This

Please cite this article in press as: J. Santner, et al., Two decades of chemical imaging of solutes in sediments and soils – a review, Anal. Chim. Acta (2015), http://dx.doi.org/10.1016/j.aca.2015.02.006

avoids incorrect comparisons of bulk soil c_{DGT} concentrations to c_{DGT} in images with thin diffusion layers.

4.1.5.4. Soil water content. While standard DGT procedures in soils operate close to water saturation, DGT can also be applied at lower soil water levels. It has been shown that the absolute amount of solute accumulated by DGT decreases with decreasing soil water content [195,196]. For DGT imaging in the rhizosphere of terrestrial plants we have found that a soil water content of ~50% to ~80% of the soil water holding capacity is adequate, as differential water distribution throughout the imaged region is unlikely. Close to or above the soil water holding capacity the O_2 levels in the rhizosphere can drop rapidly and cause redox artefacts like reductive Mn dissolution (Andreas Kreuzeder and Jakob Santner, unpublished results).

4.2. Planar optodes

4.2.1. Spatial resolution

The high spatial resolution and large fields of view (>400 cm^2) offered by planar optodes are two of the main advantages of this approach as compared to traditional microsensor measurements. The maximum spatial resolution is predominantly determined by the pixel size of the image sensor. For high-grade CCD cameras [30,85,124] this is typically 5.7 × 5.7 μm, for DSLR cameras [82,84] the pixel size is typically 11.4 × 11.4 μm when using the non-interpolated RAW file format. However, when using the JPEG file format (Joint Photographic Experts Group) the spatial resolution is boosted by pixel interpolation, artificially increasing the spatial resolution by a factor of 2. Furthermore, the JPEG format reduces the dynamic resolution from 12 to 8 bit, which represents a ~16-fold reduction [82].

The maximum spatial resolution derived from the characteristics of the image sensor is however merely theoretical as optical distortion in the lens, the optode sensor and/or the optical pathway will inevitable degrade the image resolution. Furthermore, the maximum resolution can only be achieved if the field of view is limited to the size of the camera's image sensor (20.7 × 13.8 mm–28.7 × 19.1 mm for standard DSLR cameras), in combination with the use of macro lenses with a 1:1 reproduction ratio.

In order to define the actual spatial resolution of a standard setup we did a series of tests with imaging resolution test targets (USFA 1951). We found that a Canon D1000 camera equipped with a high quality macro lens could maximally resolve structures 2–3 times time lager than the maximum theoretical resolution of 11.4 × 11.4 μm. This is in agreement with the observation of Strömberg and Hulth [74].

As for DET and DGT approaches, lateral diffusion of the analyte inside the sensor is another factor affecting the actual spatial resolution [85,197]. Based on mathematical modelling Fischer and Wenzhöfer [85] estimated that the spatial resolution limit of an O_2 optode is ~5 times the thickness of the sensing layer, therefore a 2 μm thick layer exhibits a theoretical resolution limit of ~10 μm. In this context, sensing layers with a thickness of 5–10 μm exhibit a spatial resolution limit higher or equal to the maximum spatial resolution that can be achieved by most imaging systems. Additional optical insulation layers, as required by some intensity-based imaging techniques, will further deter the actual spatial resolution that can be achieved. Light guidance in the sensing layer, support foil and container wall likewise decrease the optical resolution that can be achieved due to smearing of the emission light, these aspects are discussed in Section 4.2.9.

For most applications a spatial resolution in the range of ~100 × 100 μm will be sufficient to resolve the smallest dynamics of interest. Appropriate image resolution can be estimated using the Nyquist–Shannon sampling theorem which states that the sample resolution should be at a minimum two times higher than the requested resolution [198] – to resolve a 50 × 50 μm feature a minimum resolution of 25 × 25 μm should therefore be applied.

4.2.2. Temporal resolution of the imaging systems

Another key aspect of planar optode system performance is the temporal resolution at which images can be acquired.

4.2.2.1. Lifetime based systems. Lifetime based systems all rely on low noise, high sensitivity CCD cameras in order to capture the short-lived phosphorescence. Typical exposure times for these systems are in the range of 5–20 μs, and are controlled by an electronic shutter [115,170,199,200]. The signal intensity for these short exposure times is usually low, therefore multiple exposure time frames are integrated to record a single image and thereby increase the image intensity. Depending on the integration time, the total image acquisition time for a single image is ~1–2 s [99]. These images typically have an unacceptably low signal-to-noise ratio. For improving the signal-to-noise ratio, most studies apply multiple image averaging (4–16), leading to a final acquisition time of 10–40 s for a composite image [115]. In lifetime-based systems the temporal resolution can be increased by applying a pixel binning procedure [115,170,199]. Binning is the combination of two or more image sensor pixels to form a new super-pixel prior to readout and digitizing. Binning increases the apparent sensitivity of the image sensor, thereby reducing the need for image integration, but at the same time results in reduced spatial resolution [115]. The binning of 2 × 2 pixels will result in a theoretical increase in sensitivity of a factor of 4, but a reduction of the maximum achievable pixel size by a factor of 2.

4.2.2.2. Intensity-based systems. Intensity-based systems generally apply lower-sensitivity CCD or CMOS cameras which require longer exposure times, typically ranging from 0.1 to 1 s, but up to 30 s have been reported [163]. Similar to lifetime systems the signal-to-noise ratio is improved by averaging multiple images and by pixel binning. For standard DSLR cameras, binning can only be performed post image acquisition and does not allow for increased sensitivity, but the procedure is used to decrease image noise. The exposure time of DSLR cameras can be reduced by increasing the ISO equivalent, which is a measure of the signal gain, however, this comes at the expense of increased image noise. For a moderate increase in ISO (*e.g.* 100–400) the increase in noise is, however, often negligible. Since DSLR cameras typically have larger image sensors with more pixels compared to the lifetime-based systems the post-acquisition binning procedure often has minimal effect on the true spatial resolution of the image, but is an effective way to reduce image noise. Overall, for most practical purposes hardware performance rarely limits the requested temporal resolution of planar optode measurements.

4.2.3. Response time of planar optode sensors

The response time of a planar optode depends on the time it takes for the analyte in the sensing layer to reach thermodynamic equilibrium with the surrounding medium. For fast sensors the thickness of the sensing layer has to be minimized, which necessitates bright indicators to ensure sufficient signal output [70,102]. The sensing layer for most O_2 sensors is between 10 and 40 μm thick [105] and 90% response times are reported to be in the range of 5–10 s. Optode sensors coated with black silicone for optical insulation exhibit slower responses of up to 30–60 s [82,201]. Response times of up to one minute are generally not a limiting factor as time lapse studies rarely require faster sensor response. However, fast sensor response times are sometimes necessary for studies of phototrophic communities [109,202]. In

Please cite this article in press as: J. Santner, et al., Two decades of chemical imaging of solutes in sediments and soils – a review, Anal. Chim. Acta (2015), http://dx.doi.org/10.1016/j.aca.2015.02.006

such cases, clever combination of ultra-bright sensors and fast imaging techniques can help to realise the required total system response times of 1–2 s [70,102].

pH and pCO_2 sensors are generally slower than O_2 sensors. For the pH sensors described by Zhu et al. [123], the response time was 1 min for a 90% signal response after a pH shift from 6 to 8, while the 100% response time was 2 min. This seems typical for most pH sensor designs [82,124,203]. However, Hulth et al. [18] used an only 5 μm thin cellulose matrix and reported an estimated response time of only ~5 s. Planar pCO_2 sensors are reported to have response times ranging from 10 to 150 s [20,72], while the response times for NH_4^+ sensors are in the order of 3–4 min [133,134]. For most practical applications in soil and sediment the sensor response times does not appear to be a limiting factor.

4.2.4. Dynamic range

O_2 sensors for planar optode imaging all show a broad dynamic range making them applicable for O_2 levels from 0% to above 100% air saturation. The most widely used indicators for planar optode imaging (PtTFPP and PtOEP) have a nonlinear signal response when immobilized in polystyrene matrices, with highest sensitivity at low O_2 concentrations and a moderate to low sensitivity at concentrations around 100% air saturation. This makes the sensors less useful for studies on photosynthetic systems which typically exhibit O_2 supersaturation. However, by substituting the matrix with a polymer of lower O_2 permeability such as PSAN poly(styrene-co-acrylonitrile), the dynamic range can be increased significantly – in our experience up to O_2 levels of ~200% air saturation, for both, lifetime and intensity based measurements. By applying matrices with higher permeability such as ethyl cellulose or silicone, the dynamic range can be reduced, facilitating sensors with high sensitivity at low O_2 concentrations [95]. For lifetime based measurements both, Ru-dpp and Ir(III) sensors immobilized in polystyrene can effectively be applied in environments with O_2 supersaturation, as they retain a relatively high sensitivity across a wider dynamic range (Fig. 3). When immobilized in polystyrene, both PtTFPP and PtOEP show a ~60% decrease in luminescent lifetime, for an increase in O_2 level from 0 to 50% air sat. For the same increase in O_2, the lifetime of Ru-dpp and $Ir(Cs)_2(acac)$ only decreased by ~25 and ~13%, respectively [70].

The dynamic range of pH sensors is mainly determined by the acid dissociation constant (pK_a) of the luminophore. The dynamic range is typically ±1.5 pH units of the indicator's apparent pK_a [204]. HPTS in free solution has a pK_a of 7.31 [75], but the apparent pK_a of the immobilized indicator is usually lower [127]. For HPTS-based planar optodes the reported apparent pK_a ranges from 7.06 to 7.47 [75,82], with a reported dynamic range of pH 5.5–9.5 [18,75,82,123], depending on the specific sensor design. For DHFAE-based sensors [124,126] the apparent pK_a is around ~8.3 and the dynamic range is 7.2–9.3 [124,126], an ideal range for most marine applications.

The common pH range of soils (pH 4–8.5) is lower than that of marine environments; therefore HPTS and DHFAE based sensors can only partly cover the relevant pH range for soils. DClFE (2,7-dichlorofluorescein octadecylester) [205] with an apparent pK_a value of ~6.2 and a pH range of ~4–7.5 in freshwater might be a good candidate for soil. In a recent, unpublished application we have found that DClFE immobilized in Hydromed D4 shows a dynamic range of pH 5–7.5. In general it should be noted that the apparent pK_a of all fluorescent pH indicators is affected by the immobilization matrix and the ionic strength of the medium.

The dynamic range of the few pCO_2 sensors available was reported to be ~0 to 40 hPa [20,72,122]. The dynamic range for the NH_4^+ sensor was reported to be in the range of 10 μmol L^{-1}–100 mmol L^{-1} [133]. The dynamic range of the H_2S sensors described by Zhu and Aller [21] is ~4–3000 μmol L^{-1}, depending on the amount of immobilized indicator.

4.2.5. Sensor stability

Sensor stability during storage or long-term measurements is important for high-fidelity measurements. O_2 sensors based on polystyrene are generally found to be mechanically stable and exhibit no loss of sensitivity when stored in the darkness for months [99]. The main reason for sensitivity loss in O_2 sensors is photobleaching or leaching of the indicators from the matrix, however many indicators show excellent photostability at conditions relevant for standard applications (Table 2).

PtOEP indicators, which are reported be prone to photobleaching [116,206] have however, been applied for several months for imaging at 1 h intervals without notable bleaching effects [115]. It should be noted that photobleaching has a greater effect on intensity based imaging than imaging based on luminescence lifetime, and that photobleaching in anoxic conditions for some sensors is greater than in oxic conditions with ongoing O_2 quenching [70].

Photostability for HPTS is reported to be high [75,122], whereas fluorescein derivatives (*e.g.* DHFAE) are more prone to bleaching [124,126]. In marine sediments, planar optode pH sensors based on indicators immobilized in cellulose acetate and polyvinyl alcohol matrices are reported to be stable for weeks to months [18,72] even though such matrixes are reported to swell due to water uptake [67,207]. In contrast, sensors based on Hydromed D4 matrix show reduced stability, rendering them useful for less than one week [110,124]. This reduction in stability is most likely caused by indicator leaching out of the sensing layer or by the accumulation of reduced chemical species in the sensor matrix.

The few pCO_2 sensors applied to date show stabilities comparable to their pH equivalents, *i.e.* in the order of several weeks [20,72]. NH_4^+ sensors have also been applied for weeks with little change in sensitivity [74,134]. In some cases signal drifts can be compensated for by a time dependent calibration correction [74,120].

As already mentioned, sensor performance can be affected by indicator leaching out of the sensor matrix. Leaching of O_2 indicators from polystyrene is reported to be no problem due to the high solubility of the indicator in this matrix [208]. However, indicator leaching from pH sensors is more problematic, especially from hydrogel matrices [124,131]. Leaching of DHFAE and DHFA from Hydromed D4 resulted in a decrease in sensor absorbance of 11.2% and 18.1%, respectively, during a 10 day period. HPTS showed no significant leaching from a cellulose acetate matrix [18], however, Hakonen and Hulth [120] observed leaching from ethyl cellulose, resulting in an increase of the apparent pK_a of the sensor. In some cases, leaching of pH indicators was overcome by covalently linking the indicator to the matrix polymer [75,209,210]. For HPTS-based pCO_2 sensors no indicator leaching has been reported.

Prolonged deployments of planar optodes sensors in biologically highly active systems (*e.g.* wastewaters) may result in biofouling of the sensor surface [18], which can cause erroneous determination of the analyte concentration and decreased sensor response time. Biofouling problems can be significantly reduced by coating the sensor surface with an anti-fouling layer to prevent surface growth [211].

4.2.6. Interferences

Temperature interference is observed for all luminescence indicators and has to be compensated for if the temperature cannot be kept constant [150]. Temperature interference on O_2 optodes is mainly caused by the temperature dependence of the O_2 permeability of the sensor matrix and only to a lesser extent by

Please cite this article in press as: J. Santner, et al., Two decades of chemical imaging of solutes in sediments and soils – a review, Anal. Chim. Acta (2015), http://dx.doi.org/10.1016/j.aca.2015.02.006

the temperature sensitivity of the indicator. An overall decrease in luminescent signal intensity is observed as temperature increases (Fig. 3). For PtTFPP immobilized in polystyrene Borisov and Klimant [70] estimated that without temperature correction, O_2 levels were affected by an error of 1.7% air sat. $°C^{-1}$ at 85% air saturation, while the error was only 0.22% air sat. $°C^{-1}$ at 12% air sat. For Ru-dpp errors of 2.6% and 2.0% air sat. at the same conditions were found. Similar errors were reported by Rysgaard et al. [111], who also demonstrated a decline in the luminescent lifetime of 0.3% $°C^{-1}$ for Ru-dpp in polystyrene.

The widely used pH indicator HPTS shows a decrease in excitation light absorption in both, the protonated as well as the de-protonated form as temperature increases [75], leading to an overall decrease in luminescent intensity. In this case, the ratiometric intensity imaging procedure acts as temperature normalization. Therefore, the overall luminescent intensity of the HPTS optode was temperature-insensitive from 5 to 40 °C because the relative intensity change due to temperature was similar for the two measured luminescent wavelengths, thereby keeping the intensity ratio constant [75]. However, ratiometric sensors with two luminescent dyes (*e.g.* reference and indicator) will most likely not show such insensitivity to temperature variations due to potential differences in the temperature response of the two dyes. The fluorescein derivatives DHFA and DHFAE also exhibited a decrease in luminescent intensity with increasing temperature while their apparent pK_as were observed to increase [131]. These counteracting trends largely eliminated the need for temperature compensation in the range of pH 5.5–8 for temperatures deviations of less than 5 °C from the calibration temperature. Similarly, Rudolph et al. [127] found no need for temperature compensation in the range of 19–25 °C for the fluorescein derivate 5-hexadecanoylaminofluorescein. HPTS-based pCO_2 sensors showed considerable decreases in the luminescent intensity in response to increasing temperature [20,72], which has to be accounted for in a dynamic measuring environment.

Systematic errors caused by temperature changes can be corrected for by applying temperature compensation, either using independent temperature measurements [212,213] or by using an internal, luminescent temperature-sensitive reference [214]. For applications where large temperature inhomogeneities across the planar optode exist, temperature has to be mapped to perform temperature compensation. Planar optodes for the simultaneous measurement of *e.g.* O_2/temperature and pH/temperature have been developed for this purpose [145,166,215,216]. These dual sensors will be essential for studying O_2/pH dynamics in sea ice or hot springs, where steep temperature gradients can exists. A simple alternative to luminescence-based temperature compensation might be the use of thermal imaging cameras.

O_2 planar optodes do not exhibit interference to any environmentally relevant solutes, mainly because the indicator is immobilized in an ion-impermeable matrix. Although gaseous sulphur dioxide (SO_2) and gaseous chlorine (Cl_2) have been reported as sources for interference [217], interferences other than temperature can be neglected for most practical applications.

Due to their ion-permeable matrix, pH optodes are more prone to interferences. The major source for interference are variations in the ionic strength in the external medium [218]. For the HPTS-based pH optode presented by Zhu et al. [75] the effect of increasing ionic strength was an increase in the apparent pK_a of the indicator. This increase was nonlinear, and an increase in ionic strength beyond 50 mmol L^{-1} did not change the apparent pK_a further [72,75]. We have found a similar result for HPTS immobilized in Hydromed D4.

DHFA optodes also showed an increase in the apparent pK_a with increasing ionic strength [126]. Sensors based on DHFAE or 6,8-dihydroxypyrene-1,3-disulfonic acid (DHPDS) show relativity little interference from ionic strength (Fig. 4) [73,126,219] and are recommended for applications where insensitivity to changes in the ionic strength is critical. Common dissolved ion species like NH_4^+, Fe^{2+}, Mn^{2+} and HS^- have been shown to not interfere with the pH signal from indicators immobilized in PVA, ethyl cellulose or cellulose acetate matrices [18,75,83].

Similar to O_2 sensors, pCO_2 sensors are reported to have only few problems with interferences, largely due to the silicone layer acting as a barrier for dissolved ionic species [122]. However, the occurrence of H_2S and NH_3 can affect the signal, as these species can diffuse across the silicone layer in the gas state [20,72]. For H_2S concentrations below 20 μmol L^{-1} interferences can be neglected, but at concentrations >100 μmol L^{-1} interferences can be severe [72]. For NH_3, concentrations of up to 600 μmol L^{-1} were found to have insignificant effects on pCO_2 measurements [72].

To date only one type of NH_4^+ sensor has been presented, which is insensitive to pH changes in the range of pH 6–7.8 but shows interferences from ionic strength similar pH sensors [132,133].

The H_2S sensor presented by Zhu and Aller [21] showed no interference from ionic species due to the protection of the sensing layer by a silicone membrane. The environmentally relevant gasses O_2, N_2, CO_2, and NH_3 did also not interfere with the H_2S signal.

4.2.7. Calibration

The correlation between luminescence and analyte concentration is for most planar optodes nonlinear (Figs. 3 and 4). O_2 planar optodes are typically calibrated using the modified Stern–Volmer equation [66,170,220],

$$\frac{\tau}{\tau_0} = \frac{I}{I_0} = \frac{R}{R_0} = \left[\alpha + (1-\alpha)\left(\frac{1}{1+K_{sv}\times C}\right)\right] \tag{4}$$

where τ is the phosphorescent lifetime at the O_2 concentration C, τ_0 is the lifetime in the absence of O_2, K_{SV} is the Stern–Volmer constant, and α is the non-quenchable fraction of the luminescent signal [66]. For intensity and ratiometric imaging approaches τ/τ_0 is replaced by the signal intensity, I/I_0 or the intensity ratio R/R_0. Typical calibration curves for Ru-dpp, PtTFPP and $Ir(C_s)_2(acac)$ are shown in Fig. 3. For determination of K_{sv} and α a 4–6 point calibration is usually performed [70,82,161]. The optode is typically calibrated before the deployment to determine K_{sv} and α – these constant are later applied to the recorded images to calculate the O_2 concentration using the rearranged Stern–Volmer equation (Eq. (5)):

$$C = \frac{\tau_0 - \tau}{K_{sv}\times(\tau - \tau_0\times\alpha)} \tag{5}$$

If the recorded images contain areas of known O_2 concentration, *e.g.* anoxic sediment and fully air saturated water, a two-point calibration can be carried out post measurement.

Calibration curves for pH sensors used for planar optode imaging typically show a classical sigmoidal response. The response can in most cases be fitted with a four parameter curve fit [82,120,124]:

$$I = I_0 + \frac{a}{1 + e^{-(\mathrm{pH}-\mathrm{p}K_a)/b}} \tag{6}$$

where I is the intensity at a given pH, I_0 is the minimum intensity, pK_a is the apparent acid dissociation constant of the indicator, and a and b are fitting constants describing the difference between asymptotic minimum and maximum of the sigmoidal function and the Hill slope, respectively. For ratiometric imaging approaches I and I_0 are replaced by R and R_0. For determining these curve parameters a 6–10 point calibration that covers the expected pH range is usually performed [18,75,127]. Prior to sensor deployment

Please cite this article in press as: J. Santner, et al., Two decades of chemical imaging of solutes in sediments and soils – a review, Anal. Chim. Acta (2015), http://dx.doi.org/10.1016/j.aca.2015.02.006

all four constants have to be determined by external calibration for subsequent image calibration.

As for most O_2 sensors the calibration curves for pCO_2 sensors have the highest sensitivity at low concentration and a signal that approaches the upper dynamic range limit asymptotically [20,72,122].

The NH_4^+ sensor presented by Strömberg and Hulth [133] showed a sigmoidal intensity-concentration response which could be approximated linearly in the analyte concentration range from 10 to ~250 μmol L^{-1}. The H_2S sensors presented by Zhu and Aller [21] were calibrated using a modified Stern–Volmer equation as described above.

4.2.8. Sensitivity and precision

4.2.8.1. Sensitivity. Sensitivity is defined as incremental signal response per unit increase in analyte concentration. Generally, sensitivity is given as slope of the calibration line. For O_2 optodes, this leads to varying sensitivity over the calibration range commonly with the highest sensitivities at low O_2 concentration. Borisov and Klimant [70] compared the sensitivity of O_2 optodes based on PtTFPP, $Ir(Cs)_2(acac)$ and Ru-dpp indicators immobilized in polystyrene and found that PtTFPP had sensitivities 2.5 and 1.9 times higher than Ru-dpp and $Ir(Cs)_2(acac)$ in the range from 0 to 100% air sat., respectively (Fig. 3).

Similar to the sensitivity, the resolution is determined by the shape of the response curve, generally leading to higher resolutions at lower O_2 concentrations (Fig. 3) [70]. At low O_2 concentrations (12% air sat.) PtTFPP had a 3-fold higher resolution than $Ir(Cs)_2(acac)$ and a 7-fold higher resolution than Ru-dpp. At higher O_2 concentrations (82% air sat.) the resolution of PtTFPP was only 1.8 times higher than that of $Ir(Cs)_2(acac)$ and 1.4 times than that of Ru-dpp. A comparison of PtOEP and Ru-dpp in a lifetime-based planar optode system demonstrated increased sensitivity of PtOEP compared to Ru-dpp at 80% air sat. [115].

Limits of detection of planar optodes are often not reported in the literature. In our experience the LOD of PtTFPP in polystyrene is around 2–3 μmol $O_2\,L^{-1}$, calculated as 3 times the standard deviation across an optode area of 50 × 50 mm under anoxic conditions. For $Ir(Cs)_2(acac)$ immobilized in polystyrene we have found LODs in the range of 6–8 μmol L^{-1}. As noted previously the dynamic range, but also the sensitivity of optical sensors can be tuned by applying matrices with different analyte permeability. For example, Borisov et al. [221] reported a trace O_2 sensor for which PtTFPP was covalently immobilised on silica-gel particles, resulting in a sensor with a LOD below 0.05 μmol L^{-1} and an upper dynamic range limit of 15 μmol L^{-1}.

pH sensors have the highest sensitivity in a pH range of $pK_a \pm 0.5$ pH units, where the calibration curve is usually steepest and quasi-linear [82]. Similar to most O_2 optodes pCO_2 and NH_4^+ sensors generally show the highest sensitivity at low concentrations [20,131]. The detection limit for the NH_4^+ sensors was reported to be ~10 μmol L^{-1} [133]. The LOD of the nanoparticle-enhanced NH_4^+ sensor is considerably lower with 119 nmol L^{-1} [222]. For the pCO_2 sensors described in the literature no LOD was reported. For the H_2S sensor reported by Zhu and Aller [21] the LOD was determined to be 4 μmol L^{-1}.

4.2.8.2. Precision. Precision is defined as the within-run standard deviation of the sensor signal when exposed to a homogeneous medium. The precision of planar optode measurements is influenced by the sensor signal response, the signal to noise ratio of the imaging system and by the homogeneity of the sensor. It is important to note that values of precision and accuracy are predominantly based on short term measurements in the orders of hours or on single calibration curves [73,75] and therefore do not take gradual loss of sensitivity and calibration drift into account.

The precision and accuracy of O_2 planar optodes is generally comparable to or surpassing that of traditional microsensors [17,115]. The precision of PtTFPP, $Ir(Cs)_2(acac)$ and Ru-dpp optodes was found to be in the low percent range [70], Oguri et al. [115] reported an accuracy of ±1.1 μmol L^{-1} at 0% air sat. and ±20 μmol L^{-1} at 80% air sat. for a PtOEP based sensor immobilized in polystyrene. For $Ir(Cs)_2(acac)$ we have found an accuracy of ±4.7 μmol L^{-1} at 0% air sat. and ±8.3 μmol L^{-1} at 80% air sat., demonstrating the improved performance at higher O_2 concentrations.

For pH optodes the reported values of precision are typically better than 0.02 pH units across the dynamic range [123], accuracy was reported to be better than 0.04 pH units [73]. For the HPTS sensors presented by Zhu et al. [75] the precision increased from ~13% at pH 4.5 to ~5% at pH 8.6. These figures are comparable to those of conventional pH electrodes. The precision of pCO_2 sensors was better than 0.3 hPa across the dynamic range with the highest accuracy (0.01 hPa) at pCO_2 concentrations of 1.58 hPa [20,72].

Sensor drift and interference from changing temperature and ionic strength during deployments can to some degree be compensated for by repetitive calibrations [74]. This was done for a NH_4^+ sensor where a time correlated pixel-by-pixel calibration scheme was applied over a 10 day experimental period. This correction improved the precision and reduced bias. At 250 μmol L^{-1} NH_4^+ the bias was reduced from −14% to −2% and the precision improved from 24% to 5% [74]. A similar correction protocol, which improved the precision considerably, was applied to pH sensing [83].

Generally, frequent calibration is highly recommended during longer experimental studies (days) and during measurements in dynamic environments. It should be noted that sensor performance is not only dependent on the sensor but is also influenced by the instrumentation and imaging approach [71,115]. Therefore appropriate instrument tuning is required for optimal performance. For instance, Oguri et al. [115] increased the precision of 2D O_2 measurements ~3-fold by increasing the camera bit resolution from 14 to 17 bit during lifetime based interrogation of a PtOEP-based sensor.

4.2.9. Light guidance

Light guidance in the sensor assembly (transparent wall, sensor support foil and sensing layer) can lead to smearing of the analyte signal as the luminescent signal from one part of the image can travel to other parts of the image [4,85]. The problem arises due to light scattering at boundaries of materials with different refractory index *e.g.* the interface between sensor support foil and sensing layer [223].

Light guidance is most severe when areas of high luminescence enclose a small area with low luminescence – for example an oxic macrofauna burrow surrounded by anoxic sediment or a root leaking O_2 into anoxic soil. This effect does not only affect the spatial resolution as a result of signal smearing, but also, and more importantly, affects the luminescence signal and thereby the measured concentration, as demonstrated in Fig. 7. To demonstrate light guidance, the optode area exposed to excitation light was reduced stepwise from 100% to 12%, however the burrow was kept illuminated at all times. As the excited area was reduced, less luminescence light from the bright anoxic sensor area was guided into the less bright oxic sensor parts, resulting in an increase of the measured O_2 level at the centre of the burrow from 55% to 64% air sat. This example demonstrates that light guidance can affect the quality of optode images significantly, even over long distances of mm to cm.

Several approaches can be applied to minimize the problem of light guidance: (1) Less bright indicators can be used such as Ru-

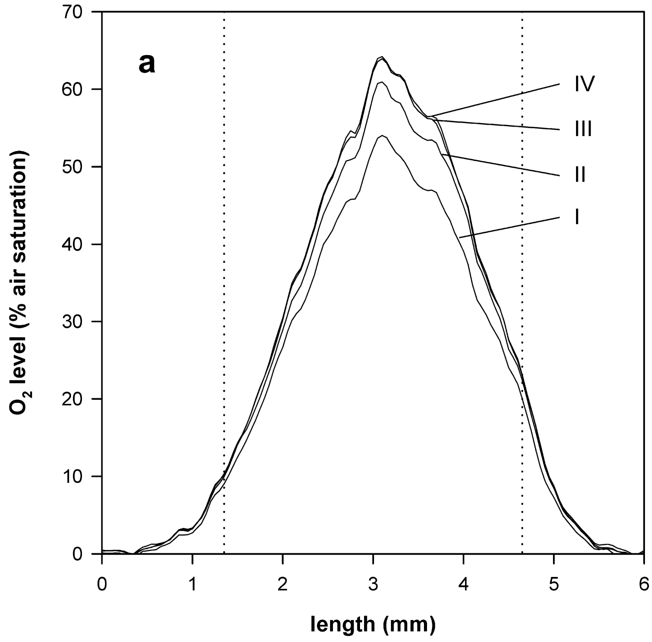

Fig. 7. Light guidance in an O_2 planar optode. O_2 profiles across an artificial worm burrow, realised by an air-filled, O_2-permeable teflon tube (O.D. = 3.3 mm, position indicated by the dashed lines) buried in sediment. The optode image corresponding to profile I was taken with the entire optode area being illuminated by the excitation light. For the images corresponding to profiles II–IV the optode foil was shaded so that only 37%, 15% and 12% of the optode area were excited. The respective profiles were extracted from the same location along the burrow, which was fully illuminated in all images. The apparent O_2 level at the centre of the burrow increases from 55% to 64% air saturation as the excited optode area is reduced. This apparent concentration increase is caused by light guidance in the optode assembly. Without optode cover (profile I) a large amount of luminescent light from the surrounding anoxic sediment travels towards the region of interest (*i.e.* the burrow) and increases the obtained signal in this region, thereby reducing the apparent O_2 level. By covering the optode outside the region of interest this effect is reduced, resulting in higher O_2 concentrations along the profiles II–IV. The images were recorded with a five second interval. Images are recorded with a colour ratio metric imaging approach [82] using a 1%/2% PtTFPP/Macrolex yellow dye mix [121]. Unpublished results of Morten Larsen and Ronnie N. Glud.

dpp or $Ir(Cs)_2(acac)$ instead of PtTFPP, as used in this demonstration, (2) the wall of the aquarium/rhizotron should be kept relatively thick (≥10 mm) to increase attenuation of the scattered light and limit the spatial crosstalk, (3) the area exposed to the excitation light should be minimized in order to minimize the amount of light that “travels” inside the optode assembly and (4) the planar optode support foil can be omitted by coating the sensing layer directly onto the wall. The thin support foil favours light guidance as there is little attenuation of scattered light and therefore relatively long-distance optical cross talk. Furthermore, the sensor chemistry can be coated onto fibre-optic face plates (FOFP) [85,97], which transfer a distortion-free image from one side of the FOFP to the other, as light transmission is only possible perpendicular to the FOFP surface planes. The use of FOFPs is the most effective way to eliminate optical cross talk, but commercially available FOFPs are generally small (70 × 50 mm) – thus limiting their application to relatively small areas [85].

4.3. Image analysis and interpretation

Interpretation of solute distribution images and the concise presentation of results can be complicated. Single images often contain much information especially in heterogeneous substrates. While DGT and DET images obtained by slicing only contain some hundred pixels, DGT images measured by LA-ICPMS consists of many thousands of pixels, while optode images, but also DGT/DET CID images, contain typically >1–6 million pixels [12,16,46,77,82,83]. Non-trivial data interpretation and presentation is particular obvious when studying conditions around complex structures like roots [12,59], animals [108], microbial hotspots [13,62] animal burrows [20,75] or wave ripples [99,224].

The translation of image data to quantitatively interpretable data is usually necessary for the detailed interpretation of any given phenomena. Optode images are often processed using ImageJ, Matlab or similar software packages [77,82,83] which allow for the simultaneous processing of image series. The information contained in image time series can be extracted as average area concentrations [225,226], as the size of an area with a specific solute concentration [225,226], solute flow patterns [83,227] or single pixel concentration profiles [82,99,228]. Although single pixel profiles contain only a fraction of the information compared to the original image, profiles are useful to highlight small-scale variability and simplify the calculation of solute release or consumption rates. Such calculations are especially useful for *e.g.* the estimation of radial O_2 loss from plant roots [225,226] or the diffusive solute exchange in sediments [86,228]. The interrelation of the biogeochemical behaviour of different solutes requires the analysis of solute correlation patterns. Williams et al. [59] used this approach to show differential solute mobilisation and immobilisation at a rice root apex and a microbial hotspot in submerged soil. In addition to interpreting the biogeochemical information in solute images, information on the abundance and geometry of biogeochemical features can be analysed. For example, Widerlund and Davison [64] have analysed the abundance, size and shape (circularity) of microbial niches in lake sediments in DGT images.

4.4. Distortion of the natural diffusion geometry by planar sensors

An important consideration when interpreting results of planar solute sensors is that the measurements are performed along a wall. This ‘unnatural’ physical barrier to diffusion transforms the undisturbed 3D diffusion geometry around microniches, burrows and roots. Images acquired using planar optodes and DET gels, which are based on equilibrium of the solute concentration in the external medium and the sensor matrix, will tend to enhance microniche structures and provide widened images of the analyte distribution around any features releasing or consuming the analyte. Similarly, in DGT imaging, where the analyte is quantitatively bound by the resin gel, image distortion by introducing a wall may occur. Sochaczewski et al. [191] showed in a modelling study that trace metal distributions around microbial microniches in sediments, may both, be widened or shrunk in a DGT image. The data of Santner et al. [12], who simulated a DGT imaging application on roots, also suggested that the recorded solute image may be widened. If the geometry of the studied features in soil or sediment is well defined, simple diffusion models can be used to correct or account for the presence of this impermeable barrier [4,80,225,229]. Without further, detailed investigation of the effects of altering the 3D diffusion geometry, potential distortions in case of complex geometry can only be carefully acknowledged when interpreting DGT, DET and planar optode images.

5. Applications

5.1. DGT and DET

High-resolution imaging using DET and DGT has provided unique insights that lead to improved understanding of

Please cite this article in press as: J. Santner, et al., Two decades of chemical imaging of solutes in sediments and soils – a review, Anal. Chim. Acta (2015), http://dx.doi.org/10.1016/j.aca.2015.02.006

biogeochemical processes, especially of the importance of microbial niches in aquatic sediments. Some selected examples are presented and discussed below.

5.1.1. Sediment biogeochemistry

Davison et al. [11] showed the simultaneous release of Mn and Zn at sub-mm scales and the highly localised co-mobilisation of Fe (II) and As in a river sediment, which strongly suggested that the release of the latter two elements was caused by microbial activity in a confined hotspot. This first application of a high-resolution, 2D DGT technique demonstrated the necessity to measure at sub-mm spatial resolution to be able to resolve and understand solute dynamics in surface sediments.

A study on Fe(II) and sulphide distributions around roots of *Zostera capricorni* showed shifts in the Fe(II) concentration from generally low concentrations during daytime to high concentrations near the sediment water interface (SWI) and high sulphide concentration at depths >8 cm in the sediment at night. This presumably reflected the consequences of diurnal shifts in the O_2 release from the roots [53]. The study documented that the redox conditions and especially the sulphidic environments in rhizospheres were much more dynamic than previously anticipated.

Using combined colorimetric DET–DGT techniques, Robertson et al. [37] investigated the complex distributions of Fe(II), sulphide and phosphate in a temperate estuarine sediment. Unexpectedly, the data documented the coexistence of dissolved Fe(II) and sulphide in sediments containing particulate organic matter and macrophyte roots [37]. A similar study showed the concomitant release of sulphide and phosphate in a sediment patch of about 1 × 0.5 cm, also indicating simultaneous release of sulphide and Fe(II), as the source of phosphate release was most likely Fe(III) oxides [47]. These data contradict the generally accepted electron donor layering [230] and challenge established biogeochemical models, documenting a much more complex distribution of biogeochemical processes in natural sediments than suggested by conceptual theoretical considerations. In another study, simultaneous measurements of PO_4^{3-}, Fe^{2+} (Fig. 8a and b) and S^{2-} revealed numerous PO_4^{3-} hotspots, presumably induced by mineralisation of organic matter, but also through SO_4^{2-} and Mn (IV) reduction [36]. The distribution of such PO_4^{3-} hotspots may be highly variable, for example it has been shown that the bioturbation activity of tubificid worms considerably decreased the number of PO_4^{3-} hotspots compared to a situation without worms in a lacustrine sediment [46]. These studies demonstrate, that sites of intensified mineralisation can serve as source of phosphorus for intensified biomass production in P limited environments.

5.1.2. Microbial microniches in sediments

A number of studies have used 2D DET and DGT techniques for the investigation of microbial niches in sediments. DET measurements on the distribution of Fe and Mn concentrations in seasonally anoxic lake sediments showed the small-scale variability of Fe and Mn not only across the SWI, but showed also highly heterogeneous concentrations down to a depth of ~6 cm into the sediment [14]. This heterogeneity was interpreted as an indication for the existence of microbial niches in sediments and suggested that such hotspots were important for the reductive dissolution of Fe- and Mn-oxyhydroxides. Using AgI gels and computer imaging densitometry, Devries and Wang [62] showed the first

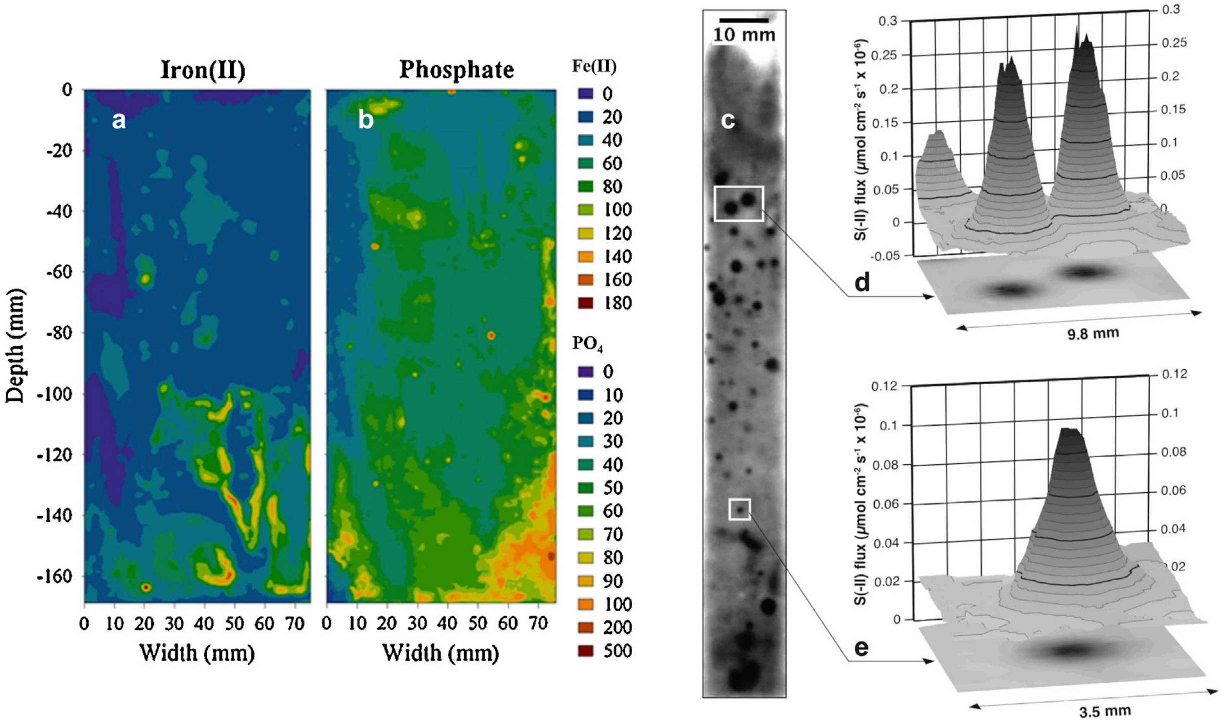

Fig. 8. Simultaneous colorimetric DET images of (a) Fe(II) and (b) phosphate distributions in a *Zostera capricorni* sea grass bed sediment. The calibration bars are given in μmol L^{-1}. Circular, mm-sized hotspots of both, Fe(II) and phosphate are visible, and are interpreted as hotspots of microbial activity. In addition, a faunal burrow structure is indicated to the left as an area of decreased Fe(II) and phosphate concentrations, which might be caused by increased O_2 levels in the burrow lumen due to bioirrigation, leading to increased Fe(III) precipitation and phosphate adsorption to newly formed Fe-oxyhydroxides. Reprinted from Pagès et al. [36], with permission from Elsevier. Copyright 2011 Elsevier. (c) DGT-CID image of sulphide-producing microniches in sediment of a eutrophic lake showing the high abundance of sulphidic microniches. (d and e) 3D plots of details of (c) demonstrating the steep sulphide gradient from the interior of the microniches. Reprinted with permission from Widerlund and Davison [64]. Copyright 2007, American Chemical Society. (For better readability of the colours in this figure the reader is referred to the web version of this article.)

high-resolution image of sulphidic microniches in sediments, probably induced by local carbon enrichment and by a localised high abundance of sulphate reducers. Along with larger, patchy areas of relatively low sulphide concentrations directly below the SWI, which were attributed to sulphide oxidation induced by the O_2 release of roots, this study demonstrated the complex pattern of oxic and sulphidic environments in natural sediments. In an extensive study, Widerlund and Davison [64] applied >130 AgI probes in undisturbed sediment cores as well as in cores that were thoroughly mixed, both after transfer into the laboratory at a temperature of $20 \pm 2\,^{\circ}C$. The authors found more than 3000 sulphidic michroniches with an average density of $\sim$0.3 and $\sim$1.75 niches cm^{-2} gel in January and March/April, respectively (Fig. 8c–e). This seasonal difference was attributed to increased availability of fresh organic matter in March/April compared to January. Niche sizes up to $\sim$10 mm^2 were observed, with 30% of the niches being smaller than 1 mm^2. Moreover, significant shifts in the isotopic composition of sulphide in microniches ($\delta^{34}S$ up to +20‰) compared to non-niche sediment areas were measured using LA-MC-ICPMS [65]. These results showed that bacterial sulphide production is largely confined to discrete microniches that are important in controlling the oxidation of organic matter in sediments and which therefore are important drivers of early diagenesis.

In addition to sulphide, Fe and Mn, trace metals (Cu, Ni, Co, Zn) have been shown to be released from confined hotspots of intensified microbial activity. For instance, intensified Co, Cu, Fe, Ni and Mn mobilisation was observed to be associated to a sulphide-releasing microniche in a lacustrine sediment [63]. Increased metal concentrations were confined to the area of the niche, indicating fast formation of metal sulphides at the edge of this microbial hotspot, thereby re-immobilising the metals. The co-mobilisation of Fe^{2+} and S^{2-} indicated the co-existence of Fe(III) and sulphate reducers [63].

Stockdale et al. [56] showed the removal of phosphate, arsenate and vanadate at a microbial microniche using a AgI-ferrihydrite DGT gel. They reasoned that the decreased phosphate concentration was caused by bacterial uptake. In contrast to this result other studies showed the release of phosphate from microbial microniches, which was interpreted as phosphate release due to the decomposition of organic matter [36,48] or through dissolution of Fe-phosphates [47]. The decrease in dissolved $VO_4{}^{3-}$ and $AsO_4{}^{3-}$ was ascribed to several potential processes including bacterial assimilation, bacterial respiration or to have a link to sulphide reduction [56]. These studies demonstrate that several differential pathways control the dynamics of oxyanions in the vicinity of microbial microniches in sediments.

5.1.3. Terrestrial rhizospheres

Recently, 2D DGT imaging was also applied for the investigation of solute distributions in the rhizosphere of terrestrial plants, especially for the investigating of phosphate (Fig. 9a and b). Santner et al. [12] compared the patterns of soluble phosphate around the roots of two *Brassica napus* cultivars. The cultivar with the higher phosphate acquisition efficiency was able to deplete the soil porewater down to lower phosphate concentrations, confirming its potential for more efficient phosphate uptake. Moreover, hotspots of highly increased P levels were located directly at root tips [12]. These previously unknown hotspots could either be induced by localised P release from the plant root or by release from the soil. Release from the soil could be triggered by highly localised soil acidification due to root proton exudation or due to the exudation of phosphate-solubilising carboxylate anions like citrate. In either case, the localised high P concentrations could serve as growth stimulation of rhizosphere microbes and thereby help the plant root to establish a beneficial microbial community in its vicinity.

In a recent DGT-planar optode sandwich sensor study, Williams et al. [59] showed that during the formation of iron plaque on submerged rice roots, which was induced by radial oxygen release, elevated levels of Fe(II), Pb and As exist at the boundary of the aerobic rhizosphere area. Co-localised pH decreases pointed towards Fe(II) mobilisation being either caused by slowed Fe(II) oxidation, which is very pH-sensitive, or by pH-mediated desorption of Fe(II) from freshly formed iron plaque. The release of Pb was attributed to a larger reservoir of more strongly bound Pb compared to Co, Cu, Ni and Zn, which were depleted in the vicinity of the roots, while the release of As was hypothesized to concur with the release of Fe(II), as As can sorb to negatively charged surfaces *via* Fe(II)-bridges. These findings have important implications for the mobility and accumulation of As in rice plants.

The potential for localised solubilisation of Cd and Zn in the rhizosphere of the metal accumulator *Salix smithiana* in a metal-contaminated soil upon the addition of elemental sulphur was recently investigated using DGT and planar optode imaging [50]. Locally enhanced S^0 oxidation caused rhizosphere acidification and a local drop in the redox potential, leading to Cd and Zn desorption as well as to their co-dissolution with Mn-oxides. As a result, plant metal uptake was highly increased in S^0 treated soils. This emphasizes the potential of enhancing metal uptake by accumulator plants by S^0 addition while reducing the risk of metal leaching to the groundwater.

5.2. Planar optodes

5.2.1. Marine sediments

Planar optodes were first introduced as a tool for investigating O_2 dynamics in surface sediments at high spatio-temporal resolution [17]. Later studies focused on O_2 dynamics in microbial biofilms, photosynthetic microbial mats and highly dynamic sediments [109,112,176]. All of these studies demonstrated highly heterogeneous systems with intense spatial and temporal variability in O_2 production and consumption which had important consequences for the overall biogeochemical functioning of these benthic systems – a fact that had largely been ignored at that point.

Planar O_2 optodes have also provided considerable new insight on the functioning of permeable sediments that are characterised by advective porewater transport [99,118,224,231,232]. These studies predominantly investigated how the advective flow in the sediment affects the O_2 distribution, with particular focus on migrating sand ripples. One excellent example was provided by Precht et al. [99], who demonstrated how oxygenated water is introduced into the ripple troughs and how anoxic pore water is drawn to the surface beneath the ripple crests (Fig. 10a). Migrating sand ripples were trailed by a porewater flow alternately exposing sediment volumes to oxic and anoxic pore water, a dynamic that must regulate the distribution and the coupling of nitrification and denitrification and thereby the overall nitrogen regeneration in such sediment types (Fig. 10d and e). Another study documented how the degradation of buried macroalgae in sandy sediment induced localised anoxic plumes that were advected through the interstitium. This could again have important implications for the turn-over of biologically available nitrogen in such systems (Fig. 10b and c) [231,233]. A combination of planar O_2 optodes and porewater sampling using DET with subsequent stable N isotope analysis showed that stationary, in contrast to migrating ripples, do not stimulate coupled nitrification–denitrification as the stationary oxic and anoxic volumes have little interaction given the characteristic flow lines around such structures [118].

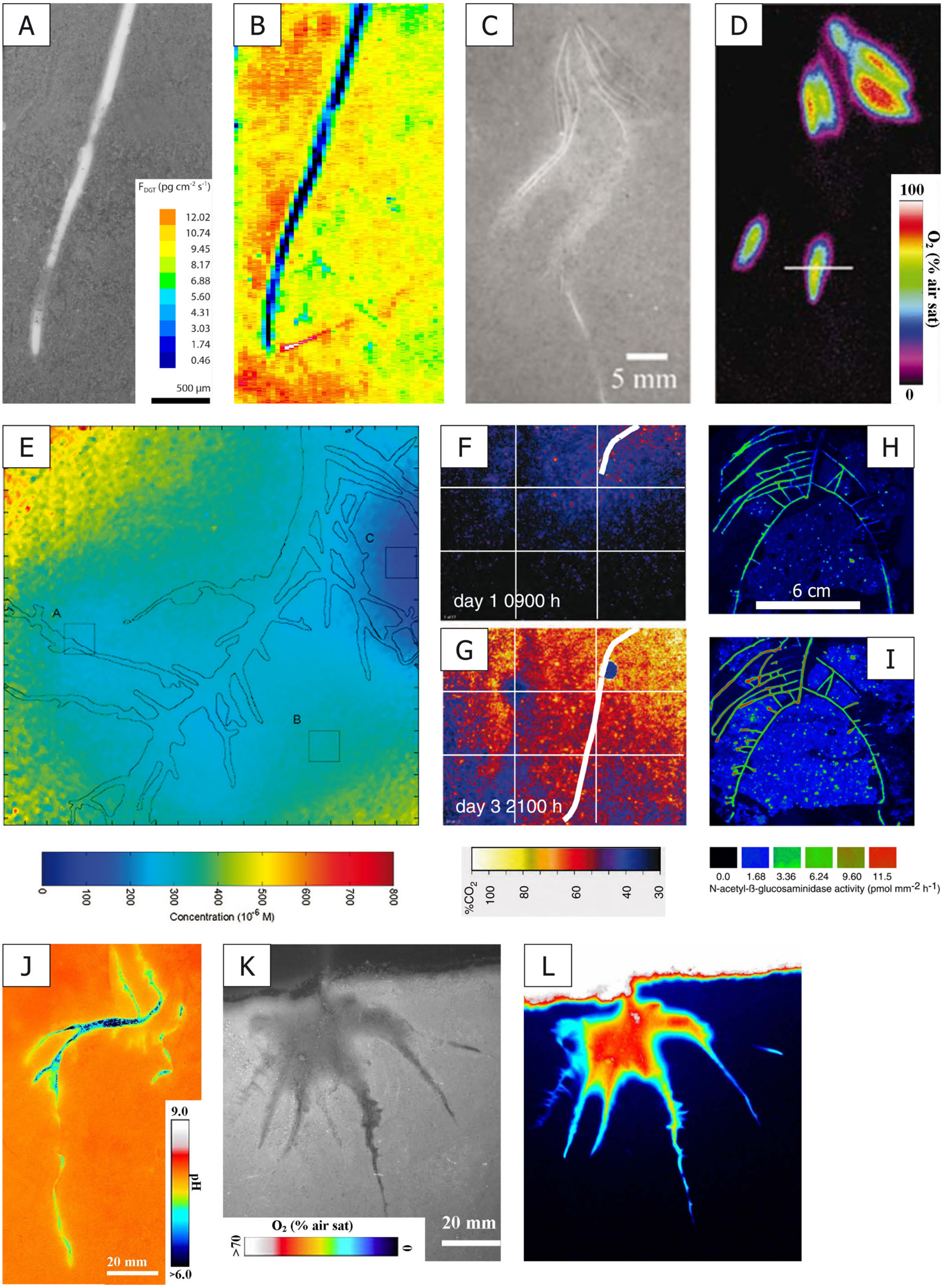

Fig. 9. Chemical changes induced by the rhizophere activity of aquatic and terrestrial plants. (a) Photograph of a maize (*Zea mays*) root grown in a high-P soil and (b) the associated distribution of phosphate around this root, measured using DGT-LA-ICPMS. A narrow phosphate depletion zone around the root due to assimilation is apparent. Andreas Kreuzeder and Jakob Santner, unpublished results. (c) Photograph of a common eelgrass (*Zostera marina*) root system growing in marine sediment and (d) the corresponding O_2 distribution measured by planar optodes. The oxic zones surrounding the tips protect the root tissues from toxic, reduced chemical species such as H_2S and Fe^{2+}. Reproduced with permission from Frederiksen and Glud [225]. Copyright 2014 by the Association for the Sciences of Limnology and Oceanography, Inc. (e) Planar optode image of the NH_4^+ distribution around a tomato (*Solanum lycopersicum*) root. The position of roots is shown by the fine, black lines. Depletion of NH_4^+ in the root zone indicates

As mentioned, a few studies have applied planar optodes to image solute dynamics directly in natural sediments by fixing the sensor foil to a specially designed inverted periscope that could be inserted directly into the sediment (Fig. 1e). The solutes investigated by this apparatus include O_2, pH and pCO_2 distributions in different benthic substrates [86,87,106,201,224]. These studies have, besides confirming that processes investigated in the laboratory could be re-found *in situ*, provide new insights into porewater dynamics in a range of different settings, especially in relation to how diurnal patterns of faunal behaviour affect solute distributions in surface sediments and how meiofauna migrate in relation to the dynamics of oxic-anoxic interphases and to patchy distribution of organic material. However, even though such studies are performed *in situ*, data interpretation has to acknowledge the fact that measurements are performed along a wall and that periscope insertion can disturb the sediment surface and the natural flow regimes as well as induce particle smearing along the front plate (Fig. 2), [201,224,234].

Although the majority of planar optode studies are investigating soils, wetlands and sediments, a few applications in other scientific disciplines exist, like the investigation of O_2 dynamic associated with corals and coral algae [117,161,235]. These studies documented a highly dynamic O_2 regime associated with the O_2 production from corals and coral algae.

Another interesting example is a study on O_2 dynamics in sea ice [111], demonstrating the development of very dynamic and heterogeneous O_2 distribution inside melting sea ice which apparently regulated the extent of nitrate (and ammonia) removal from the ice and its release to the surface waters [111,236].

5.2.2. Macrofauna

Planar optodes are an excellent tool for studying solute dynamics associated to macrofauna behaviour. Therefore most published planar optode studies investigate the effects of burrowing macrofauna and bioirrigation on solute distributions.

The majority of studies have focused on the O_2 dynamics associated to changes in irrigation patterns, excavation and burrowing activities [80,82,87,113,160,163,237,238]. All of these studies demonstrate how irrigation by fauna causes intensified oxygenation of the sediment and as a result significantly increases sediment O_2 uptake (Fig. 11d and e). The *in situ* study by Wenzhöfer and Glud [87] demonstrated that the irrigation and excavation activity of the polychaete *Hediste diversicolor* exhibited a distinct diurnal rhythm which greatly affected the O_2 exchange rate and its availability in deep sediment layers. Using planar O_2 optodes it has also been demonstrated how the buried lesser sandeel (*Ammodytes tobianus*) induces advective O_2 transport in permeable sediments, creating an inverted cone of O_2 rich porewater in front of the mouth (Fig. 11f and g), [108], in order to fulfil its respiratory O_2 demand when buried in the sediment. This study also documented that the fish could not only avoid predators during burial but it also reduced its metabolic costs as compared to periods were it was free swimming.

A few studies have investigated the effects of faunal activity on the distribution of pH/pCO_2 in marine sediments (Fig. 11a–c), directly documenting that faunal irrigation and burrows have a considerable effect on the sediment porewater composition [72,75,83,124]. A study by Zhu et al. [123] demonstrated that the activity of polychaetae caused complex heterogeneity in the porewater pH distribution with gradients of ±2 pH units over a few millimetres. This was induced by active irrigation but also by infilled relict burrows and decaying biomass. Similar heterogeneity was observed in the pCO_2 concentrations in sediment inhabited by the polychaete *Nereis succinea* [20,72]. These studies showed decreased pCO_2 concentrations inside irrigated burrows as compared to surrounding porewater levels, but also documented elevated pCO_2 concentrations in abandoned burrows, which is evidence for elevated microbial respiration in these carbon-enriched micro habitats [72].

Macrofauna activity in terrestrial system is far less studied than in marine sediments. To date only one optode study on the earthworm *Lumbricus terrestris* has been presented [213]. Here it was shown that earthworm mucus deposits along the burrow walls created large (cm^2 size) anoxic microniches that persisted for several days in the otherwise oxygenated soil (Fig. 11h and i). Such anoxic microniches potentially support overlooked anaerobic microbial processes such as denitrification in otherwise well aerated soil.

5.2.3. Rhizosphere

Several studies applied planar optodes to investigate mainly pH, but also O_2/pCO_2 distributions in the rhizosphere of terrestrial and wetland plants [19,104,127,162,239]. These studies observed spatial, temporal (hours to days) and inter-specific variations of the rhizosphere pH distribution. Blossfeld et al. [162] showed that ryegrass and pennycress alkalinized their rhizosphere by up to 1.7 pH units, whereas maize acidified its rhizosphere by up to −0.7 pH units. Based on these pH changes the authors calculated the local soil-solution cadmium concentrations and concluded that the porewater Cd concentrations in the rhizospheres of ryegrass and pennycress were reduced 200-fold, but increased 3-fold in the maize rhizosphere.

The application of pCO_2 optodes showed a considerable increase of the pCO_2 concentration in the vicinity of a root of *Viminaria juncea* growing in submerged soil [104]. This effect was a result of root respiration and local enhancement of microbial activity. Schreiber et al. [240] investigated the flooding tolerance of *Arundinella anomala* and *Alternanthera philoxeroides* using pH and O_2 optodes, showing that the root systems remained fully functional during and after flooding. Blossfeld et al. [32] studied the dynamics of pH and O_2 in the rhizosphere of three *Juncus* species, all of which showed O_2 leakage along the roots but exhibited differential effects on rhizosphere pH. Two species showed either acidification or alkalization, respectively, while the third plant had no impact on the pH levels in the rhizosphere.

Faget et al. [169] presented a combination of pH planar optodes with root identification by fluorescent imaging of green fluorescent protein (GFP) expriming roots. This GFP technique allowed for root identification in situations where roots of two species grew closely together, showing that rhizosphere pH effects were

the assimilation by the roots. Reproduced with permission from Strömberg [227]. Copyright 2008 American Chemical Society. (f and g) CO_2 distribution around a short *Viminaria juncea* root section (f) and after 2.5 days of root growth (g). As the root elongates the CO_2 concentration in the imaged soil area increases as a consequence of root respiration. The root position is indicated as white line in the images. Reprinted with permission from Blossfeld et al. [104] by permission of Oxford University Press. (h and i) Chemical images of the *N*-acetyl-β-glucosaminidase (chitinase) activity around the roots of a *Lupinus polyphyllus* plant immediately (h) and 10 days (i) after cutting the shoot. Root-associated chitinase activity, especially at the tips in (i) is visible. Adapted from Spohn and Kuzyakov [155] with permission from Springer Science and Business Media. (j) Planar optode image of the pH distribution around a maize root growing in a calcaric soil. Rhizosphere alkalinisation was induced by NO_3^- fertilisation. Increased root NO_3^- uptake leads to OH^- release by the root in order to maintain root electroneutrality. Unpublished results of Morten Larsen, Eva Oburger, Jakob Santner, Walter W. Wenzel and Ronnie N. Glud. (k and l) Photographs of a rice (*Oryza sativa*) root system growing in a flooded soil from an image series of an as yet unpublished study [226]. These images are based on dual-image lifetime sensing (Section 3.3.5), and show the root and soil structure as well as the soil–water interface. The dark patches in (k) are the response of the fluorophore to the high O_2 concentrations in the water as well as in the root zone, (l) shows the corresponding, processed O_2 image with intense O_2 release by the roots into the water saturated, anoxic soil. (For better readability of the colours in this figure the reader is referred to the web version of this article.)

Please cite this article in press as: J. Santner, et al., Two decades of chemical imaging of solutes in sediments and soils – a review, Anal. Chim. Acta (2015), http://dx.doi.org/10.1016/j.aca.2015.02.006

stronger when roots of bean and maize grew alone compared to growing in close vicinity to each other. Another study combined O_2 optode imaging with the determination of the water distribution in soil by neutron radiography [164] which enabled to directly link O_2 dynamics to root respiration, plant transpiration, and soil water distribution.

Strömberg [227] investigated the NH_4^+ turnover around roots of tomato (*Solanum lycopersicum*), (Fig. 9f). The planar optode images indicated that NH_4^+ uptake of tomato roots proceeds over the entire root structure and that the uptake of thin peripheral roots was about twice as efficient as that of the main root.

Using their novel soil zymography technique, Spohn and Kuzyakov [154] showed that high acid phosphatase activity is closely associated with roots while the locations with high alkaline phosphatase activities were in areas at greater distance from the roots. This strongly indicated that acid phosphatases are mainly excreted by plant roots and rhizosphere-associated microorganisms, while alkaline phosphatases are mainly produced by microorganisms inhabiting non-rhizosphere soil areas. The spatial differentiation of these microorganisms was interpreted as a strategy to avoid competition for organic P substrates. In a study on dead root biomass turnover, Spohn and Kuzyakov [155] showed the spatial and temporal development of chitinase, phosphatase and cellulase activities in the rhizosphere of *Lupinus polyphyllus* following the cutting of the plant's shoot. This study showed that the stimulation of microbial activity by dying and dead biomass in soil extends to locations up to 55 mm away from the roots (Fig. 9i and j), which is much further than previously reported using soil slicing techniques. Hotspots of enzyme activities were also observed at the root tips directly after cutting the shoot, probably due to the release of rhizodeposits as a consequence of plant injury.

O_2 planar optodes have also been used to investigate the radial oxygen leakage from roots of marine eelgrass (*Zostera marina*), (Fig. 9c and d), [81,225]. While oxygen leakage had previously been anticipated to occur from all root parts, these studies documented that O_2 leakage was confined to the root tips [225]. The high O_2 concentrations at the root tip surface were due to a barrier to O_2 loss in older root parts and the presence of an effective gas-transport system in the plant [81]. The rate of O_2 leakage was regulated by the photosynthetic activity of the plant, the ambient O_2 levels and the root age. Furthermore, it was shown that the oxic microniches were transient and rapidly moved through the sediment as the roots grew by several mm per day. The short-lived nature of these micro-zones presumably limited the potential for coupled denitrification as slow-growing nitrifiers never had time to exploit these dynamic oxic microniches [225].

5.2.4. Greenhouse gas emissions from soil

In the last few years some studies used planar optodes for investigating soil O_2 distribution and the implications of O_2 availability for CO_2 and CH_4 emissions from waterlogged soils [30,31], as well as NH_4^+ dynamics in soil as affected by manure amendments [134,209]. A recent study investigated how different manure amendment approaches affect the O_2 distribution in soil and their effect on the emission rates of greenhouse gasses like N_2O and CO_2, aiming at developing fertilizer placement strategies with minimal greenhouse gas emission rates [100].

6. Future developments

6.1. Method development

One tool for multi-analyte imaging, DGT-optode sandwich sensors, has already been presented in Section 3.4. Other promising multi-parameter imaging applications include

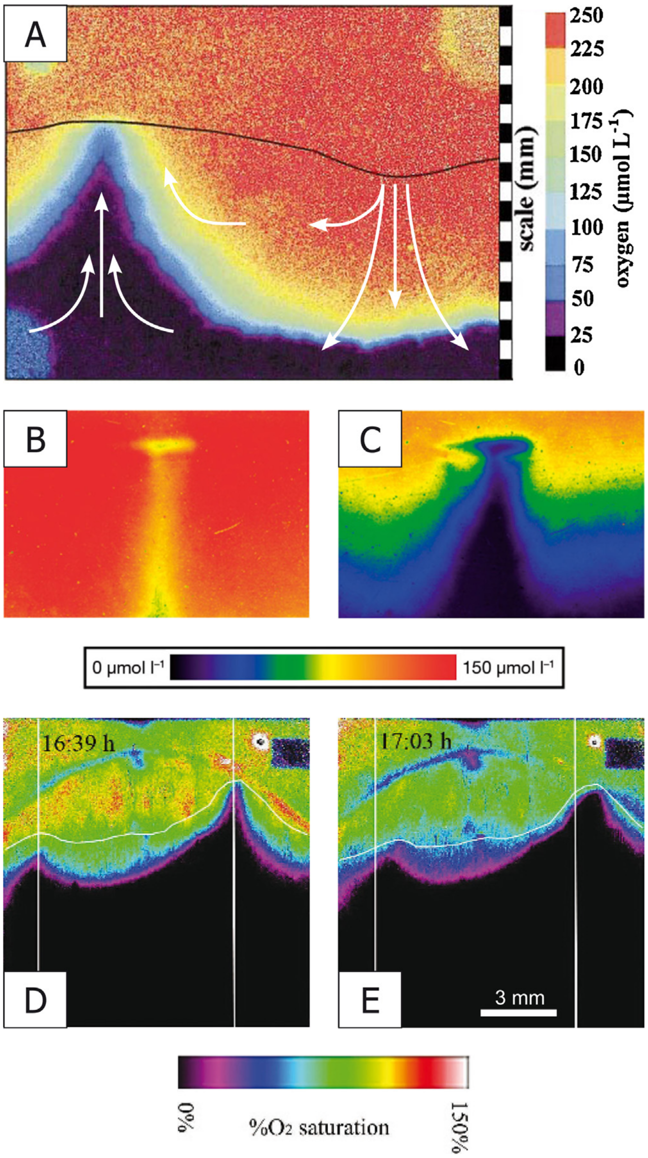

Fig. 10. O_2 dynamics in marine sand ripples. (a) Image of the O_2 distribution in a non-migrating sediment ripple exposed to constant water flow. The black line indicates the sediment surface. The arrows are a schematic representation of the dominating pore water flow in the permeable sediment around the ripple. Upwelling of O_2 depleted porewater from the deeper sediment is apparent in the centre of the ripple, while downwelling occurs at the ripple slope and trough. Some oxic upwelling occur as the two flow paths converge. Adapted with permission from Precht et al. [99]. Copyright 2014 by the Association for the Sciences of Limnology and Oceanography, Inc. (b and c) O_2 distribution around degrading macroalgae (*Ulva lactuca*) in permeable sediments recorded at two different flow velocities (b: 8.2 cm h^{-1} and c: 6.0 cm h^{-1}). The degradation causes oxygen-depleted plumes downstream of the macroalgae in the flow-through reactor. Reprinted from Bourke et al. [233] with permission by Inter-Research Science Center. (d and e) *In situ* planar images of the O_2 distribution around a migrating sand ripple. The two *in situ* images are recorded with a 24 min interval, demonstrating how the migrating ripples affect the O_2 distribution in the underlying sediments. The sediment surface is indicated by the horizontal white line. The two vertical lines indicate the position of the ripple crests on image (d). The areas of O_2 levels >100% in the overlying water were caused by mechanical damage to the sensor foils during emplacement of the inverted periscope. Reproduced with permission from Cook et al. [224]. Copyright 2014 by the Association for the Sciences of Limnology and Oceanography, Inc. (For better readability of the colours in this figure the reader is referred to the web version of this article.)

Please cite this article in press as: J. Santner, et al., Two decades of chemical imaging of solutes in sediments and soils – a review, Anal. Chim. Acta (2015), http://dx.doi.org/10.1016/j.aca.2015.02.006

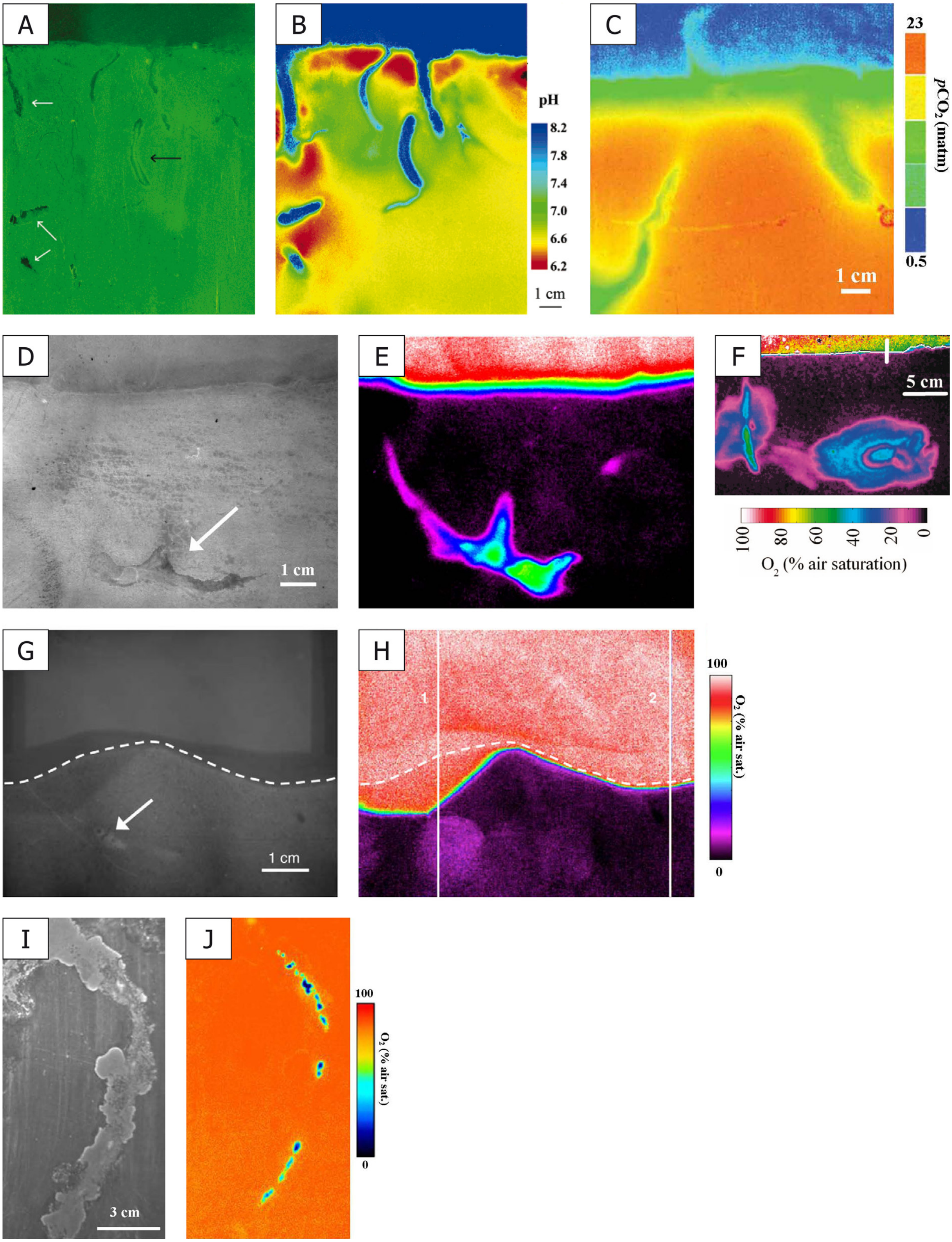

Fig. 11. Chemical images of O_2, pH and pCO_2 in the vicinity of animal burrows. (a) Photograph of common rag worm (*Nereis succinea*) burrows in a marine sediment and (b) the associated pH image. Due to irrigation of overlying water into the burrow lumen the pH is elevated. Other areas in the surface sediments are acidic due to locally intensified mineralization of organic material and potentially re-oxidation processes. Reproduced with permission from Zhu et al. [75]. Copyright 2005 American Chemical Society. (c) pCO_2 distribution in a marine sediment inhabited by a common rag worm (*N. succinea*). The CO_2 concentration in the bulk sediment (orange) is higher than in the overlying water due to decomposition of organic matter. During irrigation the overlying water passing through the burrow lumen gets enriched with CO_2 (vertical green zones). A plume of CO_2-enriched irrigation water released to the overlying waters is visible centrally. Reproduced with permission from Zhu and Aller [20]. Copyright 2014 by the Association for the Sciences of Limnology and Oceanography, Inc. (d) Photograph of a brittle star (*Amphiura filifomis*) specimen buried in marine sediment. The elongated central disk chamber of the animal can be observed. (e) Corresponding planar optode O_2 image. The brittlestar transports O_2-rich water into the cavity within the otherwise anoxic sediment. Morten Larsen and Ronnie N. Glud, unpublished data. (f) O_2 dynamics in permeable sediment around the burrow of a marine lugworm (*Arenicola marina*) specimen. The hydraulic activity of the worm causes substantial oxygenation of the sediment around the burrow – as compared to animals inhabiting cohesive sediments. Reproduced

Please cite this article in press as: J. Santner, et al., Two decades of chemical imaging of solutes in sediments and soils – a review, Anal. Chim. Acta (2015), http://dx.doi.org/10.1016/j.aca.2015.02.006

combinations of pH optodes and root identification through fluorescence-based identification of green fluorescent protein expressing roots [169], as well as pulsed amplitude modulation (PAM) fluorescent imaging and O_2 optodes for investigating the spatial distribution of gross photosynthesis and net O_2 production in benthic microalgae [97]. In the first study using PAM fluorescent and O_2 imaging [97], these parameters were measured on parallel sediment sections, as the emission of the $Ir(Cs)_2(acac)$ O_2 indicator would have interfered with the chlorophyll measurements. However, by selecting an O_2 indicator with emission/excitation wavelengths outside the region of chlorophyll, simultaneous measurements should be possible. Pulsed amplitude modulation imaging using a lifetime based imaging setup has been presented by Grunwald and Kühl [241]. The measuring principle could also be used for the simultaneous imaging of *e.g.* pCO_2 and PAM.

A further, recent adaptation of planar optodes is the use of a camera as a readout device for fiber optic cables [242,243]. Using a single camera, the ends of up to 100 freely positionable fiber optic cables can be read out simultaneously. The system presented by Fischer and Koop-Jakobsen [242] was based on lifetime O_2 measurements, but a ratiometric imaging approach could also be applied for *e.g.* O_2, pH and pCO_2 measurements. The freely positionable fibers make the system ideal to study analyte dynamics over larger scales (meter) at relatively high temporal resolution, *e.g.* O_2 dynamics in soil during flooding and drainage [244] or in permeable sands to study wave-driven pore water exchange of O_2 and pCO_2 [99].

The combined use of solute imaging techniques and localised sampling strategies such as lipid biomarker sampling was shown by Pagès et al. [61]. Shifts in the microbial community structure along a vertical profile through a microbial mat were shown in parallel to laterally and vertically heterogeneous solute distributions.

In addition to multi-parameter imaging, the development of 2D techniques for novel analyte species is ongoing. So far DGT, DET and optode techniques have mainly be used to study simple, inorganic ion species. Recently it was suggested that ionophores and the principle of co-extraction (see Section 3.3.2) could serve as a universal sensing scheme for optodes [133,135], which would considerably increase the number of easy-to-fabricate optode sensors. Hereby it should be possible to measure both, cations and anions, however cation sensing will be easier to achieve, as the plasmonic nanoparticle interactions with the anionic dye is already established [137]. A list of 44 commercially available ionophores is given by the authors [137], with 33 being selective for cations (*e.g.* Ca^{2+}, Fe^{3+}, Na^{+}) and 11 for anions (*e.g.* NO_3^-, NO_2^-, Cl^-). This uncomplicated multi-analyte sensing approach might help to considerably increase the number of sensors available for planar optode imaging.

DGT and DET methods for sampling more complex (organic) solutes, coupled with analytical techniques that have sufficient sensitivity to detect ultra-trace analyte amounts would clearly advance biogeochemical investigations in sediments and soils. The localisation of the exudation of organic molecules from plant roots, which are often released to increase nutrient bioavailability, or potential localised differences in the degradation of organic contaminants in the rhizosphere or in the vicinity of animal burrows remain largely unresolved.

Furthermore, the application of spatially resolved DGT and DET sampling coupled with the determination of stable isotope ratios provides a novel tool to trace biogeochemical reactions, as demonstrated by $^{32}S/^{34}S$ isotope fractionation during sulphate reduction in sulphidic microniches [65,182] and by using $^{15}NO_3$ as tracer in a study on coupled nitrification–denitrification in stationary, permeable sand ripples [39].

6.2. Fields of application

Although solute imaging is already widespread in aquatic science, novel application areas are emerging. While sea ice studies have received much attention in recent years, only one study has applied planar O_2 optodes to sea ice [236]. Future use of pH and pCO_2 sensors might provide valuable insights into the sea ice CO_2-carbonate system, while O_2, temperature and possibly also Cl^- sensors are of high interest for investigating the spatially complex dynamics in sea ice–brine systems. Due to the potential temperature gradients in the ice it will be necessary to map the temperature at high spatial resolution in order to perform accurate temperature compensation of the luminescent signal. This could be solved elegantly by using dual-indicator planar optodes taking advantage of phosphorescent indicators with significantly different luminescent lifetimes [126,216]. The dual lifetime determination method with the same optical configuration can be used for both indicator types. For other dual sensors with only one phosphorescent indicator (*e.g.* pH/temperature, pCO_2/temperature, Cl^-/temperature) the use of different optical filters and excitation wavelengths will be required to separate the signals and reduce optical crosstalk.

In soil science, only a few pioneering studies have used solute imaging so far. Studies on localised contaminant mobilisation in terrestrial rhizospheres [50,59], phosphorus efflux from root tips [12], rhizosphere pH changes [19,32,162] as well as increases in the CO_2 concentration in the vicinity of plant roots [104], represent innovative showcases for the potential of solute imaging in soil. In addition to the rhizosphere, which is clearly a highly heterogeneous environment in soils, solute imaging might also become important in other areas of soil science. Greenhouse gas (GHG) production and release from soils is a rapidly developing research area. As sensors for several analytes of interest (O_2, CO_2, N species and enzyme activities) are available, solute imaging is likely to become an important technique for understanding the spatio-temporal dynamics of GHG-related processes in soils. A pioneering study in this field was presented by Zhu et al. [100], who investigated N_2O emissions from soils in relation to the O_2 distribution in soil after manure application.

This review compiled innovative studies on planar chemical sensing and demonstrated the unique potential for gaining novel insights in complex and, heterogeneous environments by such procedures. The increasing use and development of planar optodes, DET, DGT and other solute imaging techniques, will undoubtedly continue and provide versatile tools for biogeochemical research in complex and dynamics habitats.

---

with permission from Volkenborn et al. [237]. Copyright 2014 by the Association for the Sciences of Limnology and Oceanography, Inc. (g) Photograph of a lesser sandeel (*Ammodytes tobianus*) buried in marine sediment and (h) the associated distribution of O_2. A plume of oxic water in front of the fish mouth, attributed to advective water flow into the sediment was created by the fish and strongly O_2 depleted water leaves the gills and disperses into the otherwise anoxic porewater. Reproduced with permission of the Journal of Experimental Biology from Behrens et al. [108]. (i) Photograph of an earthworm burrow in soil lined with earthworm casts. (j) Corresponding planar optode O_2 image showing highly localised O_2 depletion at the burrow wall, most likely caused by increased microbial activity and reduced solute transport in the mucus lining. Reprinted from Elberling et al. [213] by Permission, ASA, CSSA, SSSA. (For better readability of the colours in this figure the reader is referred to the web version of this article.)

Please cite this article in press as: J. Santner, et al., Two decades of chemical imaging of solutes in sediments and soils – a review, Anal. Chim. Acta (2015), http://dx.doi.org/10.1016/j.aca.2015.02.006

Acknowledgements

The work of JS and AK was funded by the Austrian Science Fund (FWF): P23798-B16. ML & RNG were financially supported by ERC through an Advanced Grant (ERC-2010-AdG20100224), the Danish National Research Foundation (#DNRF53 to Nordic Center for Earth Evolution), the Commission for Scientific Research in Greenland (KVUG; GCRC6507), the Danish Council for Independent Research (12-125843) and the Villum Foundation.

Appendix A. Supplementary data

Supplementary data associated with this article can be found, in the online version, at http://dx.doi.org/10.1016/j.aca.2015.02.006.

References

[1] R.A. Berner, Early Diagenesis: a Theoretical Approach, Princeton University Press, Princeton, NJ, 1980.
[2] R.C. Aller, 8.11 – sedimentary diagenesis, depositional environments, and benthic fluxes, in: H.D. Holland, K.K. Turekian (Eds.), Treatise on Geochemistry, 2nd ed.), Elsevier, Oxford, 2014, pp. 293–334.
[3] G. Kirk, The Biogeochemistry of Submerged Soils, Wiley, Chichester, 2004.
[4] R.N. Glud, Oxygen dynamics of marine sediments, Mar. Biol. Res. 4 (2008) 243–289.
[5] M. Kühl, N.P. Revsbech, Biogeochemical microsensors for boundary layer studies, in: B.P. Boudreau, B.B. Jørgensen (Eds.), The Benthic Boundary Layer, Oxford University Press, 2001.
[6] M. Taillefert, G.W. Luther III, D.B. Nuzzio, The application of electrochemical tools for in situ measurements in aquatic systems, Electroanalysis 12 (2000) 401–412.
[7] B.B. Jørgensen, R.N. Glud, O. Holby, Oxygen distribution and bioirrigation in Arctic fjord sediments (Svalbard, Barents Sea), Mar. Ecol. Prog. Ser. 292 (2005) 85–95.
[8] B.B. Jørgensen, N.P. Revsbech, Y. Cohen, Photosynthesis and structure of benthic microbial mats: microelectrode and SEM studies of four cyanobacterial communities, Limnol. Oceanogr. 28 (1983) 1075–1093.
[9] G. Holst, R.N. Glud, M. Kühl, I. Klimant, A microoptode array for fine-scale measurement of oxygen distribution, Sens. Actuators B: Chem. 38 (1997) 122–129.
[10] R.N. Glud, H. Stahl, P. Berg, F. Wenzhöfer, K. Oguri, H. Kitazato, In situ microscale variation in distribution and consumption of O_2: a case study from a deep ocean margin sediment (Sagami Bay, Japan), Limnol. Oceanogr. 54 (2009) 1–12.
[11] W. Davison, G.R. Fones, G.W. Grime, Dissolved metals in surface sediment and microbial mat at 100-μm resolution, Nature 387 (1997) 885–888.
[12] J. Santner, H. Zhang, D. Leitner, A. Schnepf, T. Prohaska, M. Puschenreiter, W.W. Wenzel, High-resolution chemical imaging of labile phosphorus in the rhizosphere of *Brassica napus* L. cultivars, Environ. Exp. Bot. 77 (2012) 219–226.
[13] P.R. Teasdale, S. Hayward, W. Davison, In situ, high-resolution measurement of dissolved sulfide using diffusive gradients in thin films with computer-imaging densitometry, Anal. Chem. 71 (1999) 2186–2191.
[14] S.M. Shuttleworth, W. Davison, J. Hamilton-Taylor, Two-dimensional and fine structure in the concentrations of iron and manganese in sediment pore-waters, Environ. Sci. Technol. 33 (1999) 4169–4175.
[15] D. Jézéquel, R. Brayner, E. Metzger, E. Viollier, F. Prévot, F. Fiévet, Two-dimensional determination of dissolved iron and sulfur species in marine sediment pore-waters by thin-film based imaging. Thau lagoon (France), Estuarine Coastal Shelf Sci. 72 (2007) 420–431.
[16] D. Robertson, P.R. Teasdale, D.T. Welsh, A novel gel-based technique for the high resolution, two-dimensional determination of iron(II) and sulfide in sediment, Limnol. Oceanogr.: Methods 6 (2008) 502–512.
[17] R.N. Glud, N.B. Ramsing, J.K. Gundersen, I. Klimant, Planar optrodes: a new tool for fine scale measurements of two-dimensional O_2 distribution in benthic communities, Mar. Ecol. Prog. Ser. 140 (1996) 217–226.
[18] S. Hulth, R.C. Aller, P. Engstrom, E. Selander, A pH plate fluorosensor (optode) for early diagenetic studies of marine sediments, Limnol. Oceanogr. 47 (2002) 212–220.
[19] S. Blossfeld, D. Gansert, A novel non-invasive optical method for quantitative visualization of pH dynamics in the rhizosphere of plants, Plant Cell Environ. 30 (2007) 176–186.
[20] Q. Zhu, R.C. Aller, A rapid response, planar fluorosensor for measuring two-dimensional pCO_2 distributions and dynamics in marine sediments, Limnol. Oceanogr.: Methods 8 (2010) 326–336.
[21] Q. Zhu, R.C. Aller, Planar fluorescence sensors for two-dimensional measurements of H_2S distributions and dynamics in sedimentary deposits, Mar. Chem. 157 (2013) 49–58.
[22] H.-P. Blume, G.W. Brümmer, U. Schwertmann, R. Horn, I. Kögel-Knabner, K. Stahr, K. Auerswald, L. Beyer, A. Hartmann, N. Litz, A. Scheinost, H. Stanjek, G. Welp, B.-M. Wilke, Lehrbuch der Bodenkunde, 15 ed., Spektrum Akademischer Verlag, Heidelberg, Berlin, 2002.
[23] E.J. Gabet, O.J. Reichman, E.W. Seabloom, The effects of bioturbation on soil processes and sediment transport, Annu. Rev. Earth Planet. Sci. 31 (2003) 249–273.
[24] P. Hinsinger, G.R. Gobran, P.J. Gregory, W.W. Wenzel, Rhizosphere geometry and heterogeneity arising from root-mediated physical and chemical processes, New Phytol. 168 (2005) 293–303.
[25] J.D. van Elsas, J.K. Jansson, J.T. Trevors, Modern Soil Microbiology, 2nd ed., CRC Press, Boca Raton, 2007.
[26] M.H. Weisenseel, A. Dorn, L.F. Jaffe, Natural H^+ currents traverse growing roots and root hairs of barley (*Hordeum vulgare* L.), Plant Physiol. 64 (1979) 512–518.
[27] B. Jaillard, L. Ruiz, J.C. Arvieu, pH mapping in transparent gel using color indicator videodensitometry, Plant Soil 183 (1996) 85–95.
[28] K.K.S. Bhat, P.H. Nye, Diffusion of phosphate to plant roots in soil – I. Quantitative autoradiography of the depletion zone, Plant Soil 38 (1973) 161–175.
[29] W.W. Wenzel, G. Wieshammer, W.J. Fitz, M. Puschenreiter, Novel rhizobox design to assess rhizosphere characteristics at high spatial resolution, Plant Soil 237 (2001) 37–45.
[30] L. Askaer, B. Elberling, R.N. Glud, M. Kühl, F.R. Lauritsen, H.R. Joensen, Soil heterogeneity effects on O_2 distribution and CH_4 emissions from wetlands: in situ and mesocosm studies with planar O_2 optodes and membrane inlet mass spectrometry, Soil Biol. Biochem. 42 (2010) 2254–2265.
[31] B. Elberling, L. Askaer, C.J. Jorgensen, H.P. Joensen, M. Kühl, R.N. Glud, F.R. Lauritsen, Linking soil O_2, CO_2, and CH_4 concentrations in a wetland soil: implications for CO_2 and CH_4 fluxes, Environ. Sci. Technol. 45 (2011) 3393–3399.
[32] S. Blossfeld, D. Gansert, B. Thiele, A.J. Kuhn, R. Lösch, The dynamics of oxygen concentration, pH value, and organic acids in the rhizosphere of *Juncus* spp, Soil Biol. Biochem. 43 (2011) 1186–1197.
[33] W. Davison, G.W. Grime, J.A.W. Morgan, K. Clarke, Distribution of dissolved iron in sediment pore waters at submillimetre resolution, Nature 352 (1991) 323–325.
[34] W. Davison, H. Zhang, G.W. Grime, Performance characteristics of gel probes used for measuring the chemistry of pore waters, Environ. Sci. Technol. 28 (1994) 1623–1632.
[35] W.W. Bennett, P.R. Teasdale, D.T. Welsh, J.G. Panther, D.F. Jolley, Optimization of colorimetric DET technique for the in situ, two-dimensional measurement of iron(II) distributions in sediment porewaters, Talanta 88 (2012) 490–495.
[36] A. Pagès, P.R. Teasdale, D. Robertson, W.W. Bennett, J. Schäfer, D.T. Welsh, Representative measurement of two-dimensional reactive phosphate distributions and co-distributed iron(II) and sulfide in seagrass sediment porewaters, Chemosphere 85 (2011) 1256–1261.
[37] D. Robertson, D.T. Welsh, P.R. Teasdale, Investigating biogenic heterogeneity in coastal sediments with two-dimensional measurements of iron(II) and sulfide, Environ. Chem. 6 (2009) 60–69.
[38] F. Cesbron, E. Metzger, P. Launeau, B. Deflandre, M.-L. Delgard, A. Thibault de Chanvalon, E. Geslin, P. Anschutz, D. Jézéquel, Simultaneous 2D imaging of dissolved iron and reactive phosphorus in sediment porewaters by thin-film and hyperspectral methods, Environ. Sci. Technol. 48 (2014) 2816–2826.
[39] A.J. Kessler, R.N. Glud, M.B. Cardenas, P.L.M. Cook, Transport zonation limits coupled nitrification-denitrification in permeable sediments, Environ. Sci. Technol. 47 (2013) 13404–13411.
[40] W. Davison, H. Zhang, In situ speciation measurements of trace components in natural waters using thin-film gels, Nature 367 (1994) 546–548.
[41] H. Zhang, W. Davison, Performance characteristics of diffusion gradients in thin films for the in situ measurement of trace metals in aqueous solution, Anal. Chem. 67 (1995) 3391–3400.
[42] F. Degryse, E. Smolders, H. Zhang, W. Davison, Predicting availability of mineral elements to plants with the DGT technique: a review of experimental data and interpretation by modelling, Environ. Chem. 6 (2009) 198–218.
[43] H. Zhang, F.J. Zhao, B. Sun, W. Davison, S.P. McGrath, A new method to measure effective soil solution concentration predicts copper availability to plants, Environ. Sci. Technol. 35 (2001) 2602–2607.
[44] C.D. Luider, J. Crusius, R.C. Playle, P.J. Curtis, Influence of natural organic matter source on copper speciation as demonstrated by Cu binding to fish gills, by ion selective electrode, and by DGT gel sampler, Environ. Sci. Technol. 38 (2004) 2865–2872.
[45] S. Scally, W. Davison, H. Zhang, In situ measurements of dissociation kinetics and labilities of metal complexes in solution using DGT, Environ. Sci. Technol. 37 (2003) 1379–1384.
[46] S. Ding, F. Jia, D. Xu, Q. Sun, L. Zhang, C. Fan, C. Zhang, High-resolution, two-dimensional measurement of dissolved reactive phosphorus in sediments using the diffusive gradients in thin films technique in combination with a routine procedure, Environ. Sci. Technol. 45 (2011) 9680–9686.
[47] S. Ding, Q. Sun, D. Xu, F. Jia, X. He, C. Zhang, High-resolution simultaneous measurements of dissolved reactive phosphorus and dissolved sulfide: the first observation of their simultaneous release in sediments, Environ. Sci. Technol. 46 (2012) 8297–8304.
[48] S. Ding, Y. Wang, D. Xu, C. Zhu, C. Zhang, Gel-based coloration technique for the submillimeter-scale imaging of labile phosphorus in sediments and soils with diffusive gradients in thin films, Environ. Sci. Technol. 47 (2013) 7821–7829.
[49] G.R. Fones, W. Davison, J. Hamilton-Taylor, The fine-scale remobilization of metals in the surface sediment of the North-East Atlantic, Cont. Shelf Res. 24 (2004) 1485–1504.

Please cite this article in press as: J. Santner, et al., Two decades of chemical imaging of solutes in sediments and soils – a review, Anal. Chim. Acta (2015), http://dx.doi.org/10.1016/j.aca.2015.02.006

[50] C. Hoefer, J. Santner, M. Puschenreiter, W.W. Wenzel, Localized metal solubilisation in the rhizosphere of *Salix smithiana* upon sulfur application, Environ. Sci. Technol. (2015) (under review).
[51] A. Kreuzeder, J. Santner, T. Prohaska, W.W. Wenzel, Gel for simultaneous chemical imaging of anionic and cationic solutes using diffusive gradients in thin films, Anal. Chem. 85 (2013) 12028–12036.
[52] N.J. Lehto, W. Davison, H. Zhang, The use of ultra-thin diffusive gradients in thin-films (DGT) devices for the analysis of trace metal dynamics in soils and sediments: a measurement and modelling approach, Environ. Chem. 9 (2012) 415–423.
[53] A. Pagès, D.T. Welsh, D. Robertson, J.G. Panther, J. Schäfer, R.B. Tomlinson, P.R. Teasdale, Diurnal shifts in co-distributions of sulfide and iron(II) and profiles of phosphate and ammonium in the rhizosphere of *Zostera capricorni*, Estuarine Coastal Shelf Sci. 115 (2012) 282–290.
[54] J. Santner, T. Prohaska, J. Luo, H. Zhang, Ferrihydrite containing gel for chemical imaging of labile phosphate species in sediments and soils using diffusive gradients in thin films, Anal. Chem. 82 (2010) 7668–7674.
[55] H. Stahl, K.W. Warnken, L. Sochaczewski, R.N. Glud, W. Davison, H. Zhang, A combined sensor for simultaneous high resolution 2-D imaging of oxygen and trace metals fluxes, Limnol. Oceanogr.: Methods 10 (2012) 389–401.
[56] A. Stockdale, W. Davison, H. Zhang, High-resolution two-dimensional quantitative analysis of phosphorus, vanadium and arsenic, and qualitative analysis of sulfide in a freshwater sediment, Environ. Chem. 5 (2008) 143–149.
[57] A. Stockdale, W. Davison, H. Zhang, 2D simultaneous measurement of the oxyanions of P, V As, Mo, Sb, W and U, J. Environ. Monit. 12 (2010) 981–984.
[58] K.W. Warnken, H. Zhang, W. Davison, Analysis of polyacrylamide gels for trace metals using diffusive gradients in thin films and laser ablation inductively coupled plasma mass spectrometry, Anal. Chem. 76 (2004) 6077–6084.
[59] P.N. Williams, J. Santner, M. Larsen, N.J. Lehto, E. Oburger, W.W. Wenzel, R.N. Glud, W. Davison, H. Zhang, Localized flux maxima of arsenic, lead, and iron around root apices in flooded lowland rice, Environ. Sci. Technol. 48 (2014) 8498–8506.
[60] H. Zhang, W. Davison, Diffusional characteristics of hydrogels used in DGT and DET techniques, Anal. Chim. Acta 398 (1999) 329–340 (in press).
[61] A. Pagès, K. Grice, M. Vacher, D.T. Welsh, P.R. Teasdale, W.W. Bennett, P. Greenwood, Characterizing microbial communities and processes in a modern stromatolite (Shark Bay) using lipid biomarkers and two-dimensional distributions of porewater solutes, Environ. Microbiol. (2014) (in press).
[62] C.R. Devries, F. Wang, In situ two-dimensional high-resolution profiling of sulfide in sediment interstitial waters, Environ. Sci. Technol. 37 (2003) 792–797.
[63] M. Motelica-Heino, C. Naylor, H. Zhang, W. Davison, Simultaneous release of metals and sulfide in lacustrine sediment, Environ. Sci. Technol. 37 (2003) 4374–4381.
[64] A. Widerlund, W. Davison, Size and density distribution of sulfide-producing microniches in lake sediments, Environ. Sci. Technol. 41 (2007) 8044–8049.
[65] A. Widerlund, G.M. Nowell, W. Davison, D.G. Pearson, High-resolution measurements of sulphur isotope variations in sediment pore-waters by laser ablation multicollector inductively coupled plasma mass spectrometry, Chem. Geol. 291 (2012) 278–285.
[66] I. Klimant, V. Meyer, M. Kühl, Fiber-optic oxygen microsensors, a new tool in aquatic biology, Limnol. Oceanogr. 40 (1995) 1159–1165.
[67] I. Klimant, M. Kühl, R.N. Glud, G. Holst, Optical measurement of oxygen and temperature in microscale: strategies and biological applications, Sens. Actuators B: Chem. 38 (1997) 29–37.
[68] M. Quaranta, S. Borisov, I. Klimant, Indicators for optical oxygen sensors, Bioanal. Rev. 4 (2012) 115–157.
[69] X. Cai, J.E. Martin, L.E. Shea-Rohwer, K. Gong, D.F. Kelley, Thermal quenching mechanisms in II–VI semiconductor nanocrystals, J. Phys. Chem. C 117 (2013) 7902–7913.
[70] S.M. Borisov, I. Klimant, Ultrabright oxygen optodes based on cyclometalated iridium(III) coumarin complexes, Anal. Chem. 79 (2007) 7501–7509.
[71] M. Staal, E.I. Prest, J.S. Vrouwenvelder, L.F. Rickelt, M. Kühl, A simple optode based method for imaging O_2 distribution and dynamics in tap water biofilms, Water Res. 45 (2011) 5027–5037.
[72] Q.Z. Zhu, R.C. Aller, Y.Z. Fan, A new ratiometric planar fluorosensor for measuring high resolution, two-dimensional pCO_2 distributions in marine sediments, Mar. Chem. 101 (2006) 40–53.
[73] A. Hakonen, S. Hulth, A high-performance fluorosensor for pH measurements between 6 and 9, Talanta 80 (2010) 1964–1969.
[74] N. Strömberg, S. Hulth, Assessing an imaging ammonium sensor using time correlated pixel-by-pixel calibration, Anal. Chim. Acta 550 (2005) 61–68.
[75] Q.Z. Zhu, R.C. Aller, Y.Z. Fan, High-performance planar pH fluorosensor for two-dimensional pH measurements in marine sediment and water, Environ. Sci. Technol. 39 (2005) 8906–8911.
[76] K. Waich, T. Mayr, I. Klimant, Fluorescence sensors for trace monitoring of dissolved ammonia, Talanta 77 (2008) 66–72.
[77] Z. Cao, Q. Zhu, R.C. Aller, J.Y. Aller, A fluorosensor for two-dimensional measurements of extracellular enzyme activity in marine sediments, Mar. Chem. 123 (2011) 23–31.
[78] Q. Zhu, R.C. Aller, Two-dimensional dissolved ferrous iron distributions in marine sediments as revealed by a novel planar optical sensor, Mar. Chem. 136–137 (2012) 14–23.
[79] S.M. Borisov, T. Mayr, I. Klimant, Poly(styrene-block-vinylpyrrolidone) beads as a versatile material for simple fabrication of optical nanosensors, Anal. Chem. 80 (2008) 573–582.
[80] L. Polerecky, N. Volkenborn, P. Stief, High temporal resolution oxygen imaging in bioirrigated sediments, Environ. Sci. Technol. 40 (2006) 5763–5769.
[81] S.I. Jensen, M. Kühl, R.N. Glud, L.B. Jorgensen, A. Prieme, Oxic microzones and radial oxygen loss from roots of *Zostera marina*, Mar. Ecol. Prog. Ser. 293 (2005) 49–58.
[82] M. Larsen, S.M. Borisov, B. Grunwald, I. Klimant, R.N. Glud, A simple and inexpensive high resolution color ratiometric planar optode imaging approach: application to oxygen and pH sensing, Limnol. Oceanogr.: Methods 9 (2011) 348–360.
[83] A. Hakonen, S. Hulth, S. Dufour, Analytical performance during ratiometric long-term imaging of pH in bioturbated sediments, Talanta 81 (2010) 1393–1401.
[84] D.A. Minett, P.L.M. Cook, A.J. Kessler, T.R. Cavagnaro, Root effects on the spatial and temporal dynamics of oxygen in sand-based laboratory-scale constructed biofilters, Ecol. Eng. 58 (2013) 414–422.
[85] J.P. Fischer, F. Wenzhöfer, A novel planar optode setup for concurrent oxygen and light field imaging: application to a benthic phototrophic community, Limnol. Oceanogr.: Methods 8 (2010) 254–268.
[86] R.N. Glud, F. Wenzhöfer, A. Tengberg, M. Middelboe, K. Oguri, H. Kitazato, Distribution of oxygen in surface sediments from central Sagami Bay, Japan: in situ measurements by microelectrodes and planar optodes, Deep-Sea Res. Part I-Oceanogr. Res. Pap. 52 (2005) 1974–1987.
[87] F. Wenzhöfer, R.N. Glud, Small-scale spatial and temporal variability in coastal benthic O_2 dynamics: effects of fauna activity, Limnol. Oceanogr. 49 (2004) 1471–1481.
[88] H. Zhang, W. Davison, R. Gadi, T. Kobayashi, In situ measurement of dissolved phosphorus in natural waters using DGT, Anal. Chim. Acta 370 (1998) 29–38.
[89] K.W. Warnken, H. Zhang, W. Davison, Performance characteristics of suspended particulate reagent- iminodiacetate as a binding agent for diffusive gradients in thin films, Anal. Chim. Acta 508 (2004) 41–51.
[90] BIO-RAD Chelex® 100 and Chelex 20 Chelating Ion Exchange Resin – Instruction Manual, BIO-RAD Laboratories. http://www3.bio-rad.com/webmaster/pdfs/9184_Chelex.PDF, 1998 (accessed 14.11.13.).
[91] J. Luo, H. Zhang, J. Santner, W. Davison, Performance characteristics of diffusive gradients in thin films equipped with a binding gel layer containing precipitated ferrihydrite for measuring arsenic(V), Selenium(VI), Vanadium (V), and Antimony(V), Anal. Chem. 82 (2010) 8903–8909.
[92] S. Ding, D. Xu, Q. Sun, H. Yin, C. Zhang, Measurement of dissolved reactive phosphorus using the diffusive gradients in thin films technique with a high-capacity binding phase, Environ. Sci. Technol. 44 (2010) 8169–8174.
[93] Q. Sun, J. Chen, H. Zhang, S. Ding, Z. Li, P.N. Williams, H. Cheng, C. Han, L. Wu, C. Zhang, Improved diffusive gradients in thin films (DGT) measurement of total dissolved inorganic arsenic in waters and soils using a hydrous zirconium oxide binding layer, Anal. Chem. 86 (2014) 3060–3067.
[94] G. Odian, Principles of Polymerisation, John Wiley and Sons, Inc., Hoboken, NJ, 2004.
[95] S. Draxler, M.E. Lippitsch, I. Klimant, H. Kraus, O.S. Wolfbeis, Effects of polymer matrixes on the time-resolved luminescence of a ruthenium complex quenched by oxygen, J. Phys. Chem. 99 (1995) 3162–3167.
[96] K. Koren, L. Hutter, B. Enko, A. Pein, S.M. Borisov, I. Klimant, Tuning the dynamic range and sensitivity of optical oxygen-sensors by employing differently substituted polystyrene-derivatives, Sens. Actuators B: Chem. 176 (2013) 344–350.
[97] K. Hancke, B. Sorell, L.C. Lund-Hansen, M. Larsen, T. Hancke, R.N. Glud, Effects of temperature and irradiance on a benthic microalgae community: a combined two-dimensional oxygen and fluorescence imaging approach, Limnol. Oceanogr. 59 (2014) 1599–1611.
[98] M. Kühl, L.F. Rickelt, R. Thar, Combined imaging of bacteria and oxygen in biofilms, Appl. Environ. Microbiol. 73 (2007) 6289–6295.
[99] E. Precht, U. Franke, L. Polerecky, M. Huettel, Oxygen dynamics in permeable sediments with wave-driven pore water exchange, Limnol. Oceanogr. 49 (2004) 693–705.
[100] K. Zhu, S. Bruun, M. Larsen, R.N. Glud, L.S. Jensen, Spatial oxygen distribution and nitrous oxide emissions from soil after manure application: a novel approach using planar optodes, J. Environ. Qual. 43 (2014) 1809–1812.
[101] T. Mayr, T. Abel, B. Enko, S. Borisov, C. Konrad, S. Köstler, B. Lamprecht, S. Sax, E.J.W. List, I. Klimant, A planar waveguide optical sensor employing simple light coupling, Analyst 134 (2009) 1544–1547.
[102] T. Mayr, S.M. Borisov, T. Abel, B. Enko, K. Waich, G. Mistlberger, I. Klimant, Light harvesting as a simple and versatile way to enhance brightness of luminescent sensors, Anal. Chem. 81 (2009) 6541–6545.
[103] Z. Zhou, R. Shinar, A.J. Allison, J. Shinar, Enhanced photoluminescence of oxygen sensing films through doping with high dielectric constant particles, Adv. Funct. Mater. 17 (2007) 3530–3537.
[104] S. Blossfeld, C.M. Schreiber, G. Liebsch, A.J. Kuhn, P. Hinsinger, Quantitative imaging of rhizosphere pH and CO_2 dynamics with planar optodes, Ann. Bot. 112 (2013) 267–276.
[105] M. Kühl, L. Polerecky, Functional and structural imaging of phototrophic microbial communities and symbioses, Aquat. Microb. Ecol. 53 (2008) 99–118.

[106] Y. Fan, Q. Zhu, R.C. Aller, D.C. Rhoads, An in situ multispectral imaging system for planar optodes in sediments: examples of high-resolution seasonal patterns of pH, Aquat. Geochem. 17 (2011) 457–471.

[107] M.R. Chatni, D.E. Maier, D.M. Porterfield, Evaluation of microparticle materials for enhancing the performance of fluorescence lifetime based optrodes, Sens. Actuators B: Chem. 141 (2009) 471–477.

[108] J.W. Behrens, H.J. Stahl, J.F. Steffensen, R.N. Glud, Oxygen dynamics around buried lesser sandeels Ammodytes tobianus (Linnaeus 1785): mode of ventilation and oxygen requirements, J. Exp. Biol. 210 (2007) 1006–1014.

[109] R.N. Glud, M. Kühl, O. Kohls, N.B. Ramsing, Heterogeneity of oxygen production and consumption in a photosynthetic microbial mat as studied by planar optodes, J. Phycol. 35 (1999) 270–279.

[110] B. König, O. Kohls, G. Holst, R.N. Glud, M. Kühl, Fabrication and test of sol–gel based planar oxygen optodes for use in aquatic sediments, Mar. Chem. 97 (2005) 262–276.

[111] S. Rysgaard, R.N. Glud, M.K. Sejr, M.E. Blicher, H.J. Stahl, Denitrification activity and oxygen dynamics in Arctic sea ice, Polar Biol. 31 (2008) 527–537.

[112] R.N. Glud, C.M. Santegoeds, D. De Beer, O. Kohls, N.B. Ramsing, Oxygen dynamics at the base of a biofilm studied with planar optodes, Aquat. Microb. Ecol. 14 (1998) 223–233.

[113] K. Timmermann, G.T. Banta, R.N. Glud, Linking *Arenicola marina* irrigation behavior to oxygen transport and dynamics in sandy sediments, J. Mar. Res. 64 (2006) 915–938.

[114] X.-d. Wang, R.J. Meier, M. Link, O.S. Wolfbeis, Photographing oxygen distribution, Angew. Chem. Int. Ed. 49 (2010) 4907–4909.

[115] K. Oguri, H. Kitazato, R.N. Glud, Platinum octaetylporphyrin based planar optodes combined with an UV-LED excitation light source: an ideal tool for high-resolution O_2 imaging in O_2 depleted environments, Mar. Chem. 100 (2006) 95–107.

[116] S.M. Borisov, G. Nuss, I. Klimant, Red light-excitable oxygen sensing materials based on platinum(II) and palladium(II) benzoporphyrins, Anal. Chem. 80 (2008) 9435–9442.

[117] A. Gregg, M. Hatay, A. Haas, N. Robinett, K. Barott, M. Vermeij, K. Marhaver, P. Meirelles, F. Thompson, F. Rohwer, Biological oxygen demand optode analysis of coral reef-associated microbial communities exposed to algal exudates, PeerJ 1 (2013) e107.

[118] A.J. Kessler, R.N. Glud, M.B. Cardenas, M. Larsen, M.F. Bourke, P.L.M. Cook, Quantifying denitrification in rippled permeable sands through combined flume experiments and modeling, Limnol. Oceanogr. 57 (2012) 1217–1232.

[119] M. Staal, S.M. Borisov, L.F. Rickelt, I. Klimant, M. Kühl, Ultrabright planar optodes for luminescence life-time based microscopic imaging of O_2 dynamics in biofilms, J. Microbiol. Methods 85 (2011) 67–74.

[120] A. Hakonen, S. Hulth, A high-precision ratiometric fluorosensor for pH: implementing time-dependent non-linear calibration protocols for drift compensation, Anal. Chim. Acta 606 (2008) 63–71.

[121] T. Mayr, B. Ungerboeck, G. Mistlberger, S.M. Borisov, I. Klimant, A simple method to reduce optical cross-talk effects in chemical imaging with planar optodes, Limnol. Oceanogr.: Methods 10 (2012) 101–109.

[122] C.R. Schröder, G. Neurauter, I. Klimant, Luminescent dual sensor for time-resolved imaging of pCO_2 and pO_2 in aquatic systems, Microchim. Acta 158 (2007) 205–218.

[123] Q. Zhu, R.C. Aller, Y. Fan, Two-dimensional pH distributions and dynamics in bioturbated marine sediments, Geochim. Cosmochim. Acta 70 (2006) 4933–4949.

[124] H. Stahl, A. Glud, C.R. Schroeder, I. Klimant, A. Tengberg, R.N. Glud, Time-resolved pH imaging in marine sediments with a luminescent planar optode, Limnol. Oceanogr.: Methods 4 (2006) 336–345.

[125] C.R. Schröder, L. Polerecky, I. Klimant, Time-resolved pH/pO_2 mapping with luminescent hybrid sensors, Anal. Chem. 79 (2007) 60–70.

[126] C.R. Schröder, B.M. Weidgans, I. Klimant, pH fluorosensors for use in marine systems, Analyst 130 (2005) 907–916.

[127] N. Rudolph, S. Voss, A.B. Moradi, S. Nagl, S.E. Oswald, Spatio-temporal mapping of local soil pH changes induced by roots of lupin and soft-rush, Plant Soil 369 (2013) 669–680.

[128] A. Hakonen, L.G. Anderson, J. Engelbrektsson, S. Hulth, B. Karlson, A potential tool for high-resolution monitoring of ocean acidification, Anal. Chim. Acta 786 (2013) 1–7.

[129] G. Neurauter, I. Klimant, O.S. Wolfbeis, Fiber-optic microsensor for high resolution pCO_2 sensing in marine environment, Fresenius' J. Anal. Chem. 366 (2000) 481–487.

[130] A. Mills, Q. Chang, Fluorescence plastic thin-film sensor for carbon dioxide, Analyst 118 (1993) 839–843.

[131] C.R. Schröder, I. Klimant, The influence of the lipophilic base in solid state optical pCO_2 sensors, Sens. Actuators B: Chem. 107 (2005) 572–579.

[132] N. Strömberg, S. Hulth, A fluorescence ratiometric detection scheme for ammonium ions based on the solvent sensitive dye MC 540, Sens. Actuators B: Chem. 90 (2003) 308–318.

[133] N. Strömberg, S. Hulth, An ammonium selective fluorosensor based on the principles of coextraction, Anal. Chim. Acta 443 (2001) 215–225.

[134] S. Delin, N. Strömberg, Imaging-optode measurements of ammonium distribution in soil after different manure amendments, Eur. J. Soil Sci. 62 (2011) 295–304.

[135] C. Krause, T. Werner, C. Huber, O.S. Wolfbeis, M.J.P. Leiner, pH-insensitive ion selective optode: a coextraction-based sensor for potassium ions, Anal. Chem. 71 (1999) 1544–1548.

[136] A. Hakonen, Plasmon enhancement and surface wave quenching for phase ratiometry in coextraction-based fluorosensors, Anal. Chem. 81 (2009) 4555–4559.

[137] A. Hakonen, N. Strömberg, Diffusion consistent calibrations for improved chemical imaging using nanoparticle enhanced optical sensors, Analyst 137 (2012) 315–321.

[138] M.M.F. Choi, Fluorimetric optode membrane for sulfide detection, Analyst 123 (1998) 1631–1634.

[139] G. Zhou, H. Wang, Y. Ma, X. Chen, An NBD fluorophore-based colorimetric and fluorescent chemosensor for hydrogen sulfide and its application for bioimaging, Tetrahedron 69 (2013) 867–870.

[140] M.R. Shahriari, J. Ding, Active silica-gel films for hydrogen sulfide optical sensor application, Opt. Lett. 19 (1994) 1085–1087.

[141] M.M.F. Choi, P. Hawkins, Development of an optical hydrogen sulphide sensor, Sens. Actuators B: Chem. 90 (2003) 211–215.

[142] S.M. Borisov, I. Klimant, Blue LED excitable temperature sensors based on a new europium(III) chelate, J. Fluoresc. 18 (2008) 581–589.

[143] N. Strömberg, A. Hakonen, Plasmophore sensitized imaging of ammonia release from biological tissues using optodes, Anal. Chim. Acta 704 (2011) 139–145.

[144] H. Peng, M.I.J. Stich, J. Yu, L.-n. Sun, L.H. Fischer, O.S. Wolfbeis, Luminescent europium(III) nanoparticles for sensing and imaging of temperature in the physiological range, Adv. Mater. 22 (2010) 716–719.

[145] M.I.J. Stich, S. Nagl, O.S. Wolfbeis, U. Henne, M. Schaeferling, A dual luminescent sensor material for simultaneous imaging of pressure and temperature on surfaces, Adv. Funct. Mater. 18 (2008) 1399–1406.

[146] C. Huber, I. Klimant, C. Krause, T. Werner, O.S. Wolfbeis, Nitrate-selective optical sensor applying a lipophilic fluorescent potential-sensitive dye, Anal. Chim. Acta 449 (2001) 81–93.

[147] C. Huber, C. Krause, T. Werner, O.S. Wolfbeis, Serum chloride optical sensors based on dynamic quenching of the fluorescence of photo-immobilized lucigenin, Microchim. Acta 142 (2003) 245–253.

[148] M. Bedoya, M.T. Díez, M.C. Moreno-Bondi, G. Orellana, Humidity sensing with a luminescent Ru(II) complex and phase-sensitive detection, Sens. Actuators B: Chem. 113 (2006) 573–581.

[149] T. Abel, B. Ungerboeck, I. Klimant, T. Mayr, Fast responsive, optical trace level ammonia sensor for environmental monitoring, Chem. Cent. J. 6 (2012) .

[150] S.M. Borisov, R. Seifner, I. Klimant, A novel planar optical sensor for simultaneous monitoring of oxygen carbon dioxide, pH and temperature, Anal. Bioanal. Chem. 400 (2011) 2463–2474.

[151] M.I.J. Stich, L.H. Fischer, O.S. Wolfbeis, Multiple fluorescent chemical sensing and imaging, Chem. Soc. Rev. 39 (2010) 3102–3114.

[152] Z. Cao, Q. Zhu, R.C. Aller, J.Y. Aller, S. Waugh, Seasonal, 2-D sedimentary extracellular enzyme activities and controlling processes in Great Peconic Bay, Long Island, J. Mar. Res. 71 (2013) 399–423.

[153] M. Spohn, A. Carminati, Y. Kuzyakov, Soil zymography – a novel in situ method for mapping distribution of enzyme activity in soil, Soil Biol. Biochem. 58 (2013) 275–280.

[154] M. Spohn, Y. Kuzyakov, Distribution of microbial- and root-derived phosphatase activities in the rhizosphere depending on P availability and C allocation – coupling soil zymography with ^{14}C imaging, Soil Biol. Biochem. 67 (2013) 106–113.

[155] M. Spohn, Y. Kuzyakov, Spatial and temporal dynamics of hotspots of enzyme activity in soil as affected by living and dead roots – a soil zymography analysis, Plant Soil 379 (2014) 67–77.

[156] W. Yin, H. Cui, Z. Yang, C. Li, M. She, B. Yin, J. Li, G. Zhao, Z. Shi, Facile synthesis and characterization of rhodamine-based colorimetric and "off–on" fluorescent chemosensor for Fe^{3+}, Sens. Actuators B: Chem. 157 (2011) 675–680.

[157] X.-B. Zhang, J. Peng, C.-L. He, G.-L. Shen, R.-Q. Yu, A highly selective fluorescent sensor for Cu^{2+} based on 2-(2′-hydroxyphenyl) benzoxazole in a poly(vinyl chloride) matrix, Anal. Chim. Acta 567 (2006) 189–195.

[158] P. Du, S.J. Lippard, A highly selective turn-on colorimetric, red fluorescent sensor for detecting mobile zinc in living cells, Inorg. Chem. 49 (2010) 10753–10755.

[159] W.H. Chan, R.H. Yang, K.M. Wang, Development of a mercury ion-selective optical sensor based on fluorescence quenching of 5,10,15,20-tetraphenylporphyrin, Anal. Chim. Acta 444 (2001) 261–269.

[160] L. Pischedda, J.C. Poggiale, P. Cuny, F. Gilbert, Imaging oxygen distribution in marine sediments. The importance of bioturbation and sediment heterogeneity, Acta Biotheor. 56 (2008) 123–135.

[161] A.F. Haas, A.K. Gregg, J.E. Smith, M.L. Abieri, M. Hatay, F. Rohwer, Visualization of oxygen distribution patterns caused by coral and algae, PeerJ 1 (2013) e106.

[162] S. Blossfeld, J. Perriguey, T. Sterckeman, J.L. Morel, R. Lösch, Rhizosphere pH dynamics in trace-metal-contaminated soils, monitored with planar pH optodes, Plant Soil 330 (2010) 173–184.

[163] L. Pischedda, P. Cuny, J. Luis Esteves, J.-C. Poggiale, F. Gilbert, Spatial oxygen heterogeneity in a Hediste diversicolor irrigated burrow, Hydrobiologia 680 (2012) 109–124.

[164] N. Rudolph, H.G. Esser, A. Carminati, A.B. Moradi, A. Hilger, N. Kardjilov, S. Nagl, S.E. Oswald, Dynamic oxygen mapping in the root zone by fluorescence dye imaging combined with neutron radiography, J. Soils Sediments 12 (2012) 63–74.

[165] A. Song, S. Parus, R. Kopelman, High-performance fiber-optic pH microsensors for practical physiological measurements using a dual-emission sensitive dye, Anal. Chem. 69 (1997) 863–867.

Please cite this article in press as: J. Santner, et al., Two decades of chemical imaging of solutes in sediments and soils – a review, Anal. Chim. Acta (2015), http://dx.doi.org/10.1016/j.aca.2015.02.006

[166] M.I.J. Stich, S.M. Borisov, U. Henne, M. Schaeferling, Read-out of multiple optical chemical sensors by means of digital color cameras, Sens. Actuators B: Chem. 139 (2009) 204–207.

[167] A. Hakonen, J.E. Beves, N. Strömberg, Digital colour tone for fluorescence sensing: a direct comparison of intensity, ratiometric and hue based quantification, Analyst 139 (2014) 3524–3527.

[168] H. Tschiersch, G. Liebsch, A. Stangelmayer, L. Borisjuk, H. Rolletschek, Planar oxygen sensors for non invasive imaging in experimental biology, in: I. Minin, O. Minin (Eds.), Microsensors, InTech, 2011.

[169] M. Faget, S. Blossfeld, P. Von Gillhaußen, U. Schurr, V.M. Temperton, Disentangling who is who during rhizosphere acidification in root interactions: combining fluorescence with optode techniques, Front. Plant Sci. 4 (2013) .

[170] G. Holst, O. Kohls, I. Klimant, B. Konig, M. Kühl, T. Richter, A modular luminescence lifetime imaging system for mapping oxygen distribution in biological samples, Sens. Actuators B: Chem. 51 (1998) 163–170.

[171] R.M. Ballew, J.N. Demas, An error analysis of the rapid lifetime determination method for the evaluation of single exponential decays, Anal. Chem. 61 (1989) 30–33.

[172] R.J. Woods, S. Scypinski, L.J.C. Love, Transient digitizer for the determination of microsecond luminescence lifetimes, Anal. Chem. 56 (1984) 1395–1400.

[173] S.M. Borisov, K. Gatterer, B. Bitschnau, I. Klimant, Preparation and characterization of chromium(iii)-activated yttrium aluminum borate: a new thermographic phosphor for optical sensing and imaging at ambient temperatures, J. Phys. Chem. C 114 (2010) 9118–9124.

[174] G. Liebsch, I. Klimant, C. Krause, O.S. Wolfbeis, Fluorescent imaging of pH with optical sensors using time domain dual lifetime referencing, Anal. Chem. 73 (2001) 4354–4363.

[175] P. Hartmann, W. Ziegler, Lifetime imaging of luminescent oxygen sensors based on all-solid-state technology, Anal. Chem. 68 (1996) 4512–4514.

[176] T. Fenchel, R.N. Glud, Benthic primary production and O_2–CO_2 dynamics in a shallow-water sediment: spatial and temporal heterogeneity, Ophelia 53 (2000) 159–171.

[177] P. Hartmann, W. Ziegler, G. Holst, D.W. Lübbers, Oxygen flux fluorescence lifetime imaging, Sens. Actuators B: Chem. 38 (1997) 110–115.

[178] Y. Gao, N. Lehto, A simple laser ablation ICPMS method for the determination of trace metals in a resin gel, Talanta 92 (2012) 78–83.

[179] A. Kreuzeder, J. Santner, T. Prohaska, H. Zhang, W.W. Wenzel, Uncertainty evaluation of the diffusive gradients in thin films technique, Environ. Sci. Technol. 49 (2015) 1594–1602.

[180] S.F. Durrant, Laser ablation inductively coupled plasma mass spectrometry: achievements problems, prospects, J. Anal. At. Spectrom. 14 (1999) 1385–1403.

[181] D. Günther, B. Hattendorf, Solid sample analysis using laser ablation inductively coupled plasma mass spectrometry, TrAC – Trends Anal. Chem. 24 (2005) 255–265.

[182] D.J. Bellis, G.M. Nowell, C.J. Ottley, D.G. Pearson, W. Davison, Solution and laser ablation analysis of sulphur isotopes with the neptune high resolution multi-collector ICP-MS (MC-ICP-MS): application to diffusive gradients in thin films, in: G. Holland, D. Bandura (Eds.), Plasma Source Mass Spectrometry. Current Trends and Future Developments, RSC Publishing, Cambridge, 2005, pp. 268–283.

[183] W. Davison, H. Zhang, Progress in understanding the use of diffusive gradients in thin films (DGT) back to basics, Environ. Chem. 9 (2012) 1–13.

[184] M.O. Krom, P. Davison, H. Zhang, W. Davison, High-resolution pore-water sampling with a gel sampler, Limnol. Oceanogr. 39 (1994) 1967–1972.

[185] M.R. Sangi, M.J. Halstead, K.A. Hunter, Use of the diffusion gradient thin film method to measure trace metals in fresh waters at low ionic strength, Anal. Chim. Acta 456 (2002) 241–251.

[186] M.C. Alfaro-de la Torre, P.-Y. Beaulieu, A. Tessier, In situ measurement of trace metals in lakewater using the dialysis and DGT techniques, Anal. Chim. Acta 418 (2000) 53–68.

[187] K.W. Warnken, H. Zhang, W. Davison, Trace metal measurements in low ionic strength synthetic solutions by diffusive gradients in thin films, Anal. Chem. 77 (2005) 5440–5446.

[188] Ø.A. Garmo, W. Davison, H. Zhang, Interactions of trace metals with hydrogels and filter membranes used in DET and DGT techniques, Environ. Sci. Technol. 42 (2008) 5682–5687.

[189] Ø.A. Garmo, W. Davison, H. Zhang, Effects of binding of metals to the hydrogel and filter membrane on the accuracy of the diffusive gradients in thin films technique, Anal. Chem. 80 (2008) 9220–9225.

[190] M.P. Harper, W. Davison, W. Tych, Estimation of pore water concentrations from DGT profiles: a modelling approach, Aquat. Geochem. 5 (1999) 337–355.

[191] Ł. Sochaczewski, W. Davison, H. Zhang, W. Tych, Understanding small-scale features in DGT measurements in sediments, Environ. Chem. 6 (2009) 477–485.

[192] H. Zhang, W. Davison, S. Miller, W. Tych, In situ high resolution measurements of fluxes of Ni, Cu, Fe, and Mn and concentrations of Zn and Cd in porewaters by DGT, Geochim. Cosmochim. Acta 59 (1995) 4181–4192.

[193] W. Davison, H. Zhang, K.W. Warnken, Chapter 16 – theory and applications of DGT measurements in soils and sediments, in: R. Greenwood, G. Mills, B. Vrana (Eds.), Comprehensive Analytical Chemistry. Passive Sampling Techniques in Environmental Monitoring, Elsevier, 2007, pp. 353–378.

[194] M.P. Harper, W. Davison, H. Zhang, W. Tych, Kinetics of metal exchange between solids and solutions in sediments and soils interpreted from DGT measured fluxes, Geochim. Cosmochim. Acta 62 (1998) 2757–2770.

[195] P.S. Hooda, H. Zhang, W. Davison, A.C. Edwards, Measuring bioavailable trace metals by diffusive gradients in thin films (DGT): soil moisture effects on its performance in soils, Eur. J. Soil Sci. 50 (1999) 285–294.

[196] N.W. Menzies, B. Kusumo, P.W. Moody, Assessment of P availability in heavily fertilized soils using the diffusive gradient in thin films (DGT) technique, Plant Soil 269 (2005) 1–9.

[197] G. Liebsch, I. Klimant, B. Frank, G. Holst, O.S. Wolfbeis, Luminescence Lifetime imaging of oxygen, pH, and carbon dioxide distribution using optical sensors, Appl. Spectrosc. 54 (2000) 548–559.

[198] S.W. Smith, The Scientist and Engineer's Guide to Digital Signal Processing, California Technical Publishing, 1997, pp. 427.

[199] G. Holst, B. Grunwald, Luminescence lifetime imaging with transparent oxygen optodes, Sens. Actuators B: Chem. 74 (2001) 78–90.

[200] G. Holst, B. Grunwald, I. Klimant, M. Kühl, A luminescence lifetime imaging system using imaging fibers to measure the 2D distribution of O_2 in biological samples, M.A. Marcus, B. Culshaw (Eds.), Fiber Opt. Sens. Technol. Appl. (1999) 154–163.

[201] R.N. Glud, A. Tengberg, M. Kühl, P.O.J. Hall, I. Klimant, G. Host, An in situ instrument for planar O_2 optode measurements at benthic interfaces, Limnol. Oceanogr. 46 (2001) 2073–2080.

[202] R.N. Glud, N.B. Ramsing, N.P. Revsbech, Photosynthesis and photosynthesis-coupled respiration in natural biofilms quantified with oxygen microsensors, J. Phycol. 28 (1992) 51–60.

[203] N. Strömberg, E. Mattsson, A. Hakonen, An imaging pH optode for cell studies based on covalent attachment of 8-hydroxypyrene-1,3,6-trisulfonate to amino cellulose acetate films, Anal. Chim. Acta 636 (2009) 89–94.

[204] O.S. Wolfbeis, Chemical sensing using indicator dyes, B.C.J. Dakin (Ed.), Opt. Fiber Sens. (1997) 54–107.

[205] S.M. Borisov, D.L. Herrod, I. Klimant, Fluorescent poly(styrene-block-vinylpyrrolidone) nanobeads for optical sensing of pH, Sens. Actuators B: Chem. 139 (2009) 52–58.

[206] S.-K. Lee, I. Okura, Photostable optical oxygen sensing material: platinum tetrakis(pentafluorophenyl) porphyrin immobilized in polystyrene, Anal. Commun. 34 (1997) 185–188.

[207] Z. Zhang, Y. Zhang, W. Ma, R. Russell, Z.M. Shakhsher, C.L. Grant, W.R. Seitz, D. C. Sundberg, Poly(vinyl alcohol) as a substrate for indicator immobilization for fiber-optic chemical sensors, Anal. Chem. 61 (1989) 202–205.

[208] T.C. O'Riordan, H. Voraberger, J.P. Kerry, D.B. Papkovsky, Study of migration of active components of phosphorescent oxygen sensors for food packaging applications, Anal. Chim. Acta 530 (2005) 135–141.

[209] N. Strömberg, J. Engelbrektsson, S. Delin, A high throughput optical system for imaging optodes, Sens. Actuators B: Chem. 140 (2009) 418–425.

[210] G.J. Mohr, O.S. Wolfbeis, Optical sensors for a wide pH range based on azo dyes immobilized on a novel support, Anal. Chim. Acta 292 (1994) 41–48.

[211] F. Navarro-Villoslada, G. Orellana, M.C. Moreno-Bondi, T. Vick, M. Driver, G. Hildebrand, K. Liefeith, Fiber-optic luminescent sensors with composite oxygen-sensitive layers and anti-biofouling coatings, Anal. Chem. 73 (2001) 5150–5156.

[212] Y.-L. Lo, C.-S. Chu, J.-P. Yur, Y.-C. Chang, Temperature compensation of fluorescence intensity-based fiber-optic oxygen sensors using modified Stern–Volmer model, Sens. Actuators B: Chem. 131 (2008) 479–488.

[213] B. Elberling, M. Kühl, R.N. Glud, C.J. Jørgensen, L. Askaer, L.F. Rickelt, H.P. Joensen, M. Larsen, L. Liengaard, Methods to assess high-resolution subsurface gas concentrations and gas fluxes in wetland ecosystems, in: R. D. DeLaune, K.R. Reddy, C.J. Richardson, J.P. Megonigal (Eds.), Methods in Biogeochemistry of Wetlands, Soil Science Society of America, 2013, pp. 949–970.

[214] L.M. Coyle, M. Gouterman, Correcting lifetime measurements for temperature, Sens. Actuators B: Chem. 61 (1999) 92–99.

[215] C. Baleizão, S. Nagl, M. Schäferling, M.r.N. Berberan-Santos, O.S. Wolfbeis, Dual fluorescence sensor for trace oxygen and temperature with unmatched range and sensitivity, Anal. Chem. 80 (2008) 6449–6457.

[216] S.M. Borisov, O.S. Wolfbeis, Temperature-sensitive europium(iii) probes and their use for simultaneous luminescent sensing of temperature and oxygen, Anal. Chem. 78 (2006) 5094–5101.

[217] A. Tengberg, J. Hovdenes, H.J. Andersson, O. Brocandel, R. Diaz, D. Hebert, T. Arnerich, C. Huber, A. Kortzinger, A. Khripounoff, F. Rey, C. Ronning, J. Schimanski, S. Sommer, A. Stangelmayer, Evaluation of a lifetime-based optode to measure oxygen in aquatic systems, Limnol. Oceanogr.: Methods 4 (2006) 7–17.

[218] O.S. Wolfbeis, H. Offenbacher, Fluorescence sensor for monitoring ionic strength and physiological pH values, Sens. Actuators 9 (1986) 85–91.

[219] B.M. Weidgans, C. Krause, I. Klimant, O.S. Wolfbeis, Fluorescent pH sensors with negligible sensitivity to ionic strength, Analyst 129 (2004) 645–650.

[220] J.R. Bacon, J.N. Demas, Determination of oxygen concentrations by luminescence quenching of a polymer-immobilized transition-metal complex, Anal. Chem. 59 (1987) 2780–2785.

[221] S.M. Borisov, P. Lehner, I. Klimant, Novel optical trace oxygen sensors based on platinum(II) and palladium(II) complexes with 5,10,15,20-meso-tetrakis-(2,3,4,5,6-pentafluorphenyl)-porphyrin covalently immobilized on silica-gel particles, Anal. Chim. Acta 690 (2011) 108–115.

[222] A. Hakonen, N. Strömberg, Plasmonic nanoparticle interactions for high-performance imaging fluorosensors, Chem. Commun. 47 (2011) 3433–3435.

[223] U. Franke, Applications of planar oxygen optodes in biological aquatic systems, PhD Thesis, University Bremen, 2005.

Please cite this article in press as: J. Santner, et al., Two decades of chemical imaging of solutes in sediments and soils – a review, Anal. Chim. Acta (2015), http://dx.doi.org/10.1016/j.aca.2015.02.006

[224] P.L.M. Cook, F. Wenzhöfer, R.N. Glud, F. Janssen, M. Huettel, Benthic solute exchange and carbon mineralization in two shallow subtidal sandy sediments: effect of advective pore-water exchange, Limnol. Oceanogr. 52 (2007) 1943–1963.

[225] M.S. Frederiksen, R.N. Glud, Oxygen dynamics in the rhizosphere of *Zostera marina*: a two-dimensional planar optode study, Limnol. Oceanogr. 51 (2006) 1072–1083.

[226] M. Larsen, J. Santner, E. Oburger, W.W. Wenzel, R.N. Glud, O_2 dynamics in the rhizosphere of young rice plants (*Oryza sativa* L.), Plant Soil (2015) (in press).

[227] N. Strömberg, Determination of ammonium turnover and flow patterns close to roots using imaging optodes, Environ. Sci. Technol. 42 (2008) 1630–1637.

[228] C. Carreira, M. Larsen, R.N. Glud, C.P.D. Brussaard, M. Middelboe, Heterogeneous distribution of prokaryotes and viruses at the microscale in a tidal sediment, Aquat. Microb. Ecol. 69 (2013) 183–192.

[229] F.J.R. Meysman, O.S. Galaktionov, R.N. Glud, J.J. Middelburg, Oxygen penetration around burrows and roots in aquatic sediments, J. Mar. Res. 68 (2010) 309–336.

[230] R.C. Aller, The effects of macrobenthos on chemical properties of marine sediment and overlying water, in: P. McCall, M. Tevesz (Eds.), Animal–Sediment Relations. The Biogenic Alteration of Sediments, Plenum, New York, 1982, pp. 53–102.

[231] U. Franke, L. Polerecky, E. Precht, M. Huettel, Wave tank study of particulate organic matter degradation in permeable sediments, Limnol. Oceanogr. 51 (2006) 1084–1096.

[232] L. Polerecky, U. Franke, U. Werner, B. Grunwald, D. de Beer, High spatial resolution measurement of oxygen consumption rates in permeable sediments, Limnol. Oceanogr.: Methods 3 (2005) 75–85.

[233] M.F. Bourke, A.J. Kessler, P.L.M. Cook, Influence of buried *Ulva lactuca* on denitrification in permeable sediments, Mar. Ecol. Prog. Ser. 498 (2014) 85–U420.

[234] H.C. Nilsson, R. Rosenberg, Succession in marine benthic habitats and fauna in response to oxygen deficiency: analysed by sediment profile-imaging and by grab samples, Mar. Ecol. Prog. Ser. 197 (2000) 139–149.

[235] M. Kühl, G. Holst, A.W.D. Larkum, P.J. Ralph, Imaging of oxygen dynamics within the endolithic algal community of the massive coral *Porites lobata*, J. Phycol. 44 (2008) 541–550.

[236] S. Rysgaard, R.N. Glud, Anaerobic N_2 production in Arctic sea ice, Limnol. Oceanogr. 49 (2004) 86–94.

[237] N. Volkenborn, L. Polerecky, D.S. Wethey, S.A. Woodin, Oscillatory porewater bioadvection in marine sediments induced by hydraulic activities of *Arenicola marina*, Limnol. Oceanogr. 55 (2010) 1231–1247.

[238] Z. Jovanovic, M. Larsen, C. Organo Quintana, E. Kristensen, R.N. Glud, Oxygen dynamics and porewater transport in sediments inhabited by the invasive polychaete *Marenzelleria viridis*, Mar. Ecol. Prog. Ser. 504 (2014) 181–192.

[239] K. Koop-Jakobsen, F. Wenzhöfer, The dynamics of plant-mediated sediment oxygenation in *Spartina anglica* rhizospheres – a planar optode study, Estuaries Coasts (2014) (in press).

[240] C.M. Schreiber, B. Zeng, S. Blossfeld, U. Rascher, M. Kazda, U. Schurr, A. Höltkemeier, A.J. Kuhn, Monitoring rhizospheric pH, oxygen, and organic acid dynamics in two short-time flooded plant species, J. Plant Nutr. Soil Sci. 175 (2012) 761–768.

[241] B. Grunwald, M. Kühl, A system for imaging variable chlorophyll fluorescence of aquatic phototrophs, Ophelia 58 (2004) 79–89.

[242] J.P. Fischer, K. Koop-Jakobsen, The multi fiber optode (MuFO): a novel system for simultaneous analysis of multiple fiber optic oxygen sensors, Sens. Actuators B: Chem. 168 (2012) 354–359.

[243] T. Mayr, C. Igel, G. Liebsch, I. Klimant, O.S. Wolfbeis, Cross-reactive metal ion sensor array in a micro titer plate format, Anal. Chem. 75 (2003) 4389–4396.

[244] L.F. Rickelt, L. Askaer, E. Walpersdorf, B. Elberling, R.N. Glud, M. Kühl, An optode sensor array for long-term in situ oxygen measurements in soil and sediment, J. Environ. Qual. 42 (2013) 1267–1273.

[245] C. Huber, I. Klimant, C. Krause, T. Werner, T. Mayr, O.S. Wolfbeis, Optical sensor for seawater salinity, Fresenius J. Anal. Chem. 368 (2000) 196–202.

Please cite this article in press as: J. Santner, et al., Two decades of chemical imaging of solutes in sediments and soils – a review, Anal. Chim. Acta (2015), http://dx.doi.org/10.1016/j.aca.2015.02.006